Investigation of Co nanoparticle formation using time-dependent and spatially-resolved X-ray Absorption Spectroscopy

Dissertation

zur

Erlangung des Doktorgrades (Dr. rer. nat.)

der

Mathematisch-Naturwissenschaftlichen Fakultät

der

Rheinischen Friedrich-Wihelms-Universität Bonn

vorgelegt von

Svetlana Zinoveva

aus

Samara

Bonn Februar, 2008

Investigation of Co nanoparticle formation using time-dependent and spatially-resolved X-ray Absorption Spectroscopy

Dissertation

zur

Erlangung des Doktorgrades (Dr. rer. nat.)

der

Mathematisch-Naturwissenschaftlichen Fakultät

der

Rheinischen Friedrich-Wihelms-Universität Bonn

vorgelegt von

Svetlana Zinoveva

aus

Samara

Bonn Februar 2008

Angefertigt mit Genehmigung der Mathematisch-Naturwissenschaftlichen Fakultät
Der Rheinischen Friedrich-Wihelms-Universität Bonn

Referent: Prof. Dr. J. F. Hormes
Korreferent: Prof. Dr. K. Maier

Tag der Promotion: 20.03.2008

Abstract

A crucial step towards controlled synthesis of nanoparticles is the detailed understanding of the various chemical processes that take place during the synthesis. X-ray Absorption Spectroscopy (XAS) is especially suitable for elucidating the type and structure of the intermediate metal species. It is applicable to materials that have no long range order and provides information on both electronic and geometric structures. Here a comparative study is reported of the formation of cobalt nanoparticles via thermolysis of two organometallic precursors dicobalt octacarbonyl (DCO) and alkyne-bridged dicobalt hexacarbonyl (ADH) in the presence of aluminum organics. Using time-dependent XAS a reaction pathway different from both the atom based La Mer model and the Watzky and Finsky autocatalytic surface growth model is observed. Where prior to the nucleation several intermediates are formed and the initial nucleus is composed of Co atoms coordinated with ligands $Co_n(CO)_m$ with n=2-3, m=3-5.

The formation of Co nanoparticles was also investigated using a reaction different from thermolysis of cobalt carbonyls, namely reduction of Co (II) acetate by sodium borohydrate. Here the combination of microreactor system and spatially resolved XAS allowed "*in situ*" monitoring of the wet chemical synthesis. Several steps of the reaction were spatially resolved in the microreactor. The vertical size of the X-ray beam (50 µm) focused with Kirkpatrick-Baez mirror system, determines the time resolution (better than 2 ms). The results provide direct insight into rapid process of nanoparticles formation and demonstrate the potential of this new technique for the fundamental studies of such type of processes where miniaturization and time-resolution are important. Like in the carbonyls thermolysis no evidence for the reduction of the starting complex to isolated Co^0 atoms followed by nucleation of Co^0 atoms was observed.

Table of Contents

Chapter 1 Introduction

One of the aims of nanoscience is to gain the ability to prepare nanoclusters that have very narrow size distribution, well defined phase, shape, composition (e.g. of multimetallic), and thereby allowing for greater uniformity of nanoclusters properties.

Two main approaches are used in nanotechnology to produce nanoparticles. In the "bottom-up" approach nanoparticles are built from molecular components, through controlled chemical reactions; in the "top-down" approach, through changes induced in macroscopic structures. Among the “top-down” approaches, electron beam lithography, molecular beam epitaxy[1] and application of AFM (Atomic Force Microscope)[2] are the techniques that allow the deliberate fabrication and manipulation of nanostructures. Among the “bottom-up” approaches, the wet-chemical approach appears to be the most promising for industrial applications due to its intrinsic scale-up potential. Wet-chemical synthesis methods can be broadly classified into co-precipitation and chemical reduction, which can be carried out either in traditional batch technique or in micro fluidic processes.[3]

A detailed understanding of the mechanism of nanocluster formation will allow greater control over nanocluster properties and the ability to tune these properties simply by varying the reaction conditions. While measurements of reaction kinetics suffice for the catalysis community, where understanding the processes used to produce the active phase of a catalyst is the primary concern, industrial applications of nanotechnology demand nanoparticles with superior magnetic and electronic properties. Detailed spectroscopic studies of nanoparticle synthesis are few. This is partially due to limitations of techniques to be applied to nanoscale materials, or difficulties inherent in “*in situ”* investigations.

The dominant technique for measuring particles size is electron microscopy with different imaging modes such as Transmission Electron Microscopy (TEM) Scanning Electron Microscopy (SEM), Scanning Transmission Electron Microscopy (STEM) and for the highest ever achieved resolution of about 0.5 Å- High Resolution Transmission Electron Microscopy (HRTEM); but these techniques cannot be used in situ, because sample have to be viewed in vacuum.

The most popular method that is used to study the kinetics of nanocluster formation in solution is UV-visible spectroscopy. Although this is a useful method for some systems, it requires that the nanoclusters under investigation absorb in the UV-visible region, and this tends to restrict the studies to the metals with distinct plasmon absorbances in the visible region, namely Ag, Au, and Cu and to exclude nanoclusters of many interesting metals, including Fe, Co, Ni and Pt. Alternatively, UV-visible spectroscopy can be used to follow the loss of the precursor of the reaction (provided that it absorbs in the UV-visible region) or to obtain information of surface composition if organic molecules are adsorbed, but no direct access to the interaction between the core and the surfactant is possible.

X-ray Photoelectron Spectroscopy (XPS) and Energy Dispersive X-ray Spectroscopy (EDX/EDS) are technological variants used predominantly for determining the elemental composition and chemical state of a material, but fail to determine the geometric structure of the

sample under investigation. X-ray Powder Diffraction (XPD) provides information about geometric arrangements of atoms, but is limited to large crystalline clusters. Structure of growing particles smaller than 5 nm, can no longer be reliably determined by XPD because it drops below the minimum size of coherent scattering region that can be detected in XPD experiment.[4]

Among these numerous experimental techniques, X-ray Absorption Spectroscopy (XAS) is a powerful method to probe both the electronic and structural properties of a large class of systems, ranging from solid-state materials to proteins.[5] XAS offers the following advantages as a spectroscopic technique:

- It can be used for any type of media: gases, liquids, and solids (amorphous or ordered) as it probes the local structure around the atom of interest and no long range order is required.
- It is highly element selective, since one can interrogate one type of atom of a given solute specifically, e.g., by simply tuning to its characteristic absorption edge.
- It delivers both electronic and structural information, which is essential in chemistry, where changes in electronic structure drive the nuclear dynamics.
- The precision of structural determination by Extended X-ray Absorption Fine Structure (EXAFS) is ~ 0.02 Å, which is excellent for observing transient structures of reaction intermediates.
- Due to the penetration strength of X-rays, measurements do not require a good vacuum and in many cases "*in situ*" measurements, i.e. observing the chemical processes taking place during a synthetic reaction are possible.

All these advantages are particularly attractive for the study of nanoparticles and dynamical processes in chemistry, biology, and material science. In this work XAS will be applied to study Co nanoparticle formation.

Considerable information about nanoparticles synthesis has been collected in the last decade. For example, Victor F. Puntes, *et al.*[6] reported synthesis of cobalt nanoparticles with spherical, cubic and rod-like shapes by varying the surfactant composition (oleic acid, phosphonic oxides and acids), its concentration and the reaction temperature. A combination of x-ray powder diffraction, TEM and Superconducting Quantum Interference Device (SQUID) magnetometry has been used to characterize the nanocrystals. Bao Y., *et al.*.[7] described the synthesis of monodispersed cobalt nanocrystals with controlled crystal morphology and investigation of the surface stability of these nanocrystals, depending on the surfactants used. Using TEM, XPD and magnetic measurements with SQUID he demonstrated that at room temperature the surfactant protective layer and, alternatively, at higher temperature the crystal morphology (single-crystal or multiple-grained nanoparticles) play the dominant roles in their stability with respect to oxidation. In the recent past, Lagunas A., *et al.* [8] reported a study of the effect of surfactants (trioctylphosphine oxide and oleic acid) on the kinetics and rate of thermal decomposition of dicobalt octacarbonyl ($Co_2(CO)_8$) leading to the formation of colloidal cobalt nanoparticles. Several of the reaction intermediates connecting $Co_2(CO)_8$ with Co nanoparticles were identified, and a tentative mechanism for the formation of the colloidal nanoparticles was proposed. Also a comparative study on the influence of a precursor on the formation of cobalt nanoparticles, using time-dependent FT-IR spectroscopy analysis, was recently undertaken in our group.[9] It was demonstrated that formation of nanoparticles is influenced by the choice of the precursor, which in turn influenced physical properties, such as particle size, crystal structure and oxidative

stability. It was suggested that the presence of different reaction intermediates influencing the formation of cobalt nanoparticles. Nevertheless there is currently no clear picture of what happens during the nanocluster's formation: whether the metal precursor is reduced to isolated metal atoms M^0 or formation of stable nuclei composed of intermediate species (metal atoms with some of their igands) M_xL_y occurs first and then the cluster is reduced to the zerovalent metal cluster M^0_n? In other words, when does reduction take pace and what are the roles of ligands in the nucleation process?

The goal of this work is to follow different stages in the reaction leading to the formation of nanoparticles, from initial nucleation to final particles using X-ray absorption spectroscopy. In the first part of the work, "time–dependent" investigation of the mechanism of cobalt nanoparticles formation in the course of the thermal decomposition of dicobalt octacarbonyl (DCO) and alkyne-bridged dicobalt hexacarbonyl (ADH) complexes is presented. From X-ray Absorption Near Edge Structure (XANES) and Extended X-ray Absorption Fine Structure (EXAFS) analysis, information about local geometry of the particles during the course of the synthesis is revealed. Formation of several intermediates is observed. The crystal structure and the particle size of the cobalt nanoparticles formed were found to vary during the course of the reaction. The variation in particle size was supported by TEM measurements. A descriptive picture of what happens during cobalt nanoparticle nucleation and growth is proposed.

In the second part of this work X-ray absorption spectroscopy is extended to real "*in situ*" measurements. In spite of the unquestionable advantage as compared to other techniques, both "conventional" time-resolved XAS techniques for the characterization of nanoparticles and their synthetic reactions have also some drawbacks: using an energy dispersive monochromator (EDM) or a conventional double crystal monochromator in "Quick-EXAFS mode" require significant integrations time per spectrum and per energy step, respectively, because of the normally relatively low concentration of the active components in the reaction chamber. Thus, it is not possible to use the full potential of these techniques regarding their time resolution. There are additional problems in a batch synthesis caused by inhomogeneities across the chamber (e.g. concentration, temperature etc.) even when the volume is reduced. Here experiments using a microreactor system for wet-chemical synthesis of cobalt nanoparticles in combination with spatially resolved X-ray absorption spectroscopy using a Kirkpatrick-Baez focusing system are presented. In such a system, the entire reaction is spatially resolved in the microreactor. The vertical size of the X-ray beam (50 μm) focused on the microreactor determines the time resolution (better than 2 ms). Because the flows in the microreactor are steady, the spectrum does not have to be time-resolved and can be obtained with long integration time for fluorescence detector. A reaction completely different from thermolysis of cobalt carbonyls, namely reduction of Co (II) acetate by sodium borohydrate was investigated. XANES spectra taken at different points of the microreactor, as well as microreactor final product were analyzed and compared to reference spectra of cobalt borides to gain understanding of cobalt nanoparticles formation and nanopartices formation in general.

Chapter 2 XAS theory

2.1 Introduction to X-ray Absorption Spectroscopy

X-ray absorption spectroscopy measures the absorption of x-rays as a function of x-ray energy. According to the Lambert-Beer's Law, when an x-ray beam travels though matter, it loses intensity via interaction with matter and can be described as:

$$I = I_0 * e^{-\mu(E)t} \quad \textbf{2.1}$$

where I_0 is the incident intensity, t is the sample thickness, I is the intensity transmitted through the sample, as shown in Figure 2.1and $\mu(E)$ is the *absorption coefficient*.

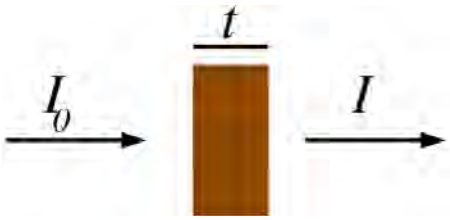

Figure 2.1 X-ray beam passing through the material of thickness *t*.

The absorption coefficient depends strongly on x-ray energy E, the atomic number Z, the density ρ and Atomic mass A of the material:

$$\mu \approx \frac{\rho Z^4}{AE^3} \quad \textbf{2.2}$$

If the absorption cross section is plotted as a function of photon energy (Figure 2.2) the experimental data show three general features[10]:

1. An overall decrease in x-ray absorption with increasing energy (Eq. 2.2).
2. The presence of a sharp rise at certain energies called edges. For this rising to occur, the photons must have enough energy to excite core shell electrons. The energetic positions of these features are unique for a given element. They occur near the ionization energy of inner shell electrons and contain spectral features due to bound to bound and bound to continuum transitions.
3. Above the edges, a series of wiggles or oscillatory structure is observed. This feature, is associated with the presence of the surrounding atoms, and therefore contains precise structural information such as interatomic distances and coordination numbers.

The XAFS spectrum is defined phenomenologically as the normalized, oscillatory part of the x-ray absorption above a given absorption edge:

$$\chi(E) = \frac{\mu(E) - \mu_0(E)}{\Delta\mu_0(E_0)} \quad \textbf{2.3}$$

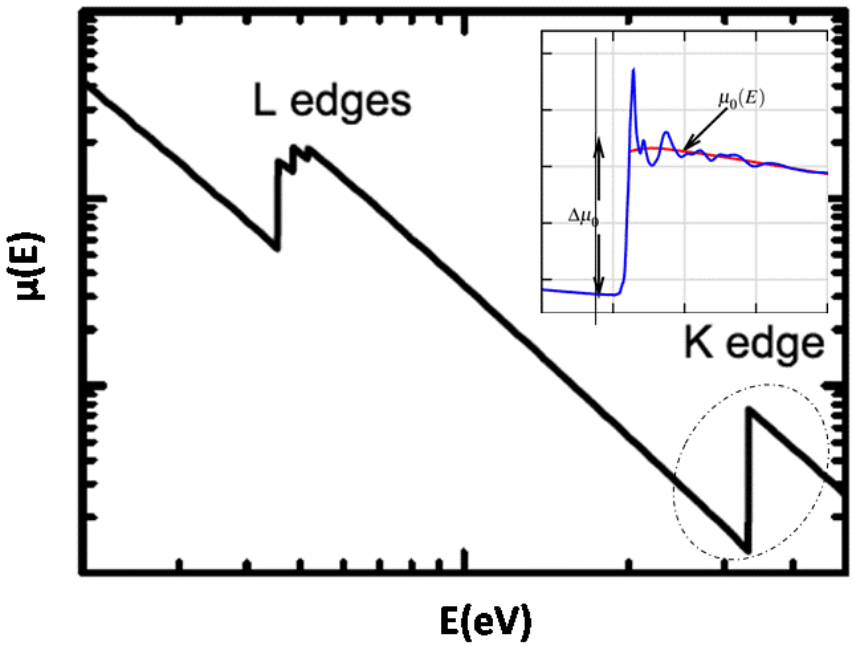

Figure 2.2 Variation of the atomic x-ray absorption cross section as a function of the photon energy.[11] Enlarged Fe K edge of FeO is in the inset.

where $\mu(E)$ is the measured absorption coefficient, $\mu_0(E)$ is a smooth atomic-like background absorption (including contributions, if any, from other edges), and $\Delta\mu_0(E_0)$ is a measured jump in the absorption $\mu_0(E)$ at the edge (edge-jump normalization, to normalize to 1 absorption event) (Figure 2.2 inset).

The absorption function measured by an XAS experiment is related to the transition rate of the photoelectron from an initial state, $|i\rangle$, into an unoccupied final state, $|f\rangle$. The probability for such a transition is determined within the one-electron and dipole approximations by Fermi's Golden Rule:

$$\mu(E) \sim \sum_f^{E>E_0} |\langle f|\tilde{\varepsilon} * \vec{r}|i\rangle|^2 \, \delta(E - E_0) \qquad \textbf{2.4}$$

where $\tilde{\varepsilon} * \vec{r}$ is the dipole operator for the incident electromagnetic wave interacting with the atom and the summation extends over all energies above the Fermi energy E_0 . Therefore, μ is a dipolematrix element of the initial state and the final state restricted to those final states which are accessible by an incident photon energy E.

Absorption edges are named after the shell from which the absorbing electron originates. In Figure 2.3, the three innermost core orbitals are shown namely the *K*, *L*, and *M* shells and the characteristic transition to the continuum is indicated. Thus the *K* edge is due to absorption by a K shell electron. Higher shells may be further specified by subshells – e.g., L_I, L_{II}, and L_{III} edges are due to 2s, 2p1/2, and 2p3/2 subshells, respectively.

Absorption of a photon leads to the excitation and the following relaxation of the atom via fluorescent x-ray or Auger electron emission. Schemes of these processes are shown in Figure

2.4. When a photon is absorbed by an inner shell electron, that electron is removed from its shell (to the continuum or another available energy state) and an electron from a more energetic shell falls into its place. The excess energy of the vacancy-filling electron is emitted as either fluorescence (Kα, K_β) or an Auger electron.

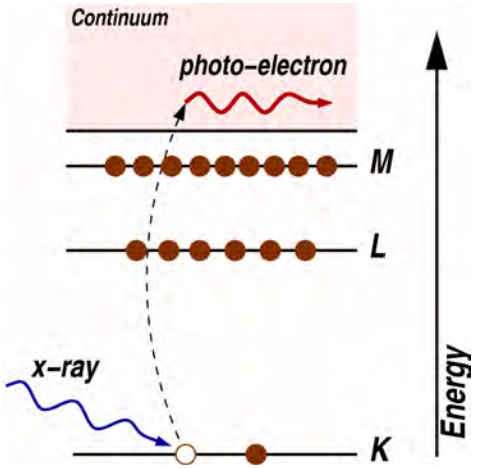

Figure 2.3 Promotion of a core electron to a continuum by absorption of x-ray photon.

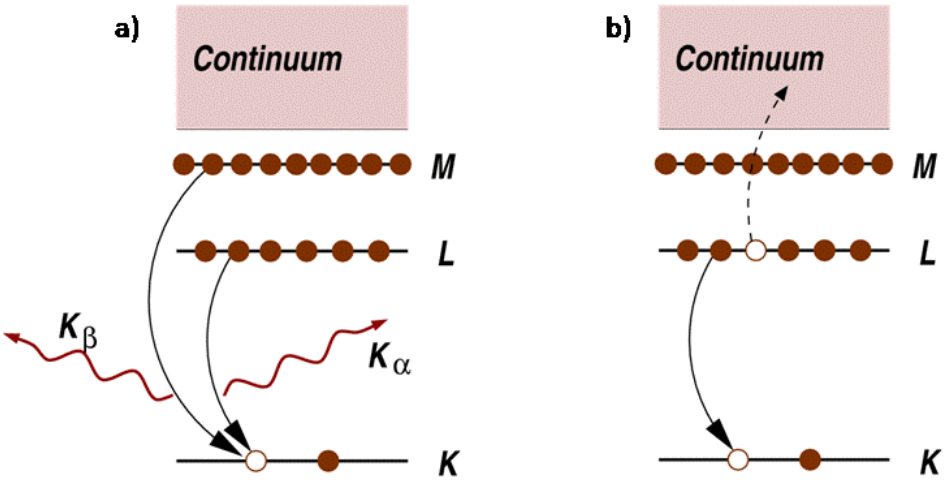

Figure 2.4 The following relaxation of the atom via fluorescence x-ray (a) and Auger effect (b).

The generally weak oscillations (wiggles) (Figure 2.5) beyond about 30 eV above the absorption edge are named Extended X-ray Absorption Fine Structure (EXAFS). The region closer to an edge typically within the first 30 eV of the edge position is referred to as X-ray Absorption Near-Edge Structure (XANES). Note that at low energies above the absorption edge, the de Broglie wavelength of the photoelectron λ_e is much larger than at higher energies:

$$\lambda_e = \frac{2\pi}{k} = \frac{\hbar}{\sqrt{2m(E-E_0)}} \qquad 2.5$$

This is the region of strong scattering where multiple scattering (MS) events are dominate. In contrast, as the λ_e decreases (at higher photoelectron's kinetic energies in the EXAFS region), the

single scattering (SS) events between selected pairs of atoms dominate the process, although the MS is still present and should be accounted for in the proper description of EXAFS. In Figure 2.6, the electron scattering is sketched for an outgoing and backscattered photoelectron wave in both SS and MS cases.

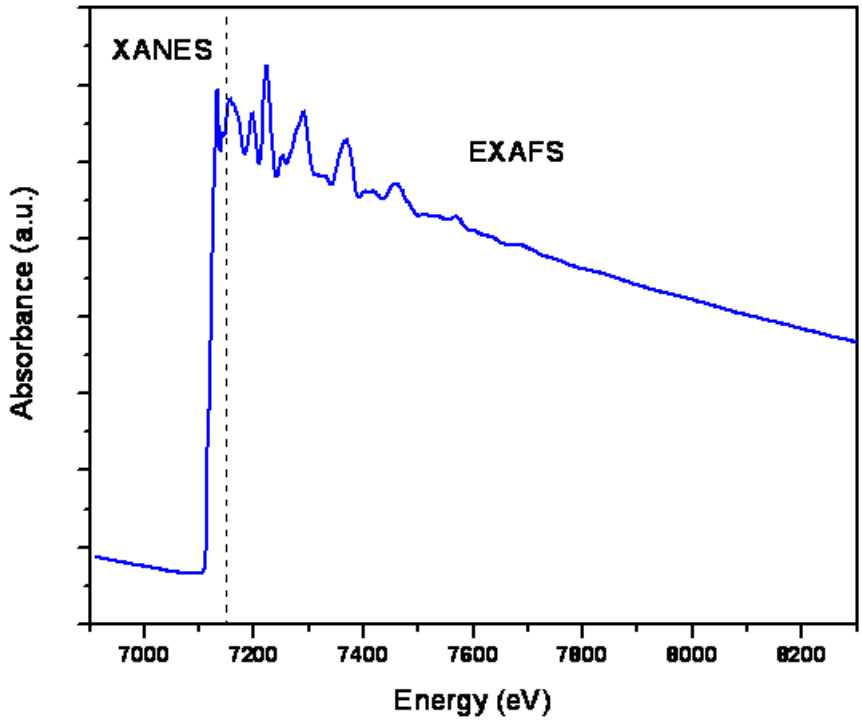

Figure 2.5 X-ray absorption spectrum of a Fe foil.

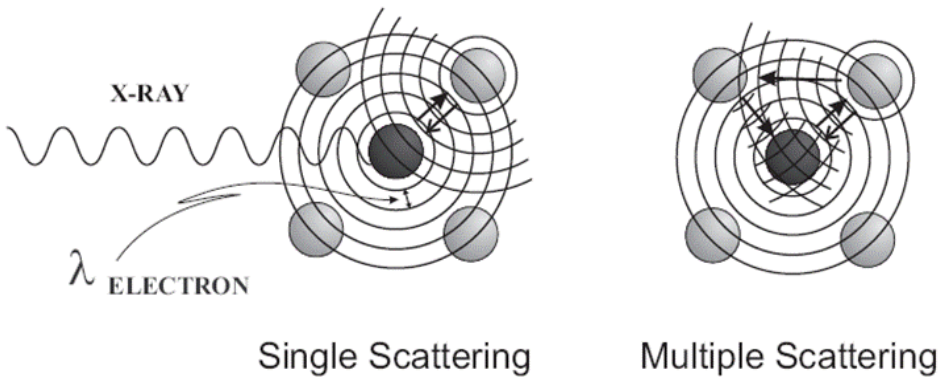

Figure 2.6 Photoelectron wave scattering in the case of EXAFS (single scattering) and XANES (multiple scattering).

The more general term XAFS was introduced by Rehr *et al*[12] to refer to the fine structure in both XANES and EXAFS, following the recognition that they both have a common origin, namely, the scattering of a photoelectron by its environment.

2.2 Extended X-ray Absorption Spectroscopy: EXAFS

XAFS is an interference effect; it depends on the wave-nature of the photoelectron. It's therefore convenient to think of XAFS in terms of photo-electron wavenumber *k*, rather than x-ray energy. The oscillations in $\chi(k)$ are shown in Figure 2.7 which is often shown weighted by k^2 or k^3 to amplify the quickly decaying oscillations at high *k*.

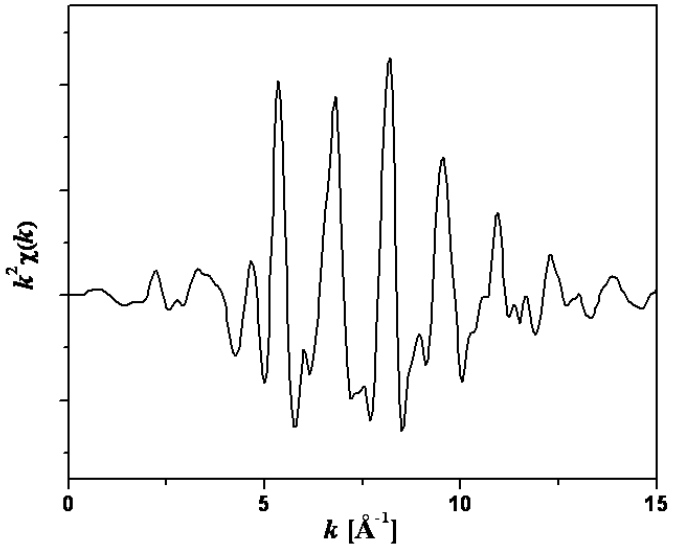

Figure 2.7 $\chi(k)$ oscillations of the Fe foil, k^2 weighted.

The different frequencies apparent in the oscillations of $\chi(k)$ correspond to different near-neighbor coordination shells which can be described by the EXAFS equation:

$$\chi(k) = \sum_i S_0^2 N_i \frac{|f_i(k)|}{kR_i^2} \sin(2kR_i + 2\delta_c + \phi) e^{-2\sigma_i^2 k^2} e^{-2R_i/\lambda(k)} \qquad \textbf{2.6}$$

defined by Sayers *et al*[13] which has become the standard for all current work. To consider the effect of all single scattering from the surrounding atoms, a summation over all scattering paths *i* is performed. In this equation N_i is the number of equivalent scatterers (coordination number) at distance R_i, S_0^2 is the passive electron reduction factor due to the shake up processes at the central atom[11,14] and is normally determined from the reference compounds. The $e^{-2\sigma_i^2 k^2}$-term describes thermal and static disorder causing an additional damping of the EXAFS amplitude (especially at large *k*) where σ^2 is the mean-square disorder in the distribution of interatomic distances (XAFS Debye-Waller factor). Generally speaking the Debye-Waller factor has two components due to static disorder and thermal vibration. The Debye-Waller approximation assumes that the vibrational/thermal motion is harmonic and the static disorder is Gaussian-like. Amplitude losses due to inelastic scattering are approximated by a damping factor $e^{\frac{-2R_i}{\lambda(k)}}$, depending upon the ratio of the distance traveled $2R_i$, to the electron mean-free-path $\lambda(k)$ (not to be confused with the de Broglie wavelength). The dependence of the oscillatory structure on interatomic distance and energy is described by the $\sin(2kR_i)$ term. Furthermore, the photoelectron experiences two more phase shifts: $2\delta_c(k)$ due to the absorbing (central) atom and ϕ due to the neighboring atom, the factor 2 in the former term denotes the fact that photoelectron wave experiences the potential of the central atom twice, once going out and once coming back.

The term $|f_i(k)|$ stands for the backscattering amplitude ($f_i(k) = |f_i(k)|e^{i\phi(k)}$), the $1/kR_i^2$ term describes the decreasing of the amplitude of an outgoing spherical wave with the distance R_i from its origin.

In relation to the structural analysis, the EXAFS description provided by Eq. 2.6 includes all the most relevant and essential parameters required for fitting the local atomic structure around the absorbing atom from the measured EXAFS spectra.

2.3 EXAFS Analysis

The most powerful application of Eq.2.6 comes from the fact that it allows expressing the complicated oscillatory pattern found in a XAS spectrum in terms of a sum of damped sine waves with their characteristic periods, which are related to the different interatomic distances. Soon after Eq. 2.6 was proposed, it was found that a Fourier transform (FT) of the EXAFS spectrum $\chi(k)$ (with respect to k) will deliver a corresponding frequency spectrum of the oscillatory part, where the characteristic frequencies will correspond to the interatomic bond distances between the absorber and the surrounding atomic shells.

As the two main components – ATHENA, a program for XAS data processing, and ARTEMIS,[15] a program for EXAFS data analysis using theoretical standards from FEFF8[16] were used in this research for the analysis of XAS data. These packages are based on the IFEFFIT[17] library of analytical and numerical algorithms and use the AUTOBK program.[17]

Subtraction of a smooth pre-edge function from $\mu(E)$ to get rid of any instrumental background and absorption from other edges is performed by the program AUTOBK. First, a pre-edge line (or simple polynomial) is fitted to the spectrum below the edge, the jump in the edge is approximated, and the spectrum is normalized by this value.

Then to approximate $\mu_0(E)$ a smooth post-edge background function is removed isolating the EXAFS $\chi(E)$. Since we don't have a measurement of $\mu_0(E)$, the absorption from an isolated atom, we approximate this with a smooth spline that matches only the low frequency components of $\mu(E)$ corresponding to a distance smaller than nearest neighbor bond length.

After the threshold energy E_0, is identified the EXAFS signal is converted from E- to k- space using Eq.2.5. It is not necessary to know the absolute value of E_0. Generally it is considered to be within 30 eV of the edge and will be refined later.

Finally, the XAFS χ(k) is weighted and Fourier transformed from k- to R- space using a window function to cope with the finite data set.[18] The Keiser Bessel Fourier transform window with Δk=2 sills was used in this research. The χ(R) has well separated peaks for different "shells". Individual shells can be isolated by Fourier filtering.

For the EXAFS data modeling, the FEFF8 program calculates scattering factors for a particular type of neighboring atoms. Once $f(k)$, $\delta(k)$, and $\lambda(k)$ are calculated, they are used in the EXAFS

equation (Eq.2.6) to predict and modify the structural parameters *R*, *N*, and σ^2 and also allow E_0 to change until we get the best-fit to the EXAFS $\chi(k)$ or FT of the data.

Standard signal analysis tells us that the maximum number of free variables that can be effectively fited in a refinement depends on the considered *k* and *R*-range. It turns out that the maximum number of independent parameters N_{ind} that can be determined from an XAFS spectrum is:

$$N_{ind} \approx \frac{2\Delta k \Delta R}{\pi} \qquad \textbf{2.7}$$

IFEFFIT is the program to perform optimization of structural parameters by minimizing the statistical parameter called *chi-squared* χ^2. The χ^2 is evaluated using the complex Fourier transforms $\tilde{\chi}(R)$ of the data and of the FEFF calculation:

$$\chi^2 = \frac{N_{ind}}{N} \sum_{i=1}^{N} \left| \frac{\tilde{\chi}(R_i)_{thy} - \tilde{\chi}(R_i)_{exp}}{\varepsilon_i} \right|^2 \qquad \textbf{2.8}$$

At each point *i* the difference between the theory and the data is normalized by the measurement uncertainty ε_i at that point.

To evaluate the difference between different fitting models which may use different numbers of fitting parameters, it is useful to evaluate the *reduced chi-square* χ^2_ν using the number of variables N_{var} actually used in the fit:

$$\chi^2_\nu = \frac{1}{\nu}\chi^2 \qquad \textbf{2.9}$$

$$\nu = N_{ind} - N_{var} \qquad \textbf{2.10}$$

The number *v* is called the *degree of freedom* of a fit. For a good fit $\chi^2_\nu \approx 1$.[19] If the χ^2_ν of the two models differ by more than a factor of $1 + \frac{2\sqrt{2}}{\sqrt{\nu}}$, then the model with the smaller χ^2_ν is better.

IFEFFIT calculates one more useful statistical parameter, an *R factor of fit*, which measures the percentage misfit of the theory to the data:

$$R = \frac{\sum_{i-1}^{N} \left| \tilde{\chi}(R_i)_{thy} - \tilde{\chi}(R_i)_{exp} \right|^2}{\sum_{i=1}^{N} \left| \tilde{\chi}(R_i)_{exp} \right|^2} \qquad \textbf{2.11}$$

The *R factor* can be helpful in determining whether the reason for a $\chi^2_\nu > 1$ is the underestimation of the measurement uncertainty σ_i or simply a poor fit. *R factor* is usually smaller than a few percent for a good fit. As seen in Figure 6.26 and Table 9 (Chapter 6), the *R factor* is between 0.6 and 1.0 percent for fits with $22<\chi^2_\nu<46$. That χ^2_ν is typically in excess of 1 is not a reason to doubt EXAFS results. Prudent use of statistical parameters such as χ^2_ν and the *R factor* combined with well constructed models and a good physical intuition make an adequate EXAFS analysis.

The results of the fitting procedure of FT EXAFS $\chi(k)$ in R space and for the back transformed signal of a Fe foil are shown in Figure 2.8. At the beginning of the fitting procedure the coordination number and the distance for the first coordination shell were fixed and then the amplitude reduction factor S_0^2 was calculated and used for the fitting of higher shells. The results of the Fe foil evaluation in comparison with *bcc* Fe crystallographic data[20] are summarized in Table 1.

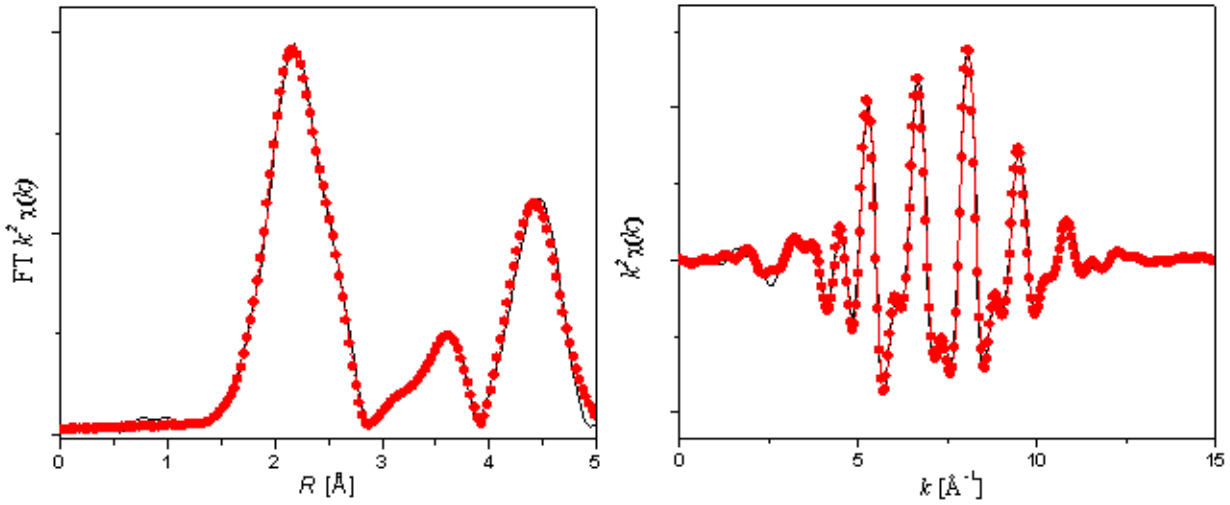

Figure 2.8 Fe foil Fourier transformation in k^2-weighting along with fit (left) and back transformed signal with fit (right), (data is solid black line, fit is circles). Uncorrected for photoelectron phase shift.

Table 1 Fit parameters of Fe foil. S_0^2= 0.870, *k*-range 2.1-11.5 Å^{-1}, R-range 1.6-5 Å.

Shells	ΔE_0 [eV]	R [Å]	N	σ^2[Å^2]	*bcc Fe*
Shell 1	3.1±1	2.470±0.005	7.1±0.8	0.005±0.0008	*R=2.49* Å *N=8*
Shell 2		2.84±0.01	5.7±1.7	0.006±0.0004	*R=2.87* Å *N=6*
Shell 3		3.820±0.09	24±0.8	0.004±0.001	*R=3.92* Å *N=24*
Shell 4		3.930±0.04	48±0.8	0.004±0.001	*R=3.92* Å *N=48*
Shell 5		4.06±0.004	10±1.2	0.006±0.0008	*R=4.06* Å *N=12*
Shell 8		4.75±0.01	20±1.2	0.007±0.0007	*R=4.76* Å *N=24*
Shell 10		4.97±0.007	7.4±1.1	0.01±0.0009	*R=4.97* Å *N=8*

2.4 X-ray Absorption Near Edge Structure: XANES

X-ray absorption near-edge structure (XANES) refers to the region of the x-ray absorption spectrum dominated by strong photoelectron scattering that extends about 30 eV above an absorption edge. XANES is of great interest in many scientific fields because it contains information about both the electronic and the geometric structure of the system of interest. XANES spectra have three characteristic features as shown in Figure 2.9: *pre-edge*, *edge*, *(*below

the ionization energy) are attributed to transitions into unoccupied orbitals, and *near-edge* XANES signal that originates from multiple scattering of the exited photoelectron and that is determined by the geometric arrangements of neighboring atoms. Transitions into unoccupied orbitals follow the dipole selection rule. In particular, for *K*- edge absorption where the initial state is a *1s* state, the photo-electron has to end up in a *p* state according to the dipole selection rule ($\Delta l = \pm 1$), that is intense edge absorption, so called *White Line* (WL). Weaker pre-edge feature results from transition to the mixing (hybridized) *p-d* orbital.

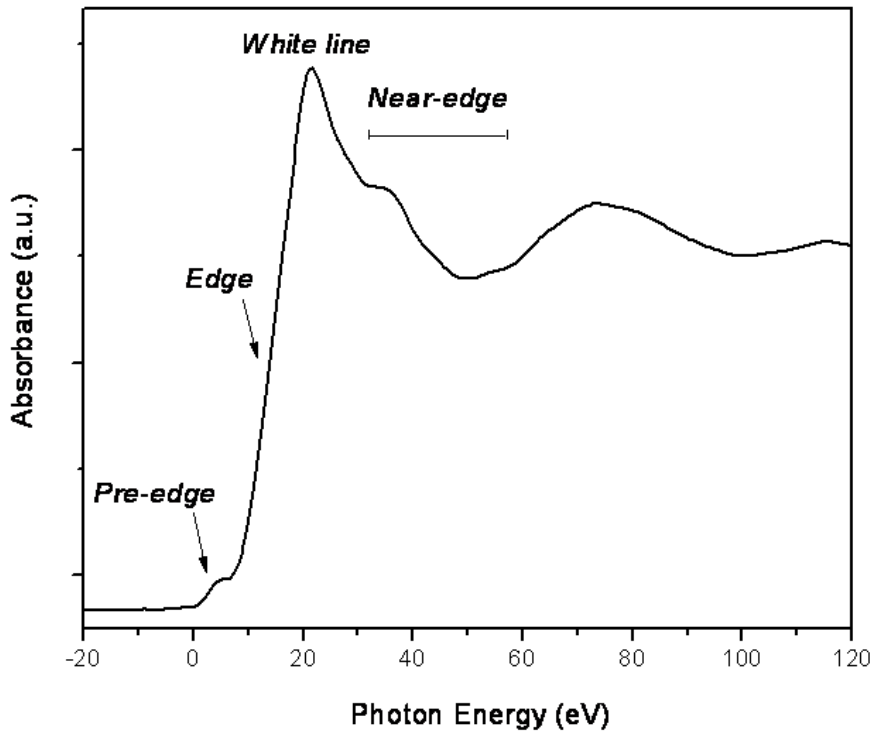

Figure 2.9 Schematic display of XANES and its main features.

It is possible to extract information about a given sample based just on a comparison of the spectrum with those of suitable reference compounds. This approach is called "*fingerprinting*". As an example, the XANES spectra for a Fe foil and different Fe oxides are shown in Figure 2.10. It is clearly seen that the position of the absorption edges is shifted to higher energies for different Fe oxides compounds with increasing formal oxidation state; this trend is known as a "chemical shift" and can be used to determine the valence. There is also a decrease of the pre-edge intensity along with an increase of the WL intensity and shift of the WL position to higher energy. Two main factors contribute to these changes:

- With participation of the valence electrons in the chemical bond formation, the core level electron is tighter bonded because of the change of the effective charge (or screening) of the nucleus. This lead to a decrease in the intensity of the pre-edge structure and to the shift of the absorption edge to the higher energy. Whereas increased WL intensity reflects a stronger contribution from the antibonding orbital into which excitation can occur.

- The energy gap between bond and antibond appears when we go from a metal to a compound explaining the shift of the WL position to higher energy.

If you have a mixture of sites/compounds in a sample you can fit the measured spectrum with a linear combinations of XANES spectra of known species and determine the proportion of each site/compound in the sample.

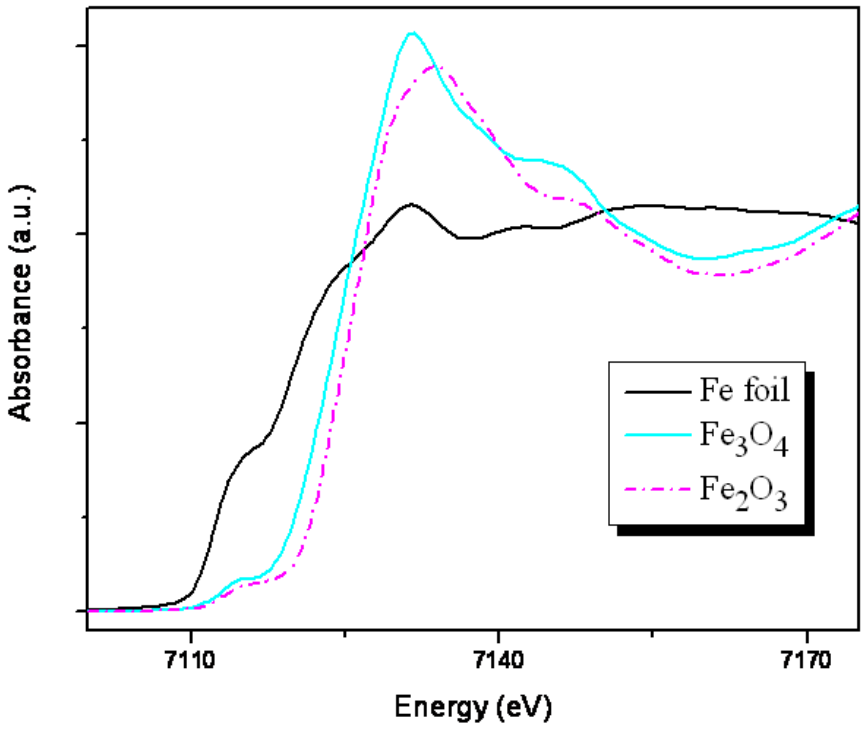

Figure 2.10 Fe K-edge XANES spectra of Fe foil and Fe oxides (hematite and magnetite).

2.5 XANES calculations using the FEFF8 code

To go beyond a "fingerprinting" method when suitable references are not available theoretical calculations of XANES spectra can be performed. All calculations shown in this work were performed using the FEFF8 code.

There are two common ways of solving the Fermi's Golden Rule equation (Eq.2.4):

1. Accurately represent |i› and |f›, then evaluate the integral directly. This is the approach taken, for example, by molecular orbital theory.
2. Use *multiple scattering* (MS) theory also known as a Green's function or propagator formalism:

$$\mu = -\frac{1}{\pi} Im\langle i|\tilde{\varepsilon}^* * \vec{r}\,\mathbb{G}(r, r'; E)\tilde{\varepsilon} * r'|i\rangle\Theta(E - E_0) \qquad \textbf{2.12}$$

where Θ is the Heaviside step function to ensure that the absorption cross section is non-zero only above the Fermi energy E_0. This step function is Lorentzian broadened to account for the lifetime of the excited core hole and the experimental resolution.

In the multiple scattering theory, all the hard work is in computing the Green's function $\mathbb{G}(r,r';E)$ as a full one electron propagator in the presence of scattering potential:

$$\mathbb{G} = G^0 + G^0tG^0 + G^0tG^0tG^0 + \ldots = \mathbb{G} = (1 - G^0t)^{-1}\, G^0 \qquad \textbf{2.13}$$

where G^0 is the free-electron propagator, the function that describes how an electron propagates between two points in space; t the function that describes how a photo-electron scatters from a neighboring atom. It is clear that Eq.2.13 contains all possible orders of scattering events. Some representative examples of possible MS paths are depicted in Figure 2.11. An arbitrary atomic lattice is shown with the absorber atom "*c*" being at the origin of the possible scattering pathways, which enter into Eq. 2.13. The first three orders in the above mentioned equation describe the scattering paths, which involve: 2 atoms (*single scattering*, (i)), 3 atoms (*double scattering*, (j)) and 4 atoms (*triple scattering*, (k)).

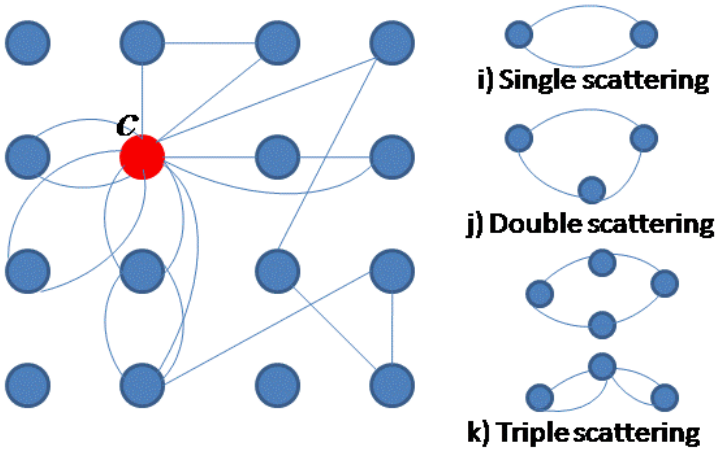

Figure 2.11 Multiple scattering in an arbitrary lattice of atoms (left). Several possible scattering paths are sketched (right: i, j, k).

Explicitly inverting the matrix $(1 - G^0t)$ and multiplying it by the G^0 matrix is called the *full multiple scattering* (FMS) approach,[21] which is computationally time consuming and is usually required only in the low energy (XANES) region. The path expansion approach, which is used in the EXAFS region allows selecting the most intense (and thus relevant) scattering contributions from the overall sum of paths as described in Eq. 2.13.

The scattering potential is calculated using *self-consistent field* method (SCF) based on the *muffin-tin* (MT) approximation, as if each particle is subjected to the mean field created by all other particles. As an input for calculating the potential a geometrical structure, which consists of a spherical scattering potential centered on each atom (Coulomb-type potential, region I in Figure 2.12 (a)) and a constant value in the interstitial region between atoms (region II in Figure 2.12 (b)) is used. According to the Norman criterion, the radii around the atoms (muffin tins radii) are chosen such that the spherically averaged charge within each radius contains an amount equal to the neutral atom. In Figure 2.12 (b), also a two-dimensional drawing of the potential energy landscape within the MT approximation is illustrated in order to highlight how the flat interstitial potential truncates the true shape of the potential. The Poisson equation for the scattering potential is solved iteratively until self-consistency is reached.

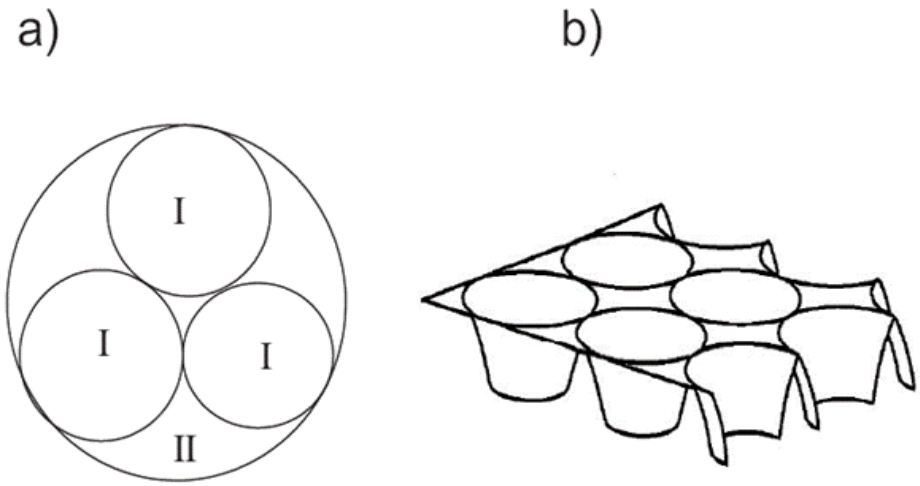

Figure 2.12 Schematic representation of muffin-tin potentials: (a) top view, including three characteristic regions; (b) 3D sketch.[21] The region I describes the atomic potentials, embedded into an interstitial region II.

In the last step, the Hedin-Lundqvist (HL) energy-dependent self-energy is added to the total potential. This is a complex exchange and correlation potential to model so called extrinsic losses, those usually approximated by the mean-free-path term in Eq.2.6. Intrinsic losses, due to the shake up processes at the central atom kept constant as S_0^2 parameter (Eq.2.6).

Chapter 3 Experiment

3.1 The synchrotron radiation source CAMD

Synchrotron Radiation (SR) is the name of the electromagnetic radiation emitted by relativistic, accelerated charged particles (electrons in our case), which move on closed curved trajectories, so called orbits, in the presence of static magnetic fields inside of a circular structure known as a *synchrotron*.

The experiments presented in this thesis were performed at the Center for Advanced Microstructures and Devices (CAMD) in Baton Rouge, Louisiana, USA. A modern synchrotron storage ring is depicted in Figure 3.1.

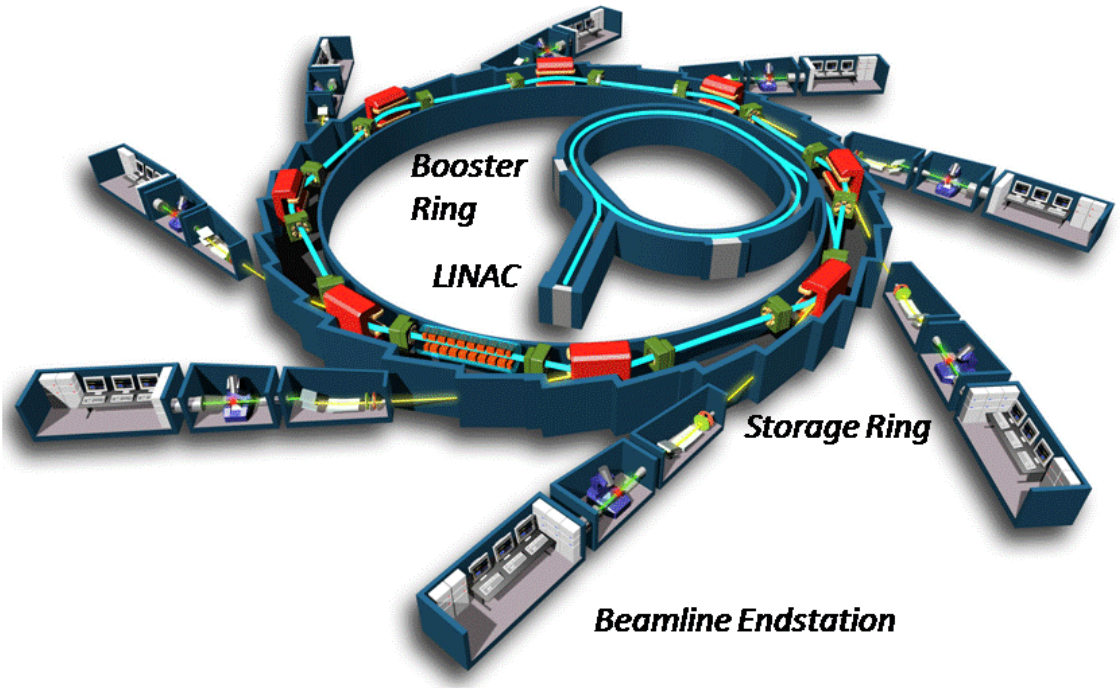

Figure 3.1 Scheme of modern synchrotron storage ring.[22]

It shows all conceptually relevant elements of the machine. Although the technical design details of CAMD are different, the basic operation scheme remains unchanged.[23] The electrons are produced in the electron gun, which injects them into the linear accelerator (commonly abbreviated as *LINAC*). The *LINAC*, accelerates an electron beam from 50 keV to 180 MeV at CAMD. The electrons then either enter a booster ring where they are accelerated up to a few GeV to be injected into a storage ring, or they enter directly into the storage ring and are accelerated there. The latter scheme is used at CAMD. In a storage ring electron beam can circulate for many hours, generating the desired SR which in turn is used at several beam-line endstations simultaneously.

The main characteristic parameters of the CAMD ring are summarized in Table 2.

Table 2 Main parameters of the CAMD ring.

Parameters	
Ring energy (GeV)	1.3
Maximal current (mA)	250
Lifetime (min)	600
Dipole magnet field (T)	1.48
Dipole magnets bending radius (m)	2.928
Characteristic energy (keV)	1.66
Characteristic wavelength (Å)	7.45

The general shape of the radiation spectra of an electron moving in a curved trajectory of CAMD operated at the typical parameters of 1.3 GeV is shown in Figure 3.2.[24]

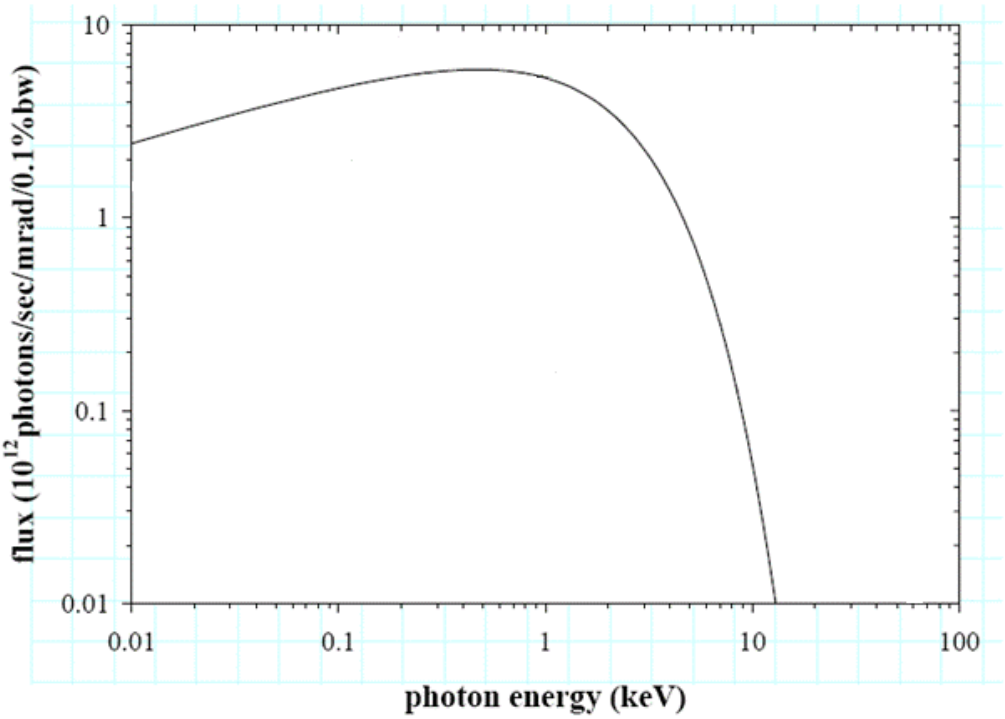

Figure 3.2 Calculated synchrotron-radiation-flux curve for synchrotron radiation from the CAMD source. Note the spectra are normalized to 200 mA ring current and 1 mrad horizontal acceptance.[24]

3.2 Collection geometries

An X-ray absorption spectrum is generally collected by measuring the variation in the absorption of monochromatic X-rays as the energy of incident photons is varied. Figure 3.3 shows a XAS experiment in both the transmission and fluorescence geometry.

Ion chambers measuring the number of photons passing through them are placed before and after the sample. *Keithley* 617 electrometers are connected to these ion chambers providing analog signals. The first ion chamber (I_0) is shorter compare to the second to absorb approximately 20% of the incident flux. The second ion chamber (I, after the sample) absorbs 80% of the incident flux. The x-ray absorption coefficient $\mu(E)$ can be derived according to the *Lambert-Beer* law (Eq.2.1) as:

$$\mu(E) = \ln \frac{I_0}{I} \qquad 3.1$$

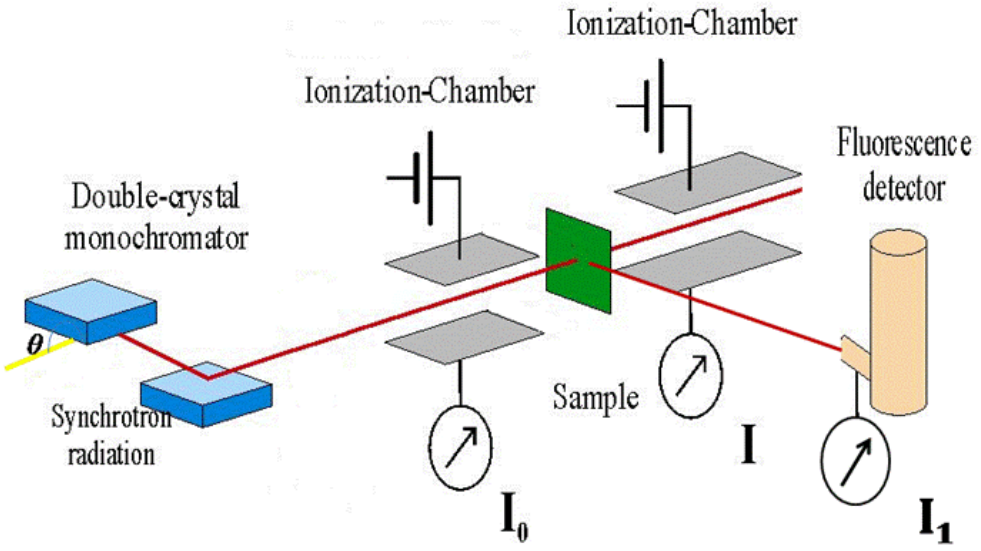

Figure 3.3 Schematic representation of XAS experiment in the transmission and fluorescence mode.

Below a certain level of concentration, the change in the absorption before and after the edge will become very small in the transmission technique and therefore the signal-to-noise ratio is poor. Whereas, the x-ray fluorescence signal is absent before the edge (if there are no others shells), and present after the edge and so the ratio is greater than in the transmission mode. In both cases I_o is still used as the reference. For fluorescence, photons produced by the element of interest during absorption are detected with a solid state detector (Figure 3.3). The detector is typically positioned orthogonal to the incident beam in the plane of the synchrotron to minimize the scattered background,[25] while still detecting the fluorescence. The dependence of the x–ray absorption coefficient μ in fluorescence mode can be estimated as:

$$\mu(E) = \frac{I_1}{I_0} \qquad 3.2$$

where I_1 is the intensity of a fluorescence associated with the absorption process.

3.3 The double crystal monochromator

Monochromatic radiation is provided with a double crystal monochromator (schematically shown in Figure 3.3) of the Lemmonier type.[26] For data collected at the Co K-edges (7709 eV), Ge(220) crystals (planar spacing $2d$ = 4 Å) were used. For data collected at the S K-edge (2472 eV), InSb(111) crystals ($2d$ = 7.48 Å) were used.

The monochromator selects the Bragg angle θ_B for the desired photon energy E (wavelength λ) according to the Bragg's law (illustrated in Figure 3.4). Through the rotation of the first crystal in appropriate range of θ the energy is scanned while the second crystal stays parallel to the first, so

that the beam is re-diffracted in the direction parallel to the incident white radiation and the beam position at the sample remains the same.

The Bragg reflection condition describes an ideal situation, i.e. if a spectrum of radiation falls under a Bragg angle thus only a sharp energy E is selectively reflected. In reality, a certain distribution centered around *E* is reflected with a certain probability. This probability of the radiation to be reflected is called reflectivity, and its dependence as function of the angle of incidence is the Rocking Curve (RC). The Rocking Curve for Ge(220) crystal is present in Figure 3.5. The dynamical scattering theory describes the reflectivity and the width of the RC as:

$$\omega = \frac{2}{sin2\Theta_B}\frac{r_e\lambda^2}{\pi V}C\left|F_{ref}\right|e^{-M} \qquad \textbf{3.3}$$

where $r_e=e^2/mc$, V is the unit cell volume, C is the polarization factor (1 or $\cos 2\theta_B$ for σ or π polarization, respectively), F_{ref} and e^{-M} is the crystal structure and the Debye-Waller factor for the crystal.

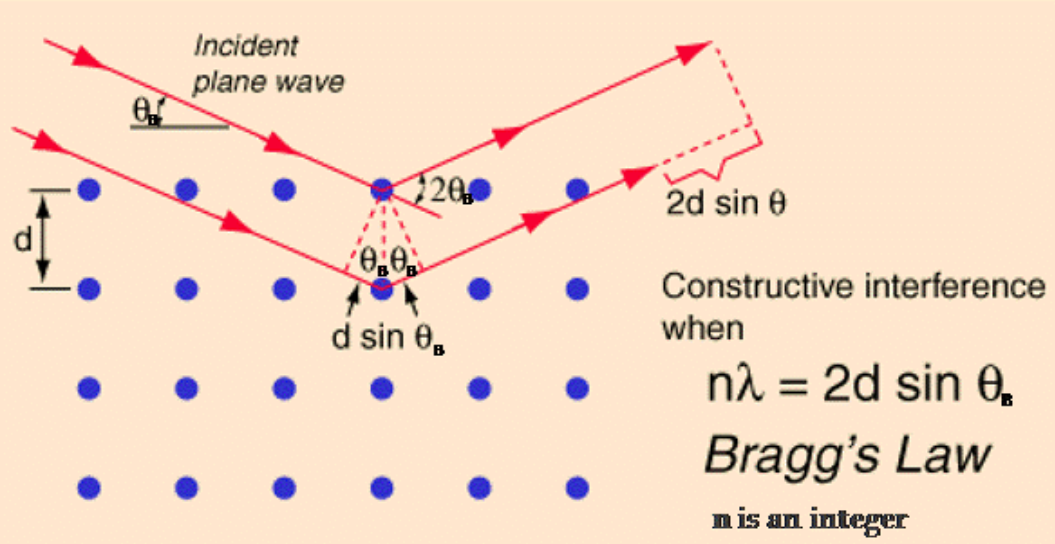

Figure 3.4 Illustration of Bragg's Law.

From Figure 3.5 it can be seen that with decreasing photon energy (increasing λ) the peak reflectivity is decreasing and the rocking curve width is increasing. The asymmetry of the reflection curves is due to the crystal absorption.[27] In addition, the rocking curve center is deviated from the Bragg angle for θ-θ_B due to refraction.

Another important parameter is the energy resolution of the monochromator. The energy resolution is given by the differential form of the Bragg equation:

$$\frac{\Delta E}{E} = \frac{\Delta\lambda}{\lambda} = \Delta\theta\ \cot\left(\theta_B\right) \qquad \textbf{3.4}$$

here E is the desired photon energy.

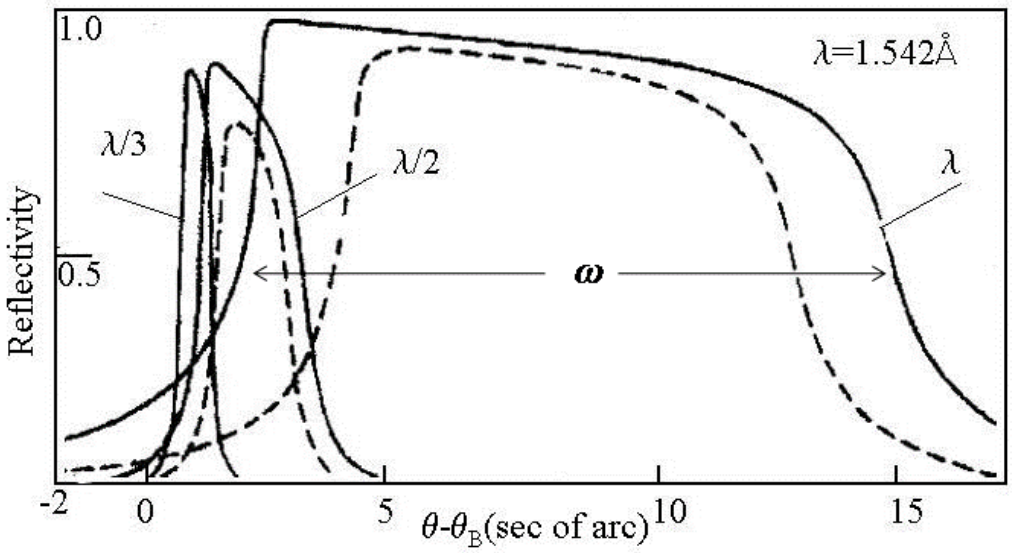

Figure 3.5 Rocking curve for Ge(220) crystal reflection (solid line– σ polarization, dash line-π polarization) [28] (θ is the actual angle of incidence, θ_B is the angle calculated from the Bragg Law).

The angular spread of the incoming beam Δθ, is due to the vertical divergence of the x-ray source and the rocking curve width of the monochromator crystals. The vertical divergence of the x-ray source can be varied by means of slits before the monochromator. Thus energy resolution is lost by opening the vertical slits too wide. A compromise should be found in maximizing the number of photons through the slits and maximizing energy resolution. When two scans of the sample are taken and slit are closed by some amount between the scans, it will be obvious if resolution was comprised by the original slit size if the features around the edge are noticeably sharper in the scan with narrower slit. The slit should be closed until no change in resolution of scans is observed. For XANES you want high resolution and may sacrifice flux, while for EXAFS you don't need high resolution so you sacrifice it and maximize flux.

3.4 The end station of the XMP beamline for spatially-resolved XAS

Beyond regular XAS experiments, the end-station of the XMP beamline is also designed to conduct *spatially-resolved* XAS experiments in transmittion and fluorescence mode. A photo of the end-station is shown in Figure 3.6.

The incident x-ray beam (indicated by an arrow) passes through motorized vertical and horizontal slits (MS). Usually widths of the slits are set to the acceptance of the Kirkpatrick-Baez focusing system (KB), which consist of vertical (KBV) and horizontal (KBH) focusing mirrors. In the case of ~7700 eV photon energy (for Co K-edge) and respective to this energy reflectivity of gold coated mirrors,[29] appropriate incident angle is ~8 mrad.[30] With a mirror length of 100 mm, this leads to a maximum slit width of 800 μm. The KB-focusing system is the most important optical part of the microprobe end-station; more detailed information will be given below. After being focused, the beam travels through an ionization chamber (IC) and impinges on the sample. The sample is mounted on the sample holder (SH), which is located on a motorized goniometric sample stage assembly. The sample stage assembly is positioned under 45° to the incident beam. It consists of two translation stages (x, z) with the resolution better than

1 μm. A *Canberra* single element Ge-detector (GE) for fluorescence detection is positioned 90° to the incident beam in the plane of the synchrotron ring. An optical microscope (MI) (*Model-No N536593, IaI-Corporation, CV-S3200, 12V*) points at the sample under 45° to the incident beam. The image is displayed on a video monitor outside of the experimental hutch.

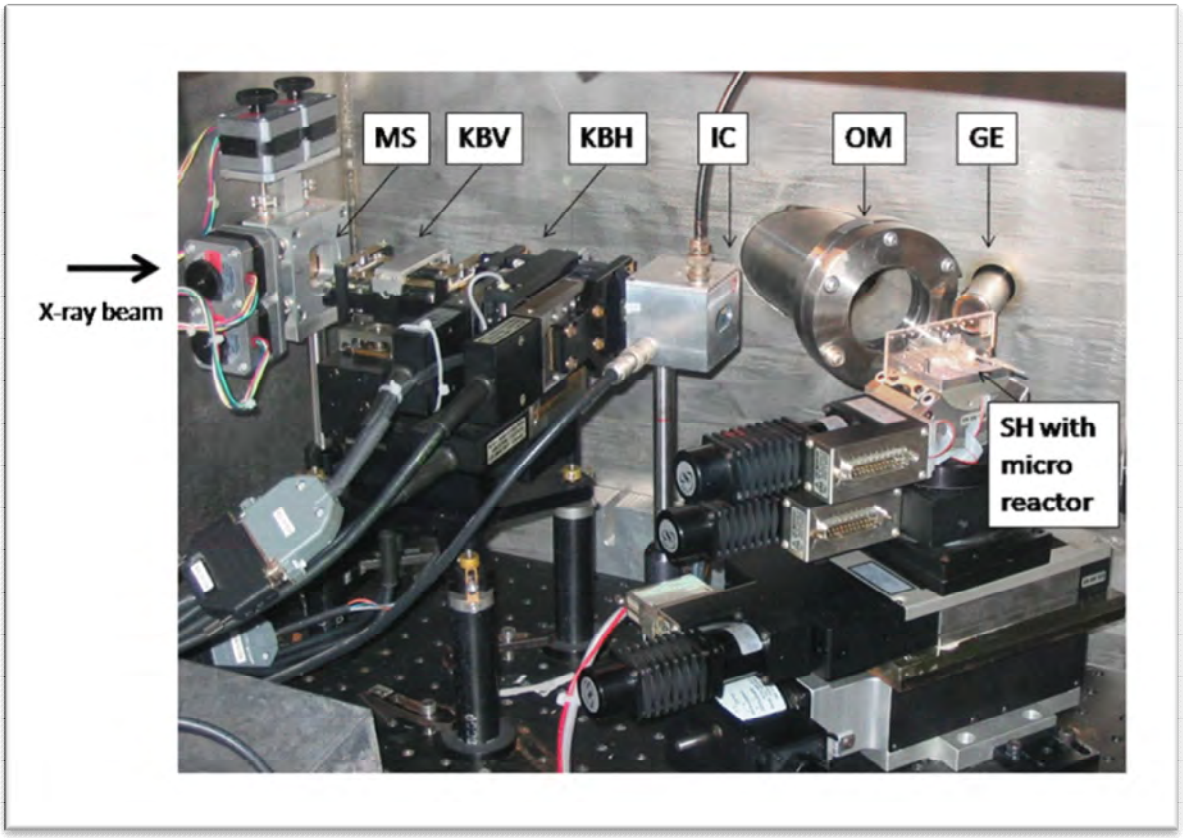

Figure 3.6 The experimental set up of the XMP beamline end-station for spatially-resolved XAS experiments.

3.4.1 The Kirkpatrick-Baez focusing system

The Kirkpatrick-Baez focusing system is based on grazing incidence total reflection mirrors. A pair of elliptical mirrors is arranged in the perpendicular Kirkpatrick-Baez geometry[31] and sequentially focusing incoming radiation in horizontal and vertical directions (Figure 3.7).

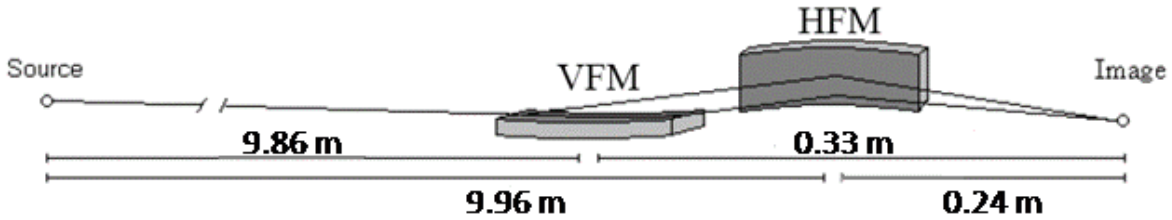

Figure 3.7 The geometry of the Kirkpatrick-Baez focusing system.

To achieve a focused image it is necessary to satisfy the focus equation at the center of the first and second mirrors:

$$\frac{1}{f_1} + \frac{1}{f_2} = \frac{2}{R_1 sin\theta_{inc}} \qquad \textbf{3.5}$$

f_1 , f_2, are clear from the geometry schematically shown in the Figure 3.8, θ_{inc} is the incident angle, R_1 is the mirror radius of curvature.

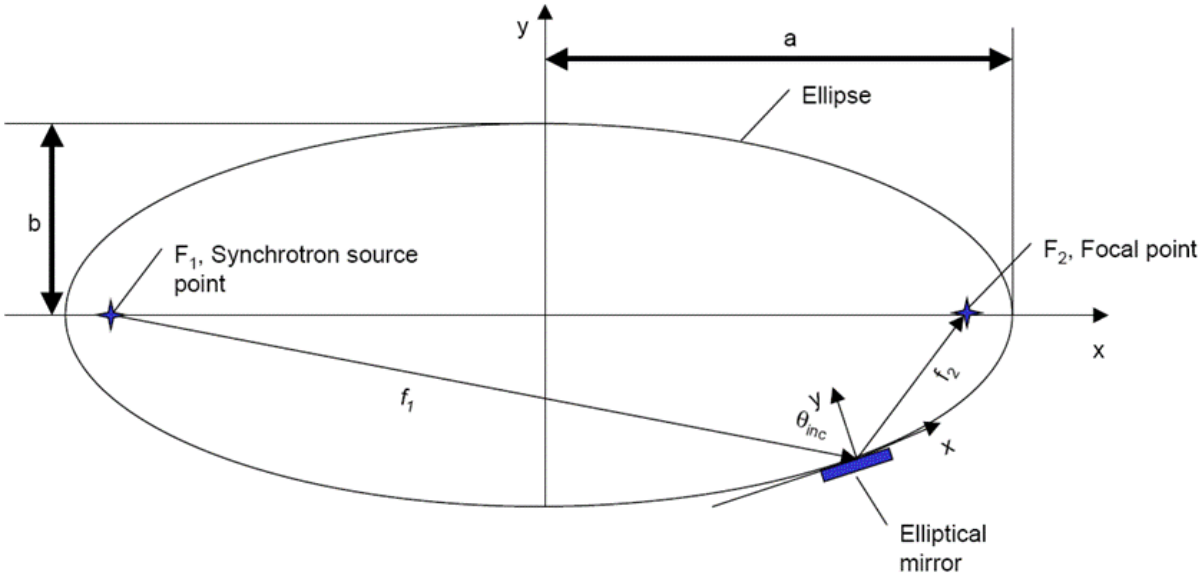

Figure 3.8 The geometry of ellipse, focusing the rays emitted from F_1 to the focal spot F_2.

The demagnification of the optical system is simply given by

$$M_D = \frac{f_1}{f_2} \qquad \textbf{3.6}$$

In the current optical system of the XMP beamline the horizontal and vertical demagnifications are *MDH*~41.5 (*f1H*/*f2H*=9.96m/0.24m) and *MDV*~30 (*f1V*/*f2V*= 9.86m/0.33m), respectively (see Figure 3.7). These result in a theoretical horizontal and vertical focal spot size of σ_{xF}=10.8 μm and σ_{zF}=13 μm, based on the horizontal and vertical source sizes of σx=450 μm and σz=390 μm (private communication V. Suller, Associate Director, CAMD).

For the experiment presented in this work the desired elliptical shape of the mirror is produced by the controlled bending of flat mirrors. The focused beam profiles were measured by performing knife-edge scans using an Fe foil of 50 μm thick mounted on the sample holder. During the knife-edge scans a photo-diode was placed after the Fe foil to monitor the intensity of the transmitted x-rays while moving the Fe foil in vertical (vertical knife-edge scan) or horizontal (horizontal knife-edge scan) direction. As the Fe knife-edge is moving into the beam, the intensity of the transmitted beam decreases until it reaches zero when the Fe knife-edge fully blocks the focused beam. Figure 3.9 and Figure 3.10 present the focused beam profile derived from the derivative of the measured transmittance along the vertical and horizontal knife-edge scans, respectively, at photon energy of 7700 keV. A vertical focal beam spot size σ_{zF} of 25 μm (50 μm FWHM) and horizontal σ_{xF}=35 μm (70 μm FWHM) were achieved.

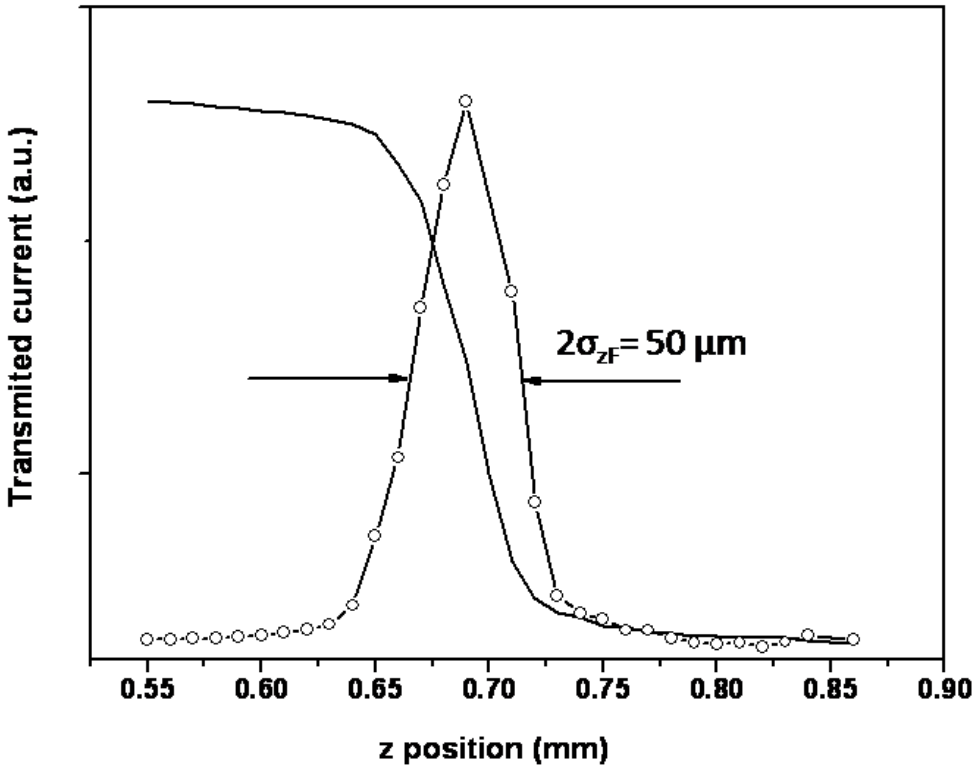

Figure 3.9 The vertical knife-edge scan (solid black line) and its derivative (solid black line with symbol ○).

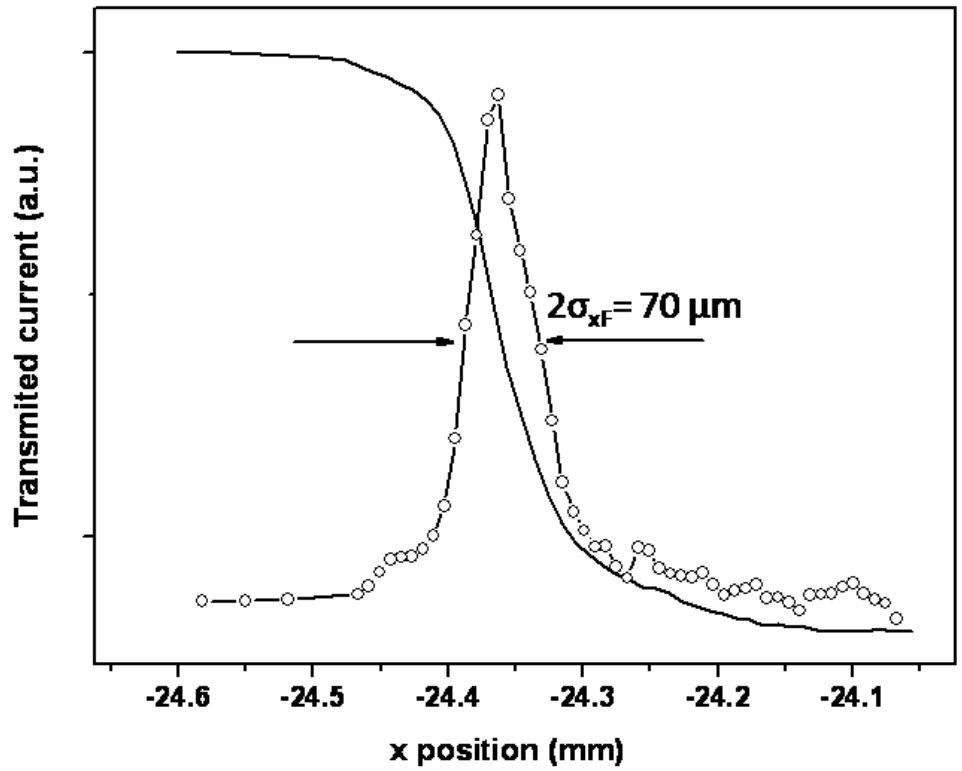

Figure 3.10 The horizontal knife-edge scan (solid black line) and its derivative (solid black line with symbol ○).

In the current experimental set-up (Figure 3.6), the sample stage is positioned under 45° to the incident beam. Therefore, in order to determine the horizontal travel of the sample stage in the x-direction, a correction factor of sin45° was used. Figure 3.10 shows already corrected values.

Deviations from the ideal surface, commonly expressed as slope error of the mirror surface as well as surface roughness led to an oversized focal spot compare to the predicted theoretical values. In the scope of this work these parameters were not determined.

3.5 Sample preparation

A proper sample preparation for a transmission experiment is essential for collection of high quality data. In order to make appropriate choices for the composition and form of the sample it is necessary to know both the absorption length and its edge step absorption length.

We need a sample that is of uniform and appropriate sample thickness of ~2 absorption lengths to get the best signal to noise ratio.[32] One absorption length is 1/μ, distance over which x-ray intensity incident upon a sample at an energy ~50 eV above the absorption edge decreases by factor 1/e ~ 37%. Suppose we assume we want a sample with 2 absorption length thickness, then mass of the sample: $m = \frac{2A}{\mu_m}$, where μ_m-mass absorption coefficient,[29] *A*-sample area. For Co μ_m at 50 eV above the edge (~7760eV) is 345.7 cm^2/g and using a sample 1.5 cm x 1 cm, so that A = 1.5 cm^2, then *m*= 3/345.7=0.0086g=8.6μg.

However to minimize systematic errors due to sample thickness,[33] $t\Delta\mu$, the change in absorption across the edge, should be ≤ 1 (*t*- is the width of the sample). By "*thickness effect*" is meant that part of the signal that is not attenuated in the sample as much as expected and might cause significant distortions in EXAFS amplitudes. This could be due to holes or varying thickness in the sample. Clearly both these criteria cannot be always satisfied. Of these two criteria, the one resulting in the thinner sample is chosen.

One of the common preparation methods is thin layers. The sample is grounded to a very fine powder; spread as a thin, even layer on the adhesive side of a tape and folded several times.

A liquid sample can be measured using a special cell.[34] The thickness of this cell might be varied respective to the desired one.

Chapter 4 Synthesis of nanoparticles

4.1 Wet chemical synthesis of Co nanoparticles for time-dependent investigation of the reaction pathway

Co nanoparticles were synthesized via established thermolysis of metal carbonyl precursors in the presence of aluminum alkyls.[35] In order to investigate a "bare" mechanism of Co nanoparticles formation the last step, so called "smooth oxidation" procedure (details are given below) was not applied at the end of these syntheses.

Dicobalt octacarbonyl [$Co_2(CO)_8$] (DCO), aluminum tryoctal [$Al(C_8H_{17})_3$] and toluene were purchased from Alfa Cesar. The alkyne-bridged dicobalt hexacarbonyl compound [(Co_2(μ-HC≡CH)$(CO)_6$] (ADH) was prepared using the procedure reported in the literature.[36] Typical procedure used for the decomposition of organometallic precursors leading to cobalt nanoparticle formation is as follows. In a 500 ml three-necked flask fitted with a mechanical stirrer and a reflux condenser [$Al(C_8H_{17})_3$] (4.4 ml (10 mM)) was dissolved in 300 ml of toluene under nitrogen and heated to 90 ^{0} C. [$Co_2(CO)_8$] (17.1 g (100 mM)) was introduced under a flow of nitrogen. After 10 minutes of stirring the mixture at 90^{o}C, the temperature was gradually increased up to 110 ^{0}C and was maintained for 18 hours. With the evolution of CO, the color of the solution changed from dark red to dark brown and then to black followed by formation of a black precipitate.

Samples of 30 mL for XAS, TEM and SQUID measurements were taken at regular intervals (2min, 3 hours, 6 hours, 9 hours, 12 and 18 hours) without any interruption of stirring and under nitrogen flow. Samples were cooled down to 20 ^{0}C and particles were decanted and washed three times with 30 ml of ethanol (except 2 min sample, where no precipitation of the particles was observed and it was kept in a liquid phase). Synthesis with the same ratio of reactants and identical reaction parameters was repeated for the ADH precursor. Samples with the same time-intervals were obtained. Due to high air sensitivity of Co nanoparticles preparation of the samples for XAS and SQUID measurements were done in a glove box and measurements were carried out under nitrogen atmosphere.

In Table 3 the size distributions D and deviations σ of the DCO and ADH particles are present. A typical TEM images and diagrams of size distribution for 9 and 18 hours samples of both DCO and ADH synthesis are displayed in Figure 4.1 and Figure 4.2.

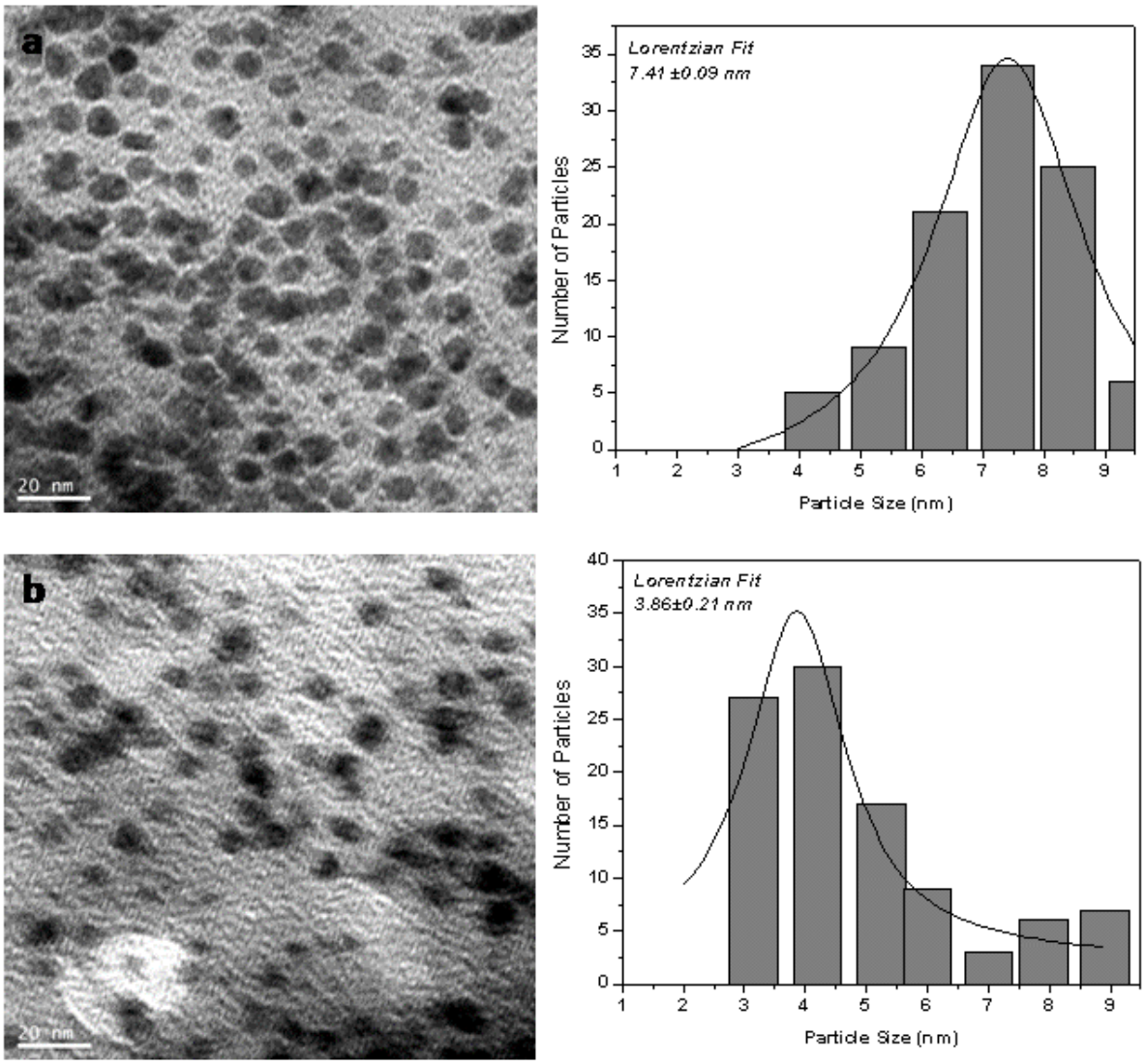

Figure 4.1 TEM images and histograms of size distribution: (a) "DCO 9h"; (b) "DCO 18h".

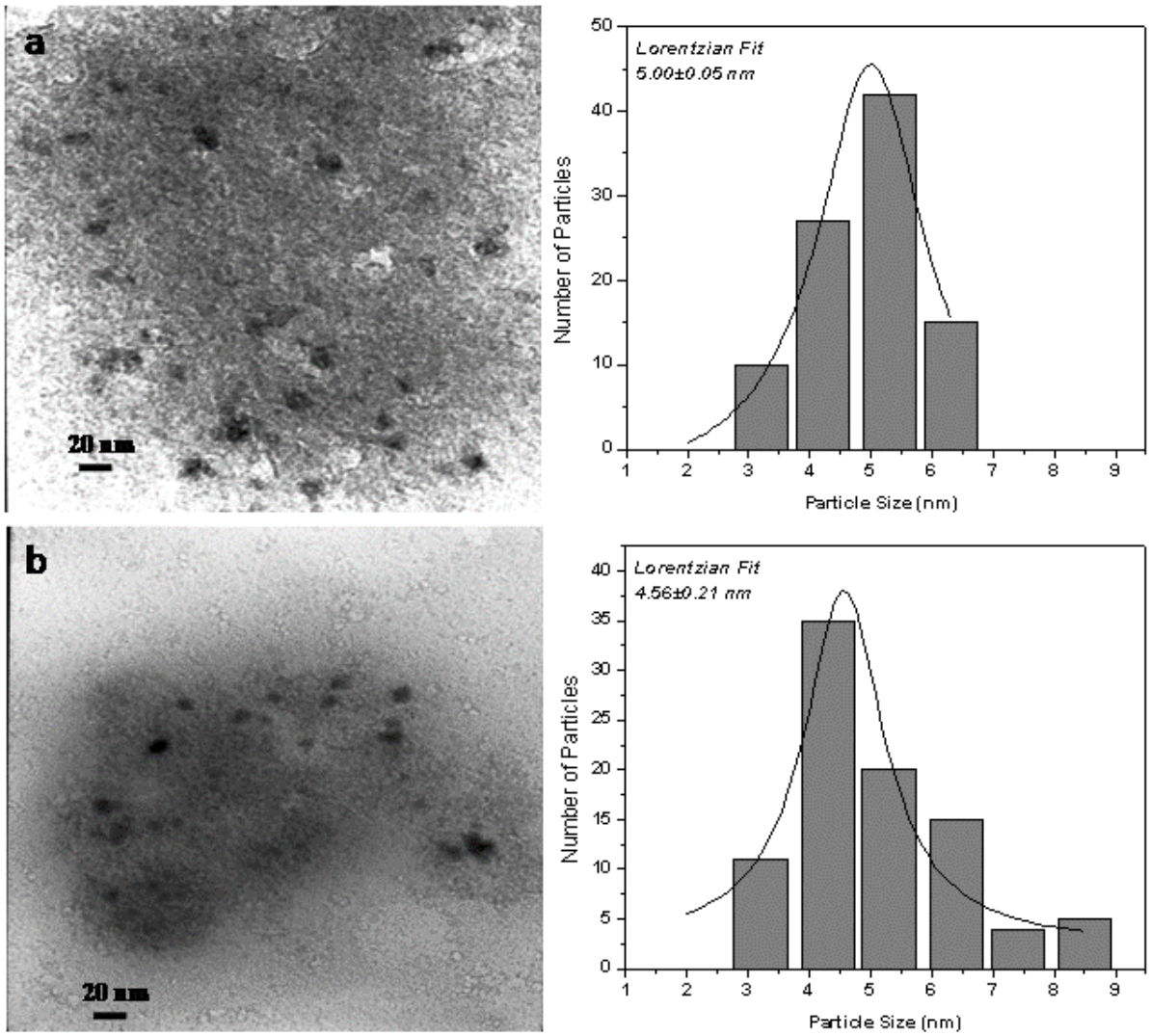

Figure 4.2 TEM images and histograms of size distribution: (a) "ADH 9h"; (b) "ADH 18h".

Table 3 Time-dependent size distributions D and deviations σ of DCO and ADH syntheses.

Time	DCO, D ± σ, (nm)	ADH, D ± σ, (nm)
2 min	—	—
3 hours	1.78±0.01	4.49±0.09
6 hours	5.26±0.40	6.51±0.01
9 hours	7.41±0.09	5.00±0.05
12 hours	5.81±0.07	4.98±0.12
18 hours	3.86±0.21	4.56±0.21

An interesting feature is observed for both reactions. Although, it is generally believed that with time particles will grow via agglomeration or Ostwald ripening, when the larger particles are growing at the expense of dissolving smaller ones, the mean particle size is found by TEM analysis to be increasing from 3 hours up to 9 hours of the syntheses, but no size increase or agglomeration was detected further with time.

4.2 Surface modification of Co nanoparticles for biomedical applications by L-cysteine ethyl ester

Co&L-cysteine nanoparticles were synthesized via the same thermolysis (see above 4.1) including the "smooth oxidation" procedure.

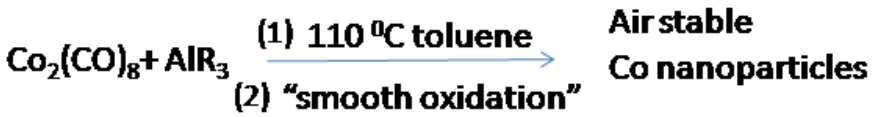

"Smooth oxidation" is a controlled oxidation of the resulting nanoparticles with synthetic air (80% O_2 and 20% N_2) bubbled through a capillary into the reaction mixture after it has been cooled down. This procedure creates a protection CoO like shell around the cobalt core, which prevents further oxidation of the metallic core.

After that 5 mL of obtained Co nanoparticles suspended in toluene were washed three times with 5–10 ml ethanol to remove toluene, followed by washing two times with 10 mL of air-free nanopure water to remove any ethanol. After washing, the particles were peptized, by adding 10 mL of aqueous L-cysteine ethyl ester solution (2% L-cysteine ethyl ester in water) and stirring.

4.3 Water based synthesis of Co nanoparticles for microfluidic reaction

Because the mechanism of nanoparticles formation highly depends on reaction conditions (such as reagents, surfactant, temperature, and solvent) a more complete and more general picture of what happens during the nanoparticles formation was investigated using a reaction completely different from thermolysis of cobalt carbonyls. An established batch sodium borohydride reduction of cobalt acetate in an aqueous medium at room temperature was adapted for synthesis in a continuous flow microfluidic reactor. It is a highly reproducible and easy to control reaction, moreover simple for scaling up process, where synthetic procedures without too many complicated steps are preferable.

Cobalt (II) acetate [$Co(CH_3COO)_2$ - $4H_2O$], N-dodecyl-N,N-dimethyl-3-ammonio-1-propanesulfonate [$C_{17}H_{38}NO_3S$] (SB12) and sodium borohydride [$NaBH_4$] were purchased from

Sigma-Aldrich. According to the Son *et al.*[37] procedure, 5.25 g cobalt (II) acetate was mixed with 2.184 g of SB12, as a surfactant, in 700 ml of air-free nanopure water in a three-necked 1000-ml flask by sonicating under nitrogen until completely dissolved. A reducing agent was prepared separately by combining 1.05 g sodium borohydride [$NaBH_4$] with 210 ml of air-free nanopure water under nitrogen. The reaction proceeds upon drop-wise addition of a reducing agent to the solution of cobalt acetate and surfactant. The light- pink solution of cobalt acetate and SB12 starts to turn black instantly upon addition of reducing agent.

From the reaction mixture the black precipitate was allowed to settle, by setting on top of a permanent magnet for several hours (until completely settled) and the transparent supernatant was decanted. Co nanoparticles were isolated, washed three times with 100 ml ethanol, and dried under nitrogen. Due to air sensitivity particles were kept in a glove box. The size of the particles was estimated with the aid of MetaVue software using 300 nanoparticles and the obtained averaged particles size was 4.13±0.15 nm. A TEM image and a diagram of size distribution are present in Figure 4.3.

For the microfluidic reaction the reactant solutions had the same composition as used in the batch process. Through the two inlets (A and B Figure 4.4) the flow of cobalt acetate and SB12 is combined with the flow of reducing agent (at the point d) and follows by a mixing in a "serpentine" section toward outlet (C). The reagents and microreactor final product were kept under nitrogen flow. Co nanoparticles were isolated in a powder form through the similar procedure described above for the batch reaction.

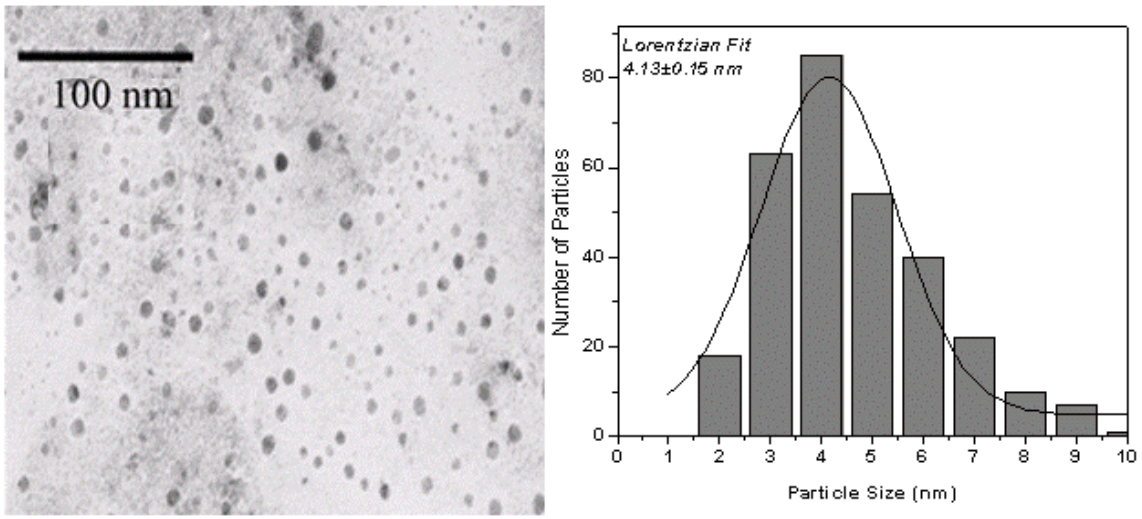

Figure 4.3 TEM image and size distribution diagram of water based Co nanoparticles resulting from the batch process.

4.4 Microreactor design and parametrs

The microreactor structure was fabricated in a standard format microfluidic experimental platform at CAMD. Components for the reactor were molded in (polymethyl metacrylate) PMMA by a hot embossing process. The molding tool was fabricated by directly milling a brass disc on a Kern[38] micromilling machine. This molding tool was then used in a Jenoptik HEX02[39] hot embossing machine to mold the components.Figure 4.5 outlines the sequence of processing

steps. Polymer molding in the form of hot embossing was the key technology used to fabricate the microfluidic chip. High accuracy, low stress parts, simple and fast mold design of hot embossing procedure make hot embossing the ideal choice for rapid prototyping and for applications where small batches of parts are desired. The scheme of hot embossing process is present in Figure 4.6. It consists of using a temperature controlled press to transfer a pattern from a metal template (mold) to a polymer sheet. The Jenoptik Mikrotechnik HEX02 machine, where all hot embossing activities were carried out is designed specifically for molding high aspect ratio micro and nano structures in polymers. The machine is capable of precisely controlling the pressing motion (1 μm resolution), temperature uniformity (±2°C over a 100 mm dia. molding area), and is equipped with advanced demolding capabilities. Micro-molding is done under vacuum to keep air from being trapped in the microstructures which would result in poor mold filling and voids in the molded part.

The machine allows continuous control and measurement of all the above parameters during the molding process, thus resulting in a high degree of repeatability. The HEX02 data acquisition system continuously measures the temperatures and relative position of the insert and polymer during the molding cycle.

Because of biological compatibility, optical properties, and ease of molding commercially available 3/16" thick PMMA sheet material (Atofina, Plexiglas) was chosen as a molding material. Being a common material for molding, the molding conditions for PMMA are well documented.[40]

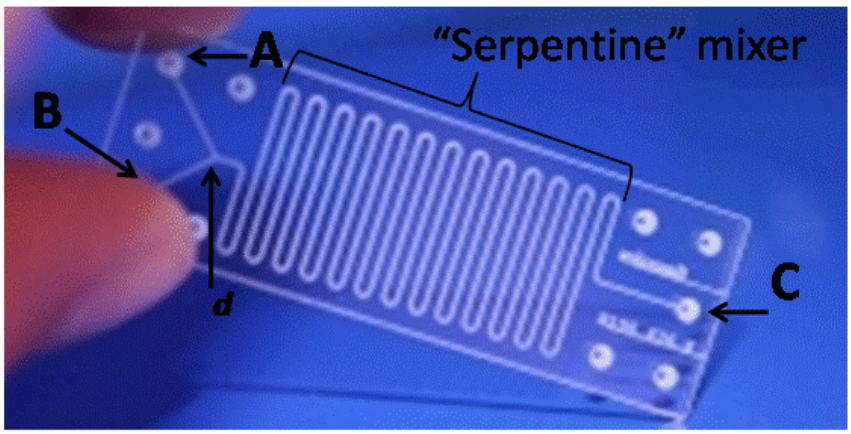

Figure 4.4 Microfluidic reactor for the synthesis of nanoparticles.

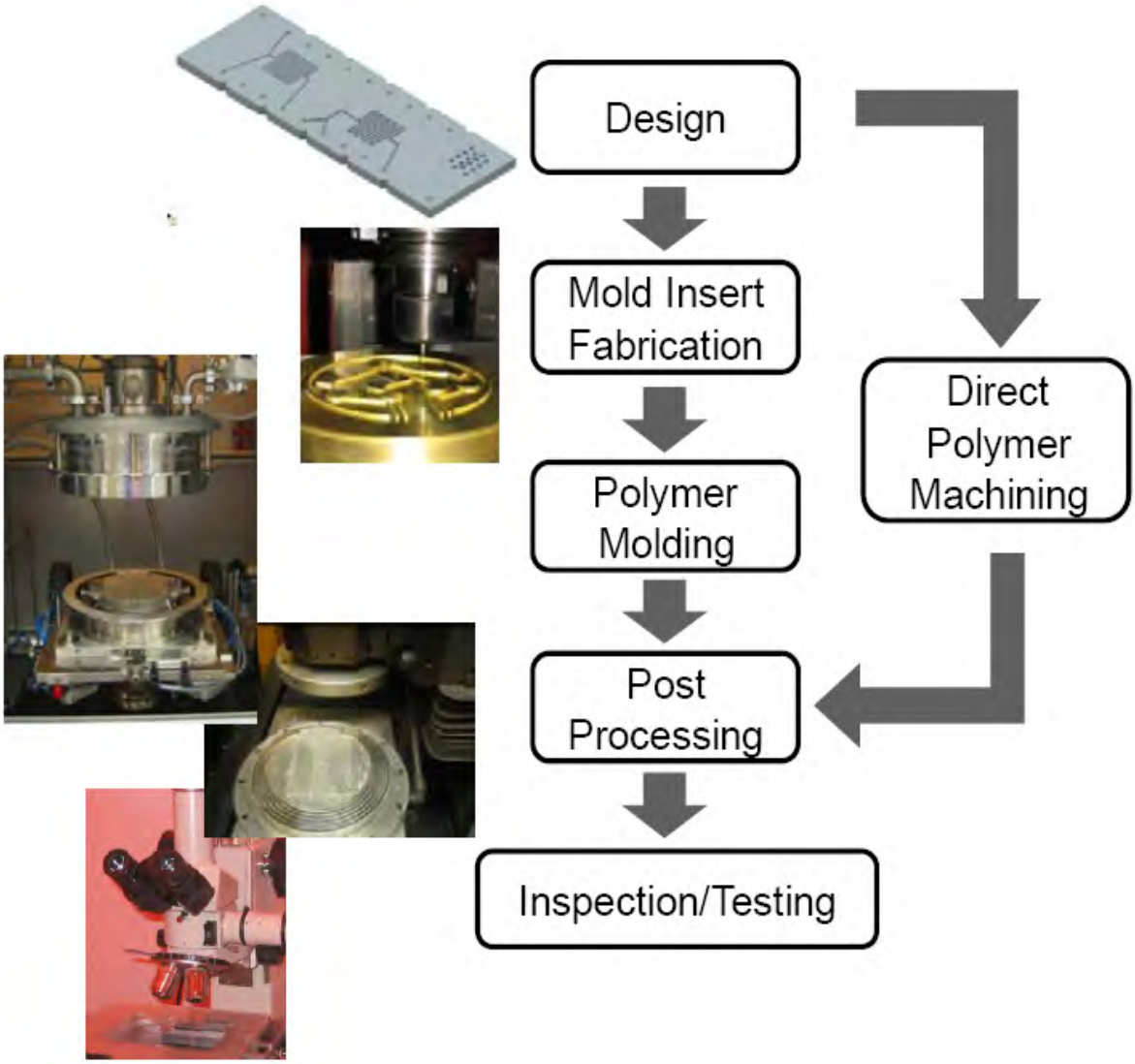

Figure 4.5 Sequence of fabrication steps for the components of the microfluidic system[41]

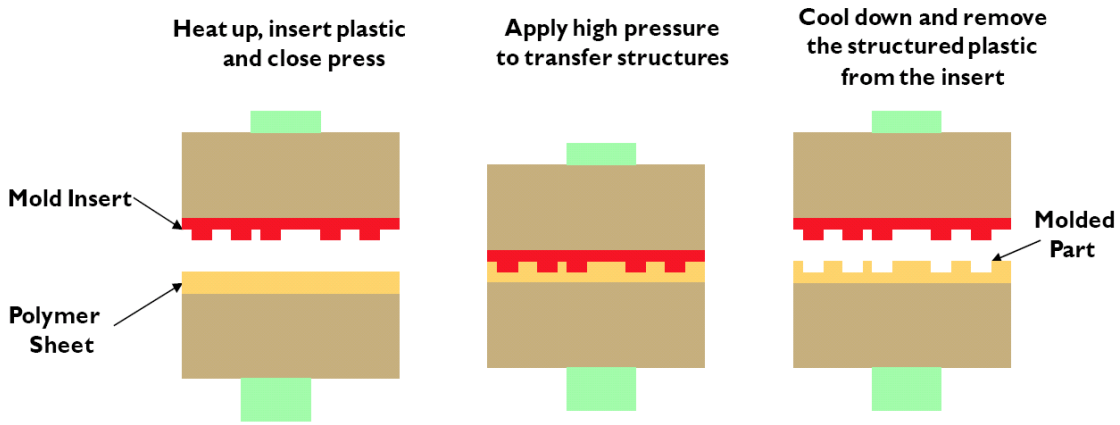

Figure 4.6 Scheme of hot embossing process.[41]

Micromilling of brass discs was chosen as the primary method of mold fabrication. Micromilling can be used to produce molds in various metals. It is by far the most flexible and quickest method which makes it a very attractive technology in spite of the fact that the resolution and surface polish achieved by micromilling is poorer than that achievable by lithography based methods. Dimensions as small as 25 micron wide and aspect ratios of up to four can be achieved by micromilling. Brass is the material of choice for milling the mold because of its easy machinablity and good performance in the hot embossing process.

Micromilling of brass blanks was done on the Kern Micromilling machine using a 40,000 rpm spindle. The machine is capable of positional and repetition accuracy with a precision of ±1 µm in a space of ~150 mm^3. Micromilling is a rapid and inexpensive method of fabricating microstructures mold inserts for prototyping and small scale production. Fabrication time for an average mold insert is 2-6 hours.

After replicating polymer parts by hot embossing, they have to undergo a sequence of steps before they are ready for use in the system. The common process all chips undergo is machining and cleaning.

The reactor consisted of 2 discrete microfluidic chips:

1. An interconnect chip consisting of fluidic ports to connect tubing (Figure 4.7)
2. A microfluidic reactor chip (Figure 4.8)

The designed microfluidic reactor chip includes the channels (Figure 4.8) dimensions of 200x200 µm (left) and 500x500 µm (right), but only 500x500 µm channel was used in the current experiment. The interconnect chip with fluidic ports was sealed to the reactor chip to form the microfluidic stack.

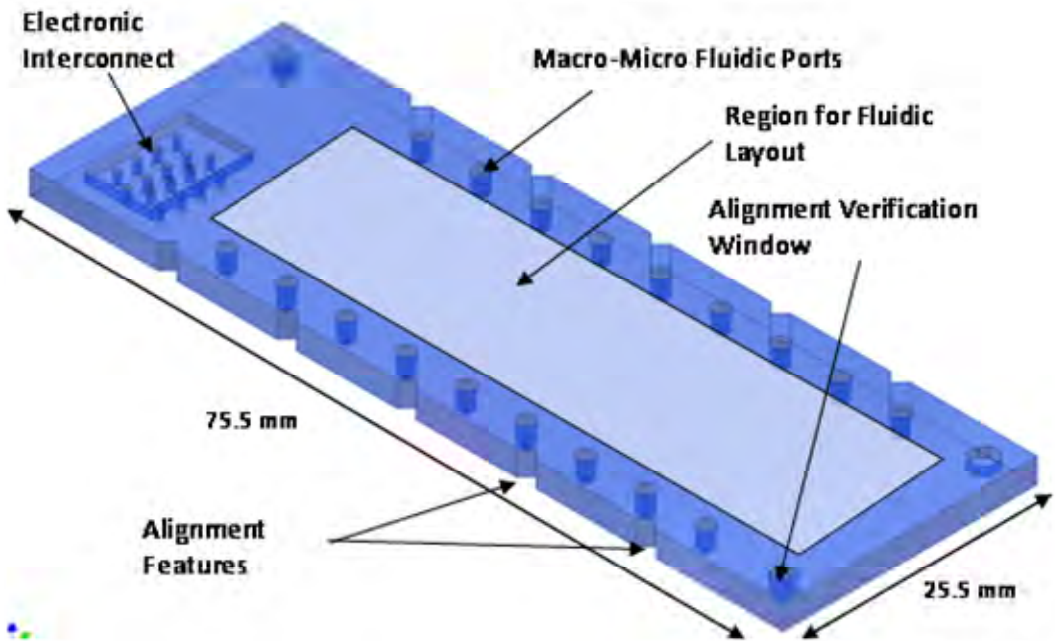

Figure 4.7 Scheme of interconnect chip.[41]

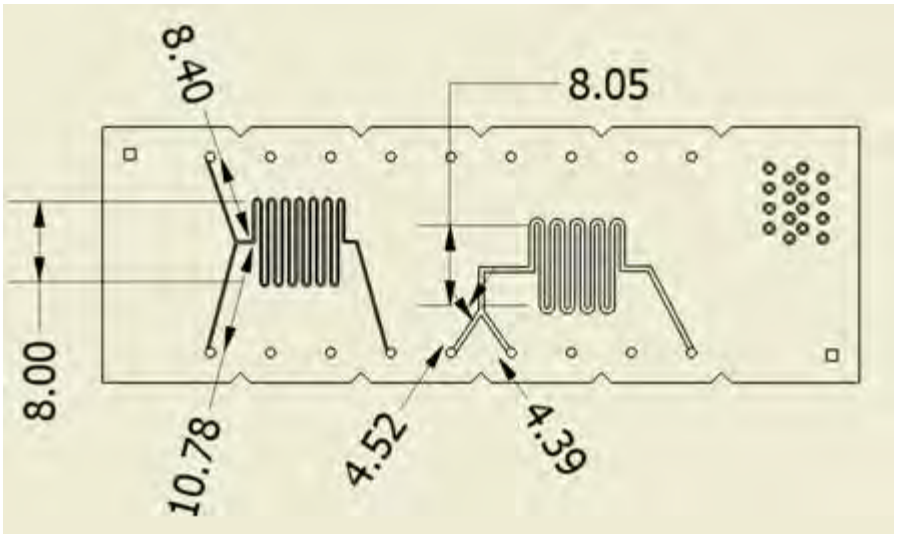

Figure 4.8 Microfluidic reactor which fits into the region for fluidic layout of the interconnect chip (Figure 4.7)

Chapter 5 Nanocluster formation

The classical studies on the formation of nanoparticles have proposed that the process consists of three stages, nucleation, growth and possible agglomeration or aggregation.[42] The two most widely cited models are the: classical model proposed by La Mer[43] and the Finke and Watzky model.[44] The earliest is the La Mer model.[43] La Mer used classical nucleation theory (CNT)[45] to describe the formation of sulfur monodispersed colloids from the decomposition of sodium thiosulfate in hydrochloric acid. The model presented in Figure 5.1, shows the concentration of sulfur nuclei vs. time and can be described as follow: the concentration of zerovalent sulfur atoms slowly increases (Stage I) until a critical level of supersaturation is reached. At this level, nucleation starts at a high rate (Stage II) then quickly drops off as the burst of nucleation immediately lowers the number of sulfur atoms in solution below the critical supersaturation level. Nucleation mostly stops at this time and slow diffusional growth begins (Stage III). Thus a complete separation of nucleation and growth is achieved. The growth phase might be followed by agglomeration or Ostwald ripening.

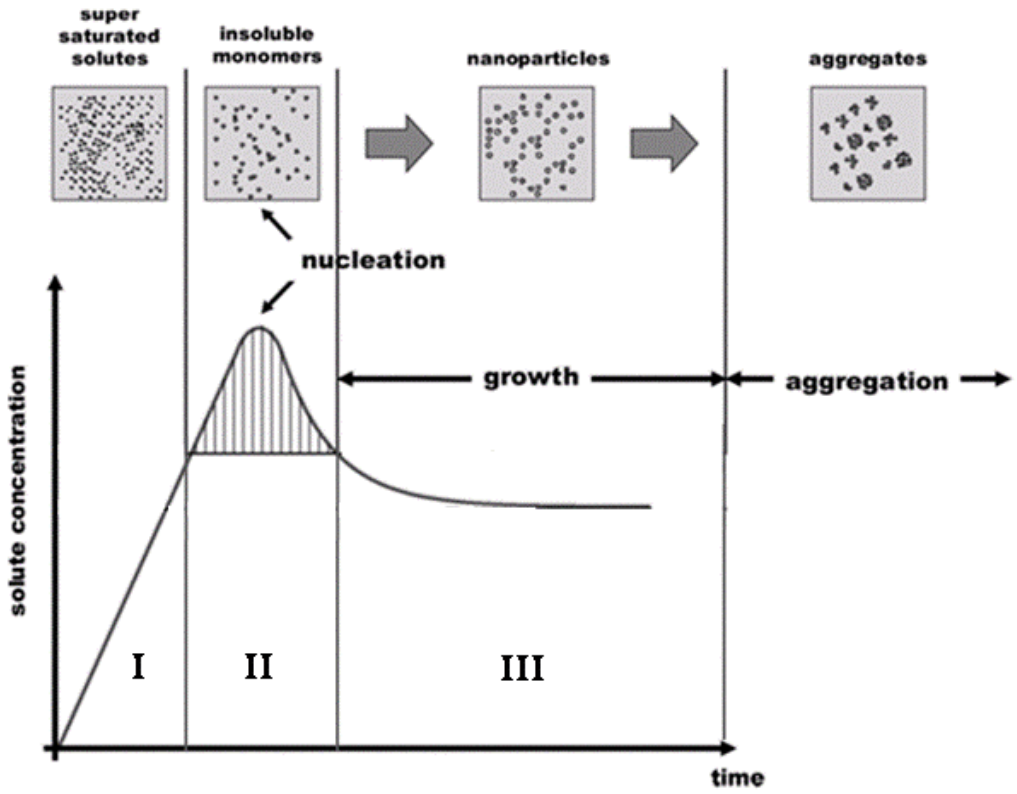

Figure 5.1 Scheme of nucleation and growth proposed by La Mer.[43a]

The La Mer model also can be described as:

$$n(S) \Leftrightarrow (S)_n,$$

where *S* is a sulfur atom.

The other model was proposed by Watzky and Finke.[44] They investigated a mechanism for the reduction of Ir salt with H_2 as a reducing agent via the measurements of the loss of hydrogen pressure. The proposed model consists of slow, continuous (not burst) nucleation followed by fast, autocatalytic (not diffusion-controlled) surface growth. The scheme of the model is:

$$A \xrightarrow{k_1} B \quad \text{(I)}$$

$$A + B \xrightarrow{k_2} B_2 \quad \text{(II)}$$

A represents the nanocluster precursor complex and *B* represents the growing surface of the Ir^0_n nanocluster:

$$Ir^I \rightarrow Ir^0$$

$$Ir^I + Ir^0 \rightarrow Ir^0_2$$

Ir^I are initial ions of the precursor complex. Once the critical nucleus, Ir^0 is formed it is able to catalytically influence the direct reduction of Ir^I upon addition to the surface of existing nanocluster Ir^0_n. The separation of nucleation and growth phases, necessary for narrow size distributions, is achieved in this system, by higher rates of growth compared to nucleation. The growth of existing nuclei dominates over the formation of new nuclei, because the reduction process in the catalyzed step II is kinetically much faster than that in the uncatalyzed step I. The kinetic data of this reaction and the fit based on the equations I and II are shown in Figure 5.2.

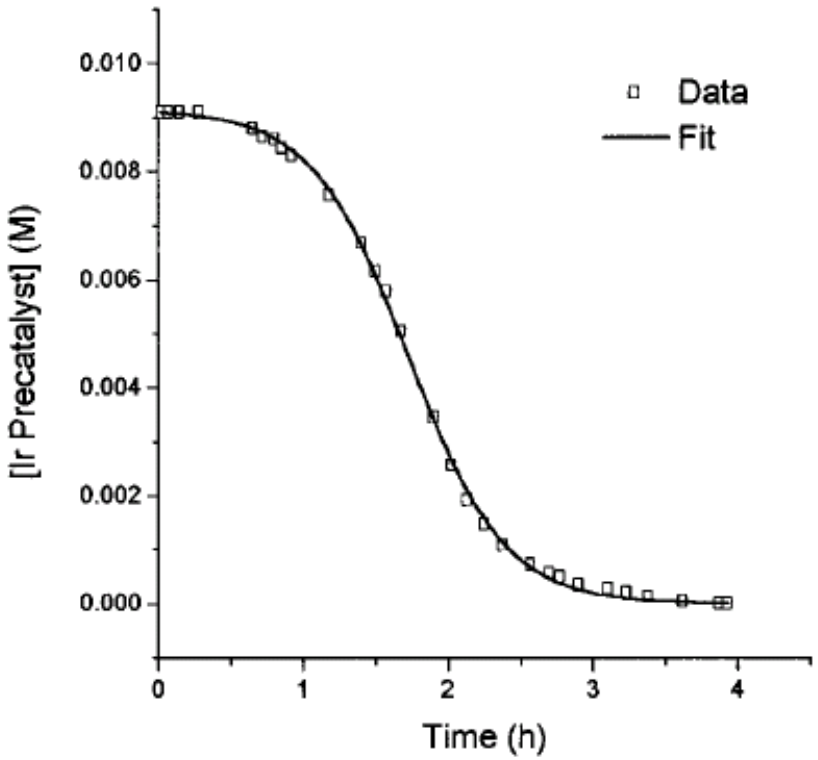

Figure 5.2 Plot of the loss of Ir precatalyst (A) versus time due to the reduction of A by H_2.[46]

In the Watzky and Finke mode of slow nucleation and autocatalytic growth, the induction period for the formation of critical nuclei was observed. The reaction is "dormant" for 1 h but then comes to completion in an additional 3 h, a total of 4 h. An upper limit on the average critical nucleus size after the induction period was estimated as $\leq Ir^{0}_{\sim 15}$.[47]

In fact, there was one more study in between these two. Shortly after the La Mer mechanism, in 1951, Turkevich *et al.* introduced the "organizer" theory of nucleation.[48] In their study, they reduced chloroauric acid in the presence of citrate, $C_6H_5O_7^{3-}$, as a stabilizer. They measured nucleation rates using the newly developed electron microscopy technique. They also observed an "induction" period before fast increase in the number of nuclei and finally a decrease of the nucleation rate (Figure 5.3).

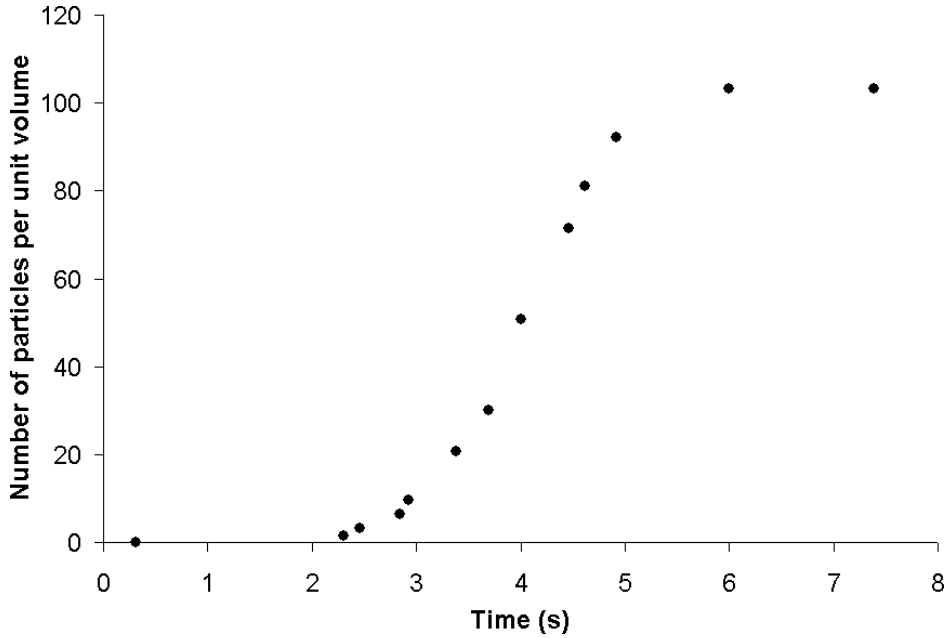

Figure 5.3 Particles formation rate observed by Turkevich.[48]

The proposed "organizer" theory is as follow: in the reaction solution of "copolymers" of gold ions bond to citrate ions; the citrate ion becomes oxidized to acetonedicarboxylic acid upon reduction of the gold ion to Au^0. The citrate ion is called the "organizer".

Turkevich mechanistic understanding of nanocluster formation is similar to the one discussed above by Watzky and Finke. In both cases a more gradual nucleation process compare to La Mer's burst nucleation is envisioned. The citrate in one case and H_2 in other is a slow reductant. Moreover, recently, Finke *et al.* presented an excellent fit of the Turkevich data based on the autocatalytic mechanism ($A \rightarrow B$, $A+B \rightarrow B_2$).[49] That is why the Watzky and Finke autocatalytic mechanism with precise chemical equations and defined rate constants of the nucleation and growth steps are considered to be more general and consequently more often cited than former "organizer" theory. The nanoclusters studied by Turkevich are formed via an analogous autocatalytic mechanism.

However the phenomenological nucleation step A→B introduced by Watzky and Finke does not give any details how the $Ir^{0}_{\sim 15}$ nucleus is formed. Several hypotheses were put forward by the authors:

- Under H_2 reduction conditions, metal hydrides $[M_xH_y]^{+/-}$ are intermediate compounds and are a key to the nucleation process.
- Nucleation of neutral atoms M^0 after reduction of metal ions and removal of ligands.
- The nucleation of metal ions, with some of their associated ligands $[M_xL_y]^+$ followed by reduction of the cluster to the zerovalent metal cluster.
- Some combination of the previous hypotheses: the nucleus consist of M^0 atoms surrounded by $[M_xL_y]^+$ and/or $[M_xH_y]^{+/-}$.

With respect to the exact mechanism of nanoparticles formation, different scenarios have been proposed in the literature. There is an investigation of the formation of Cu clusters with a tetraalkylbromide protection shell via reduction of Cu^{II} state in which energy dispersive X-ray absorption spectroscopy was used.[50] Cu K-edge absorption spectra were recorded every 2 min. The presence of a long-lived monovalent intermediate compound was observed, in which the copper is arranged in a linear configuration with two interacting partners. But no Cu^0 atoms were observed. The proposed scheme of the reaction (Figure 5.4) is:

1. Addition of the reducing agent $Li[BEt_3H]$ initiates the first step- the reduction of Cu^{II} ions which are surrounded by two Cl^- and two Br^- ions in square planar coordination of the precursor complex to monovalent Cu^I in a linear 2-fold coordination (Figure 5.4 (a) to (b)).

2. These complexes agglomerate to form Cu clusters of higher nuclearity; the formation of "Cu-Cu bonds" goes along with the complete reduction of the Cu ions to zerovalent metal (Figure 5.4 (b) to (c)). Only the surface atoms of the colloidal particles can be assumed to be in a nonzero valence due to the interection with surfactants and bromide ions.

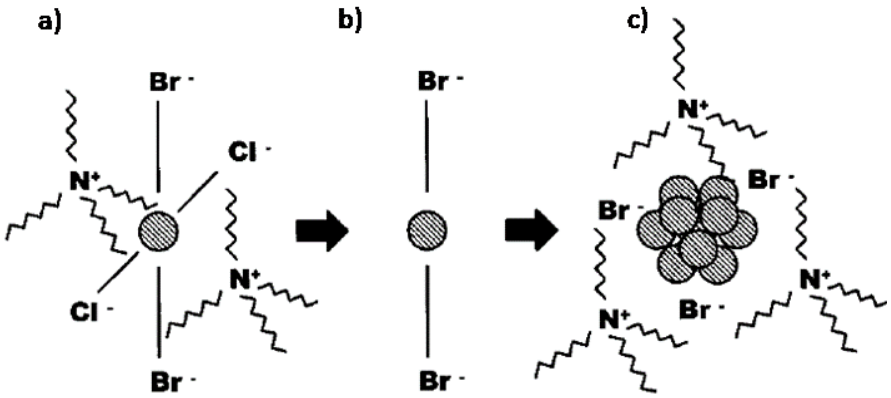

Figure 5.4 Proposed steps of the Cu colloid formation.[50]

Growth of the cluster via adsorption of intermediate metal ions and their reduction at the surface of the cluster seems to support the idea of an autocatalytic formation pathway. However, the appearance of intermediate complex is also in contrast to the one-step reduction mechanism of

the precursor complex (A+B→B_2) proposed by Watzky and Finke, emphasizing that a variety of possible reaction pathways might exists.

Another scheme of nanocluster formation was observed by Boennemann *et al.*[51] (Figure 5.5) in a study of the synthesis of colloidal Pt particles.

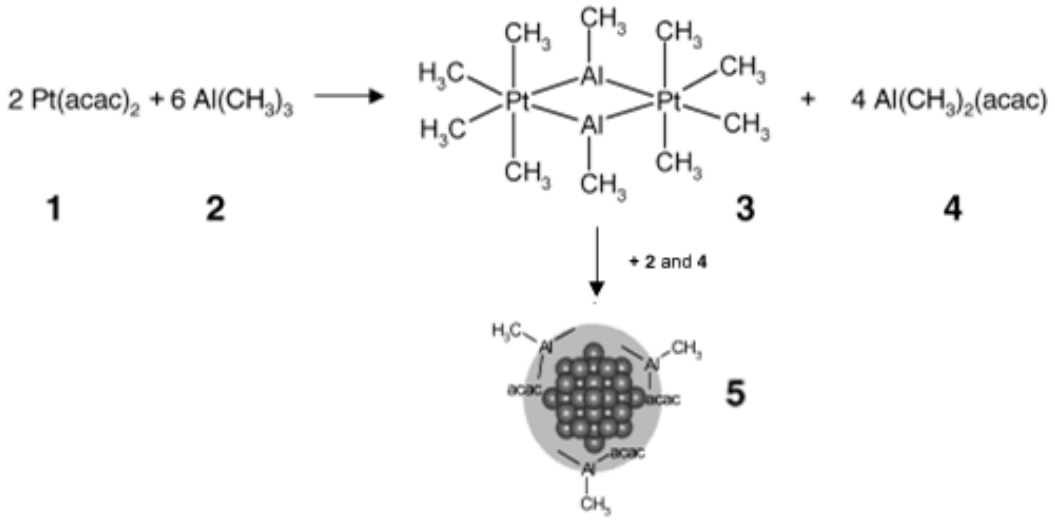

Figure 5.5 Schematic representation of the synthetic pathways of colloidal Pt particles.[51]

In this study a reaction between platinum acetylacetonate [$Pt(acac)_2$] and [$Al(CH_3)_3$] was monitored using a broad range of techniques, such as Nuclear Magnetic Resonance (NMR), anomalous small-angle X-ray scattering (ASAXS), *in situ* XAS, TEM and density functional theory (DFT) calculations. A metastable intermediate (Figure 5.4 (3)) consisting of two tetramethylplatinum species bridged by two methylaluminum species formed during the first 80 minutes of the reaction was proposed. No other metastable intermediate reaction products involving Pt were observed. Therefore complexes of type 3 are general precursors from which Pt nanoparticles such as 5 can be obtained.

Although the proposed intermediate complex was extensively characterized, the formation mechanism of the Pt nanoclusters themselves from this complex (i.e. from 3 to 5) was not investigated and assumed to be via *"reduction of the metal salt to give zerovalent metal atoms"* Pt^0 which *"can collide in solution to form an irreversible seed of stable metal nuclei"*.[51]

On the other hand, in the computational studies of Pt clusters formation from $[Pt^{II}Cl_4]^{2-}$ Ciacchi et al.[52] observed the formation of Pt^I –Pt^{II} and Pt^I –Pt^I dimers, where Pt^I is a linear $[PtCl_2]^-$ complex, which could then react with another Pt^{II} species to form Pt^I –Pt^{II} –Pt^I or Pt^I –Pt^{II} –Pt^{II} trimers. Based on their observations, the authors proposed that at least in the case of platinum, cluster formation occurs via bonding of metal ions before reduction to Pt^0, as opposed to full reduction to Pt^0 followed by nucleation of the Pt^0 atoms. In their calculations, the authors assumed a Pt^I as an intermediate.

The same reaction was studied by Henglein and coworkers.[53] An aqueous solution of $[Pt^{II}Cl_4]^{2-}$ is reduced by hydrogen; the rate of reduction is measured optically and conductometrically, and the colloidal nanoparticles, which are finally formed, are studied by high-resolution electron microscopy. Several mechanisms of the reduction are discussed:

1. Formation of Pt^0 atoms by reduction of H_2.
2. Formation of PtH as a first intermediate.
3. Formation of Pt^I by partial reduction.
4. Formation of $Pt^0{}_2$ by the reaction of two $PtCl_2(H_2O)_2$ molecules with H_2.

First, second and fourth reaction routes are excluded because they are high endoergic. The reason for this endoergicity is the high free enthalpy of formation of the species involved: 5.4 eV for the free Pt atom, 2.3 eV for PtH and 3.1 eV for $Pt^0{}_2$. The authors were left with the Pt^I mechanism; postulated it as the first intermediate of the true mechanism of Pt^0 nanocluster formation. Colloidal Pt^0 particles are then formed via coalescence of Pt^I.

Prior to the above experiments on the Pt particles formation Hengelein explained a growth mechanism of Ag clusters, which is also relevant to the current discussion.[54] The pulse radiolysis method was used to reduce Ag^+ to Ag^0 with citrate as a stabilizer agent. UV-visible spectroscopy and TEM was used to detect and follow the formation of small silver dimers and tetramers, such as $Ag_2{}^+$, $Ag_4{}^{2+}$, etc. As far as the only growth phase was considered, the exact structures were not of interest and small clusters were simply designate as Ag_x. The mechanism of Ag cluster formation is schematically depicted in Figure 5.6

Small Ag_x clusters are nuclei for the formation of larger particles via condensation reactions; they are designated as type-I nuclei. It was then assumed that at a critical size, the Ag_m cluster grows by addition of Ag^+ ions to the cluster surface. These critical nuclei were called type-II nuclei. Ag_n in that scheme is the final cluster. The mechanism described by Henglein closely resembles the Watzky and Finke mechanism, in which nucleation of metal atoms up to the critical size is followed by growth via surface reduction of additional metal ions.

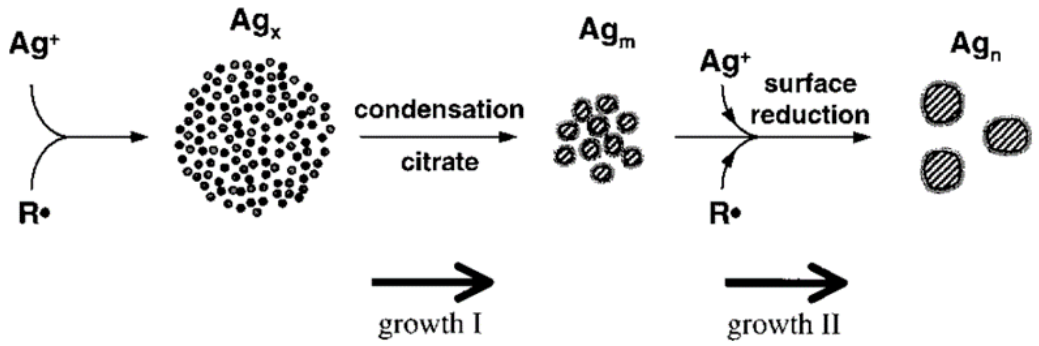

Figure 5.6 Scheme of Ag clusters growth.[54]
(R^* -reducing radicals)

Another interesting observation of the growth mechanism leading to the formation of monodispersed, spherical Au nanoparticles was recently presented also using TEM microscopy and UV-visible absorption spectroscopy.[55] The scheme is present in Figure 5.7

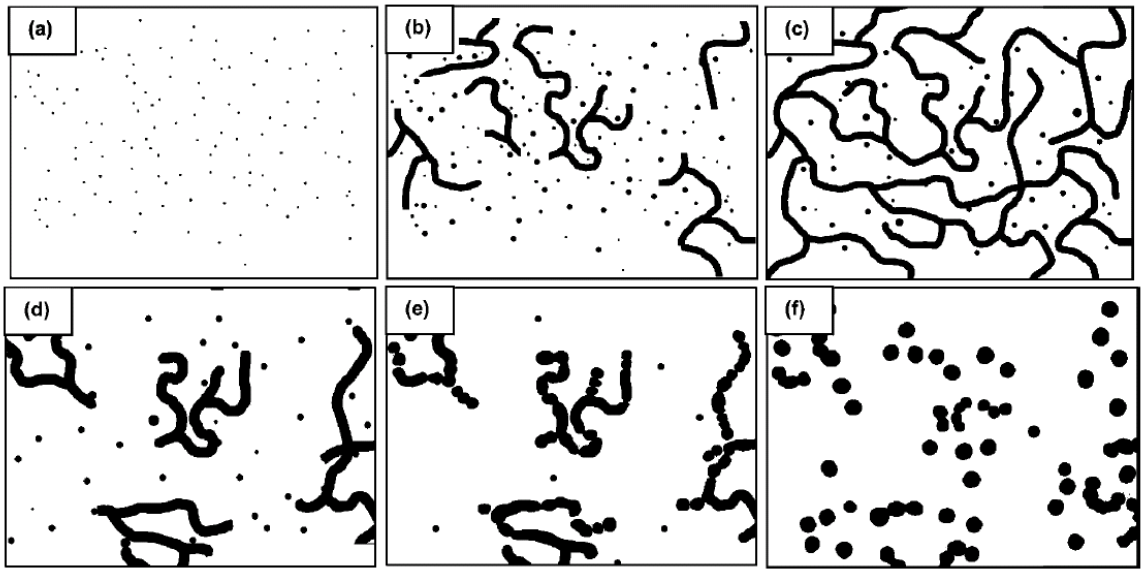

Figure 5.7 Scheme of Au nanoparticles growth.[55]

Gold ions reduced by citrate at elevated temperature collide to produce small gold nanoclusters smaller than 5 nm in diameter (a). The small nanoclusters self-assemble like a linear chain to form an extensive network of nanowires which have diameter of about 5 nm (b and c). As more Au atoms are formed, they adsorb onto the nanowires and the diameter of the nanowire increases, which is accompanied by fragmentation of the network to form small segments (d). Apparently, the increase in diameter destabilizes the nanowires, which fragment and cleave into sphere-like particles. Aging and Ostwald ripening then lead to the formation of well-defined spherical particles (e and f).

Also in this study there are no details on the nucleation stage. The reduction of $AuCl_4$ salt to Au^0 atoms was simply assumed by the authors without any experimental evidence. However the investigation of the growth mechanism revealed new mechanistic information that was not expected from either La Mer or Watzky and Finke nucleation growth models.

Evidently the supersaturated solution of free atoms proposed by the La Mer model was never directly detected in any study, but it has been demonstrated that a metal salt can be reduced to zerovalent atoms before nanocluster formation starts. For example in the UV- visible study of Pd nanoclusters formation Rothenberg et al.[56] followed the nanocluster and metal salt spectra with time. Because the spectra contain the physical information about all of the absorbing species in the mixture they were using the net analyte signal (NAS) approach[57] isolating the contribution of the various absorbing species and were able to measure the kinetics of salt reduction and nanocluster formation (Figure 5.8). From their data, they concluded that reduction of the metal salt to Pd^0, occurs before formation of clusters starts.

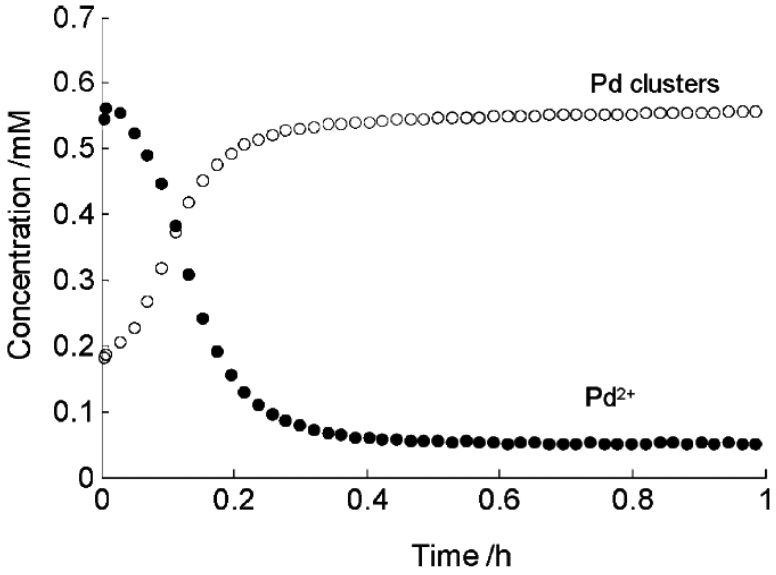

Figure 5.8 Concentration profiles showing the reduction of $PdCl_2$ and the formation of Pd clusters.[58]

The formation of cobalt oxide nanoclusters has been studied in detail by Tannenbaum *et al*.[59] A combination of infrared and X-ray photoelectron spectroscopies, TEM, and dynamic light scattering was used to identify the mechanism of metal nanocluster formation. The precursor complex used in their studies was cobalt octacarbonyl $Co_2(CO)_8$. The decomposition of $Co_2(CO)_8$ was assumed to take place via removal of CO ligands before clustering occurs. In their work, Tannenbaum et al. proposed three steps to nanocluster formation and stabilization in the presence of polymers such as poly(methylmethacrylate) (PMMA): (i) the formation of "metallomers" (small clusters- the critical nuclei Co^0_m) by heating a solution of $Co_2(CO)_8$ to 90^0C, (ii) the aggregation of metallomers to larger particles, and (iii) the adsorption of PMMA to the metal nanoparticles surface. First of all, it is highly questionable that the polymer does not interact with the metal throughout the nanocluster formation process, but instead waits in the background until a nucleus has formed and then grows to a cluster surface. Another not clear aspect in this study are the infrared data, which were used to address the question of the sequence of oxidation and clustering of Co atoms. The decrease of the CO band, corresponding to the decomposition of $Co_2(CO)_8$, began immediately, while the appearance of the Co-O band, corresponding to the formation of Co_2O_3 clusters, appeared after ~ 2 h time. This led the authors to conclude that decomposition of $Co_2(CO)_8$ occurs to form Co^0_m nuclei, which are then oxidized to yield Co_2O_3 clusters. However, from all above discussed examples reader understands that there are several possible scenarios of Co^0_m nanocluster formation. Unfortunately such a detailed characterization of the nucleation, growth phases and possible intermediates are missing in the work by Tannenbaum *et al*.

The ultimate aim of any mechanistic investigation of nanoparticle formation is to develop some general principles, which would make it possible to predict a precise reaction pathway leading to the formation of nanoparticles with desired characteristics and properties. It is hoped that the present work will assist in achieving this goal.

Chapter 6 Time-dependent XAS investigation of Co nanoparticles formation

6.1 "DCO synthesis"

The time-dependent Co K-edge XANES spectra of the samples taken from the synthesis with the DCO precursor are presented in Figure 6.1. Clear changes in the spectra are observed in the intensity of the pre-edge shoulder (A), position and the shape of the WL (B) and absorption structure above the edge (C). The observed changes in the spectra are belonging to different points of time of the synthesis will allow us to follow a path of nanoparticle formation.

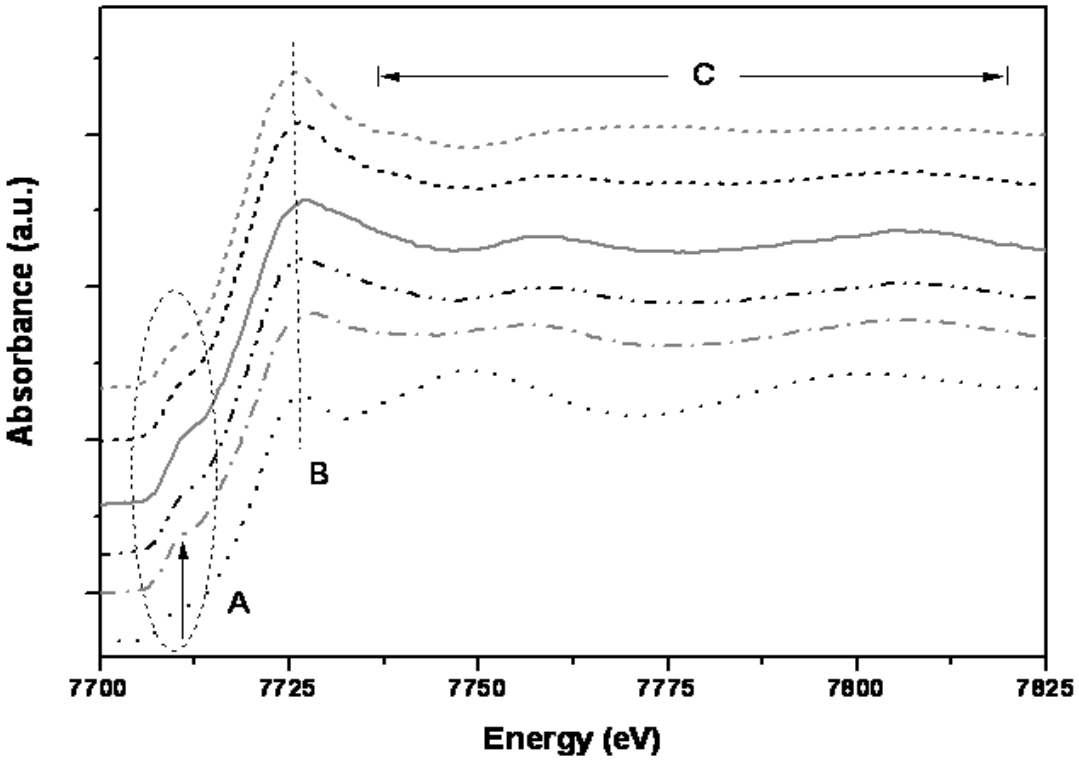

Figure 6.1 Co K-edge XANES spectra of the DCO synthesis from the bottom to the top: "DCO 2min" (dot black), "DCO 3h" (dash dot gray), "DCO 6h" (dash dot dot black), "DCO 9h" (solid gray), "DCO 12h" (short dash black), "DCO 18h" (short dash gray).

After two minutes, the products of synthesis still resemble the DCO starting complex more than a Co foil (Figure 6.2 (a)). The appearance of the WL as well as shape resonances (two maxima) at 7749 eV and at 7798 eV are very similar to those (7747 and 7798 eV) of the DCO complex. Also the intensity of the pre-edge shoulder, typical for transition metals due to transitions from 1*s* to 3*d* empty states, is reduced compared to the metallic cobalt foil and similar to the DCO complex. The difference of 1.5 eV in the WL position as well as reduced WL intensity compared to the DCO complex (inset Figure 6.2 (a)) are indicating changes in the electronic structure of cobalt atoms due to changes in the local environment, attributed to decarbonylation and/or decomposition of the DCO complex.

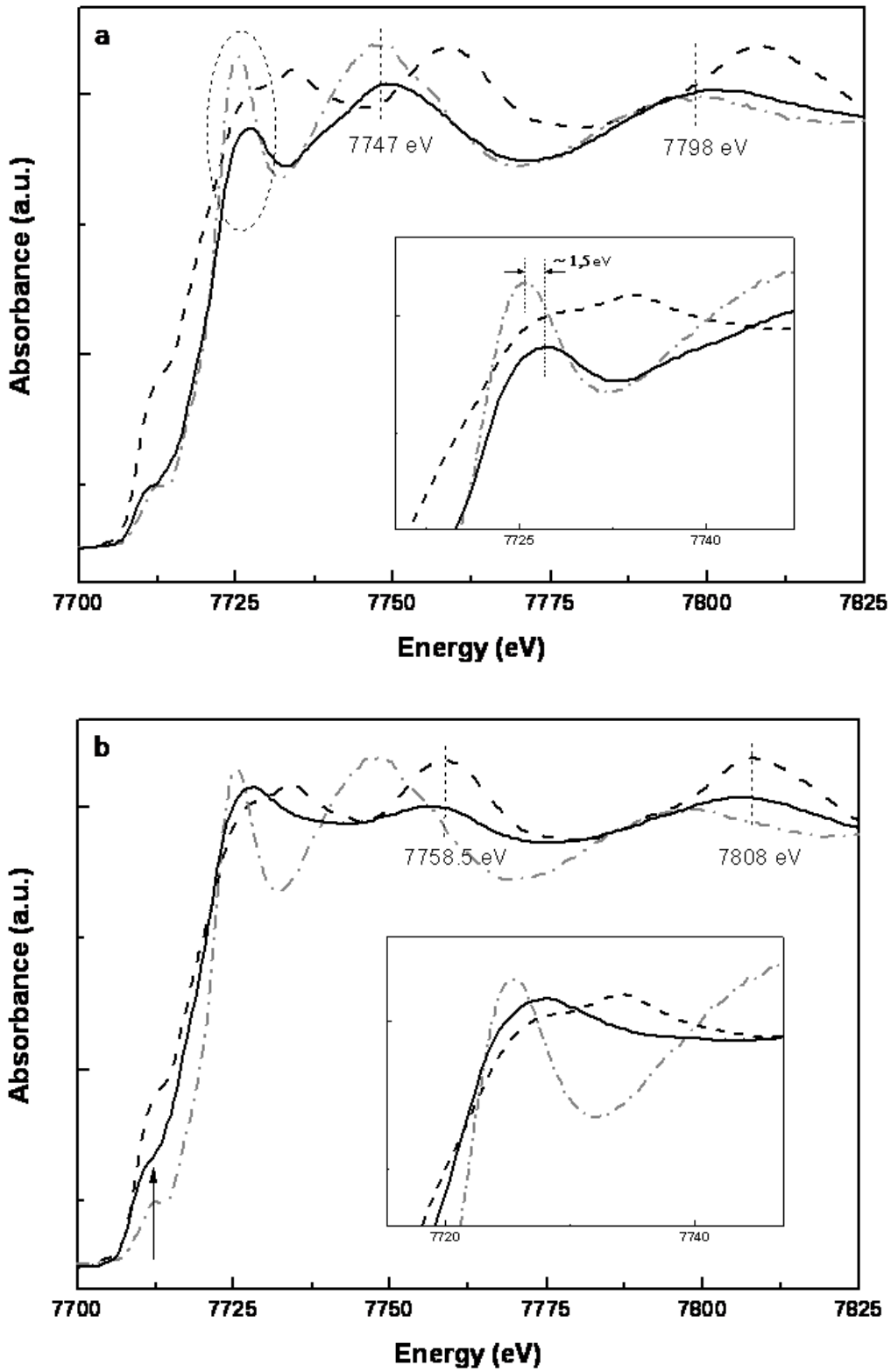

Figure 6.2 Co K-edge XANES spectra of "DCO 2 min" (a) and "DCO3h" (b) (solid black) in comparison with the Co foil (dash black) and the DCO complex (dash dot gray) reference spectra. Enlarged WL regions are shown in the insets.

According to the predecessors it is well known that the decomposition of the $Co_2(CO)_8$ is rather complex and kinetics of the CO evolution depend on the reaction temperature, the nature of the solvent and the surfactant, their respective ratios and even initial concentration of the cobalt carbonyl.[60, 61] Nevertheless an initial and rapid (in ~ 1 min.) evolution of CO corresponding to the formation of $Co_4(CO)_{12}$ was always recorded, which is most probably true and for the current reaction. From the time-dependent XANES analysis a cobalt organometallic complex(es) as a first reaction intermediate should be considered instead of highly reactive cobalt atoms proposed by the La Mer model. The following EXAFS analysis gives more details.

After 3 hours of the synthesis there are clear changes upon thermolysis as shown in Figure 6.1 (b). The most striking feature being a change of the WL appearance (inset Figure 6.1 (b)) as well as increased intensity of the pre–edge shoulder which results from the changes in the type of near neighbors. The spectral features of this sample can be interpreted if one imagines formation of small cobalt clusters (higher order then $Co_4(CO)_{12}$) via further partial decarbonylation. Moreover, the positions of the shape resonances (two maxima at 7757 and 7806 eV) are now more similar to the Co foil than to the DCO complex, indicating that the majority of the starting complex decomposed to cobalt metal phase.

The observed shift of the WL maximum to a lower energy compared to the Co foil might be correlated to the formation of a phase different from the Co foil hexagonal close-packed (hcp) phase.

Cobalt has long been known to have at least two crystal structures hexagonal close-packed (hcp) and face-centered cubic (fcc) above or below 420 °C, respectively.[62] The fcc and hcp phases of cobalt are close-packed structures and very similar to each others. They differ only in the stacking sequence of atomic planes in the 111 direction (Figure 6.3). The atoms of the second layer of the structure will preferentially sit in some of the hollows in the first layer. For the third layer of atoms there are two choices - these differ only in the relative positions of atoms in the 1st and 3rd layers. In the structure on the left the atoms of the 3rd layer sit directly above those in the 1st layer - this gives rise to the characteristic ..**ABABA**.. stacking sequence of the hcp structure. In the structure on the right the atoms of the 3rd layer are laterally offset from those in both the 1st and 2nd layers, and it is not until the 4th layer that the sequence begins to repeat. This is the ..**ABCABC**.. stacking sequence of the fcc structure. Because of their common origin, both of these structures have coordination number 12, i.e. each atom has 12 nearest neighbors.

The XANES spectra of these phases calculated using FEFF8 code in comparison with a Co foil spectrum are shown in Figure 6.4. From the comparison of the theoretical and experimental spectra of hcp cobalt it is clearly visible that good agreement is achieved with respect to all spectral features: the characteristic pre-edge structure and the double-peak white line where the second peak amplitude is higher than that of the first peak. Exception is the edge position, where maffin-tin potential are failed to reproduce the energy position of the absorption edge. The main differences between the spectra are observed in the WL region, (approx. 7725-7737 eV). Both the hcp and fcc structures have two well resolved peaks (around 7727 and 7734 eV); the difference between the fcc and hcp phase structure is the relative intensity of these two peaks.

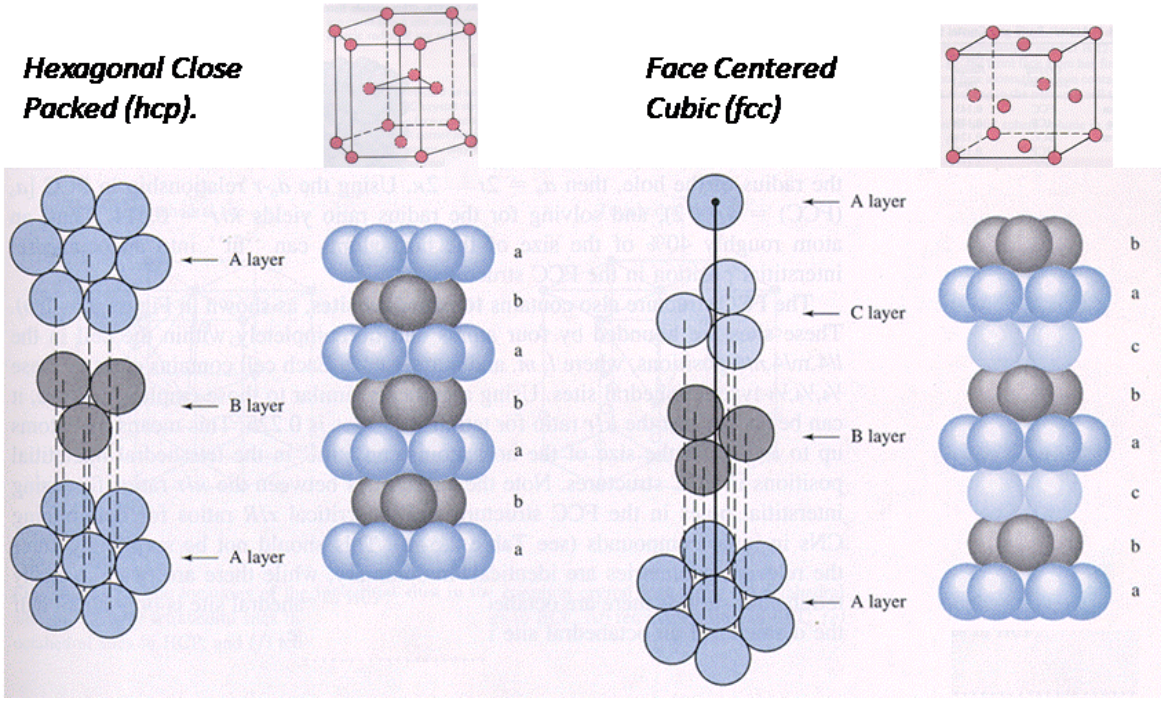

Figure 6.3 Plane stacking sequences in the *Hexagonal Close Packed* and *Face Centered Cubic* structures.

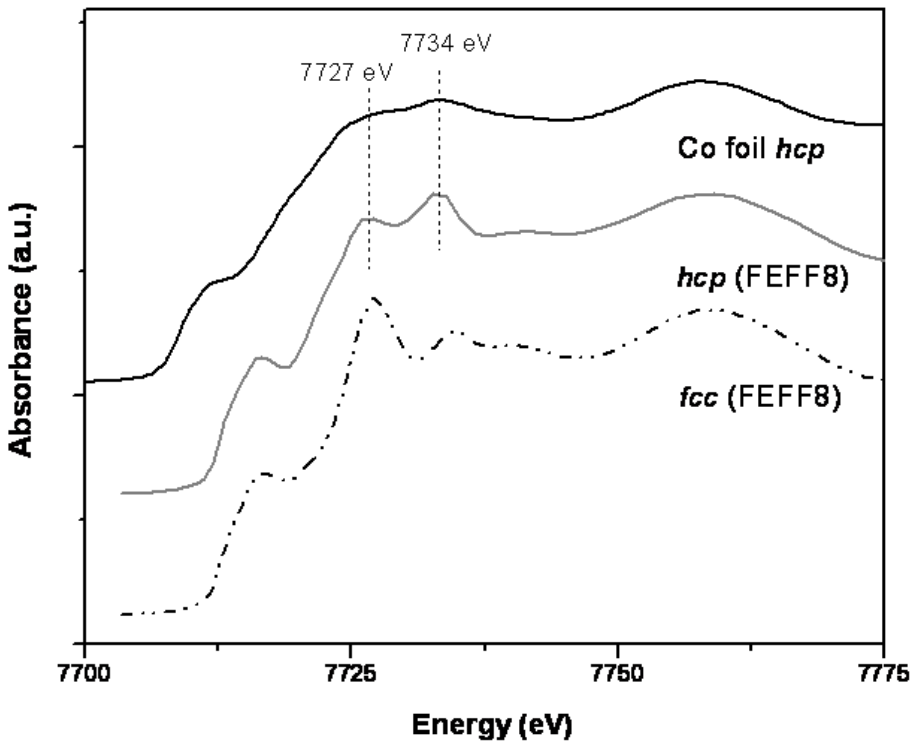

Figure 6.4 Co K-edge theoretical spectra of *hcp* and *fcc* phases calculated using FEFF8 code in comparison with Co foil experimental spectrum.

After 3 hours, the DCO spectrum shows the shape of the WL shows more resemble to the theoretical spectrum of fcc cobalt (Figure 6.5), with the maximum of intensity around 7727 eV, as opposed to 7734 eV in the hcp phase. However, the two peaks in the white line are not as clearly resolved as in the theoretical spectra. This is particularly true for the nanoparticles samples. One should bear in mind that the calculated spectrum correspond to a perfectly ordered system at 0 Kelvin and do not include any experimental broadening.

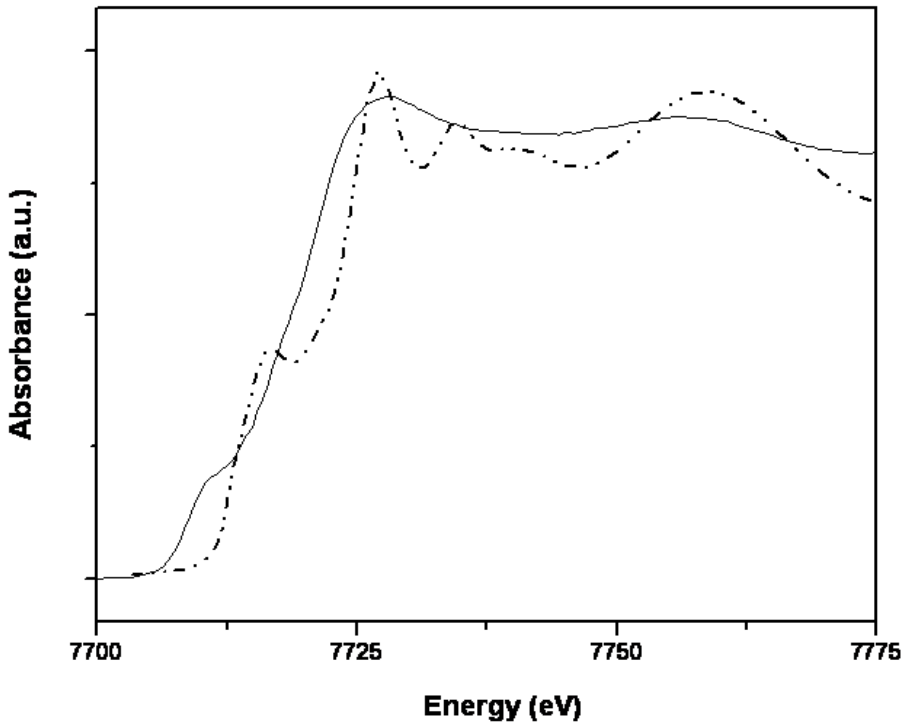

Figure 6.5 Co K- edge XANES spectra of the "DCO 3h" sample (solid black) and theoretical *fcc* phase (dash dot dot black).

The result that the initially formed cobalt clusters might posses at room temperature an unstable fcc structure compare to the stable bulk hcp phase is perhaps not surprising. Firstly because for small particles the fcc structure appears to be preferred even below room temperature[63] and secondly that the first nucleus itself is a metastable state. Following the Ostwald "step rule": "the crystal phase that is nucleated needs not be the one that is thermodynamically the most stable, but the one that is the closest in free energy to the fluid phase"[64] The thermodynamic approach to phase selection and possible changes will be given bellow.

To get more information about how these initial cobalt clusters are formed from the $Co_2(CO)_8$ or $Co_4(CO)_{12}$ complexes, three more samples were analyzed in between 2 minutes and 3 hours of the synthesis that is "DCO 10 min", "DCO 30 min" and "DCO 1h". The XANES spectra of those samples and the "DCO 2 min" sample are present in Figure 6.6. As can be seen the spectra do not differ significantly. The overall position of the absorption edge and the WL does not change. Also the pre-edge intensity remains more or less constant that is clearly seen in the first derivatives shown in the inset Figure 6.6. The change in the height of the WL maximum corresponding to the $1s \rightarrow 4p$ transition indicates changes in the electronic structure of cobalt

atoms. Due to the size of the 4*p* orbital, it overlaps with *p* orbital of the CO ligand, either through σ or π-bonding. Consequently, this transition is sensitive to the changes in the local CO environment of the Co atoms and the different stages of the decarbonylation are observed, which should be more apparent in the EXAFS analysis (vide infra).

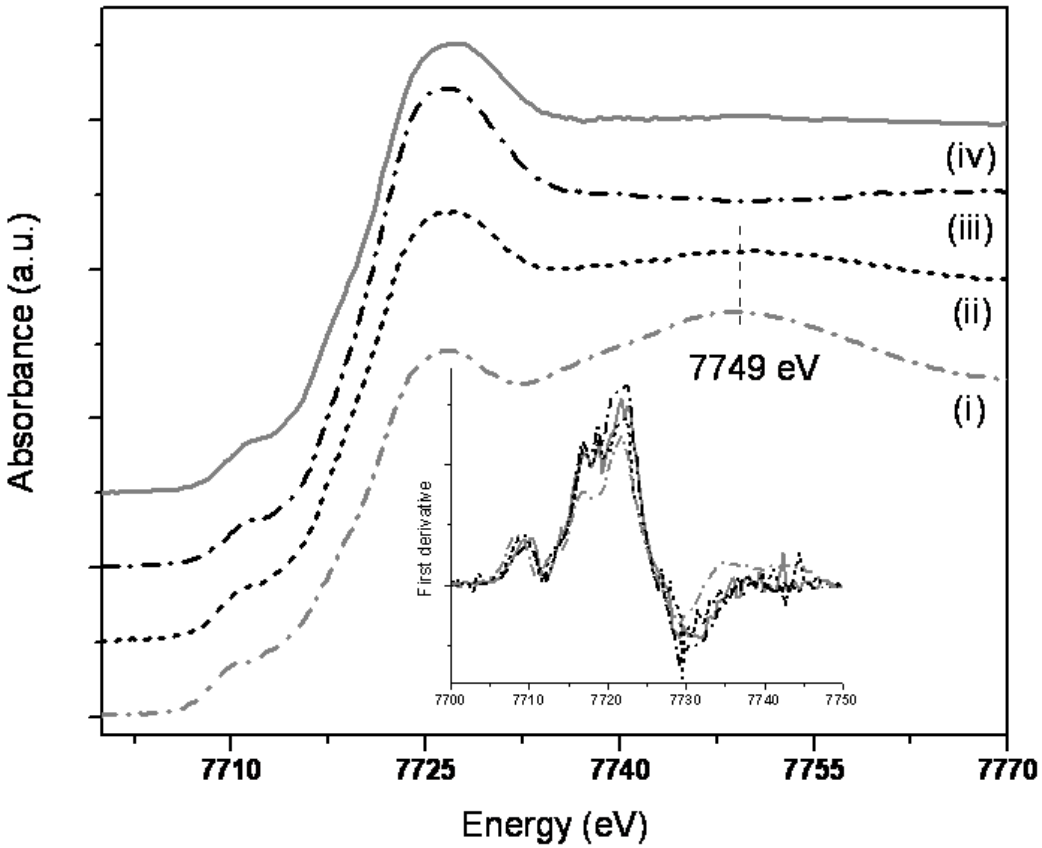

Figure 6.6 Co K-edge XANES spectra i) "DCO 2min", ii) "DCO 10min", iii) "DCO 30min", iv) "DCO 1h". First derivatives are shown in the inset.

It is tempting to suggest that the "S-shaped" variation in the height of the WL (decreasing, increasing, and again decreasing) describes the varying rate of the decarbonylation. After an initial rapid (~1-2 min.) evolution of CO corresponding to the formation of $Co_4(CO)_{12}$ the decomposition rate slows down and a $Co_4(CO)_{12}$ intermediate complex might be present in the reaction medium up to 10 min. An indication of that is the similarity between the "DCO 2min" and the "DCO 10 min" spectra. The "DCO 10 min" spectrum also has the shape resonance at 7749 eV as the "DCO 2 min" spectrum. A significant rearrangement around the absorbing atom is observed only at ~30 minutes of the reaction, because for the "DCO 30 min" sample that maximum at 7749 eV has disappeared. From here the CO evolution is accelerated again up to the "DCO 1h" sample, and we observe the decreasing of the WL intensity, but then the decomposition rate slows down as the initial cobalt clusters are formed only after ~ 3 hours of the synthesis.

The nature of the different carbonyl intermediates present in the reaction is difficult to determine. Different cobalt carbonyl structures with different number of CO groups, different configurations of bonding in single and multiple cobalt clusters, which possibly might be present during the

decomposition are illustrated in Figure 6.7. The most frequently encountered modes of CO bonding in carbonyls are terminal and bridging between two or three metals. For example in the $Co(CO)_6$ all CO molecules are terminally bonded, whereas when the metal molecule has metal-metal bonds there exists the possibility for the binuclear carbonyl bridge bonding which is shown for the $Co_4(CO)_{12}$ and for one of the $Co_2(CO)_8$ isomer. However the binuclear bridge binding is not mandatory, e.g., another $Co_2(CO)_8$ isomer has only terminally bonded CO ligands.

Through the inspection of the structural parameters of several carbonyls some generalizations can be made.[65] The terminal metal-carbon (M-C) distances are lying between 1.8÷1.9 Å and the bridged between 1.9÷2.0 Å. The M-M bond distances in the multimetal complexes are 2 to 4% larger than the metallic spacing (exception is the $Co_4(CO)_{12}$ where it is 2.48 Å and close to the bulk cobalt value of 2.49 Å).

Examination of these changes in the Fourier transforms of the corresponding Co K-edge EXAFS data (shown in Figure 6.8) was done by a detailed analysis in terms of structural models of the precursor complex and bulk cobalt.

Figure 6.9 and Figure 6.10 show the k^3weighted $\chi(k)$ Co K-edge EXAFS and corresponding back Fourier transformed functions as well as the fitting results for the “DCO 2 min”, “DCO 10 min”, “DCO 30 min”, “DCO 1h”, “DCO 3h” and the DCO starting complex. *k*-range of Fourier transform and *R*-range of Fourier fitting were 1.8-10 $Å^{-1}$ and 1.5-3.2 Å, respectively. Structural parameters of the fitting analysis are shown in Table 4 and Table 5.

The analysis proved to be relatively intractable problem. Although it was possible to analyze the Co K-edge EXAFS data by considering a Co-C shell at approximately 1.7-1.9 Å, Co-Co shell in the range of 2.4 to 2.8 Å and Co-C shell at 2.9-3 Å, both the bond lengths and coordination numbers (CN) obtained for the reference DCO starting complex were found to differ considerably from the crystallographic data (Table 4).[65] This might be explained by high reactivity as well as air sensitivity of the DCO complex. The sample for this reference was prepared by dissolving the small amount of the DCO complex in toluene, and probably already some reactions took place and different carbonyl groups were formed in the sample solution. Therefore the obtained bond length and coordination numbers are averaged. Nevertheless the $Co_2(CO)_8$ was the only carbonyl complex that showed a resolvable splitting (0.5 Å) due to the bridge bonded CO groups (Figure 6.8).

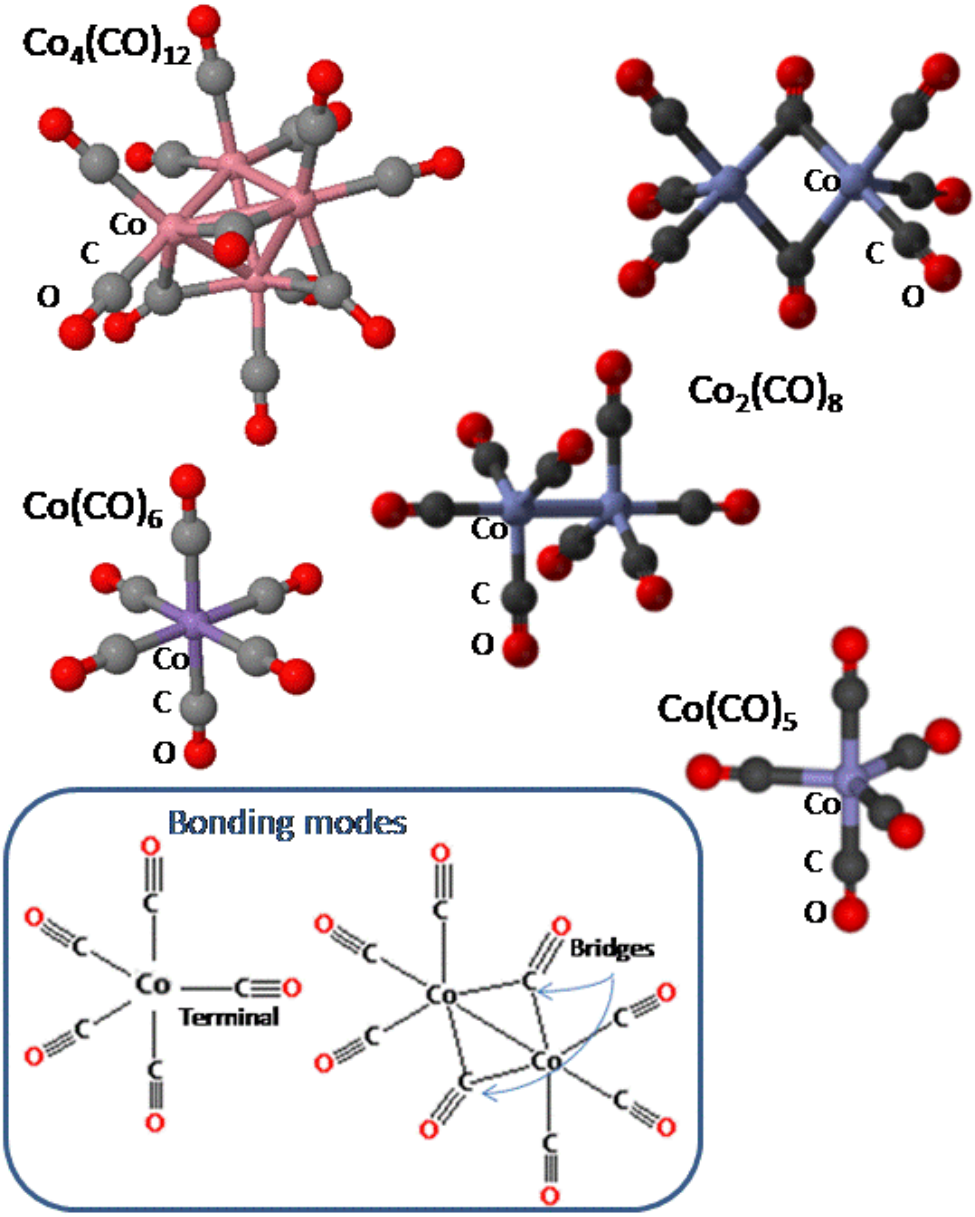

Figure 6.7 Molecular crystal structure diagrams of various cobalt carbonyls and two most important bonding modes.

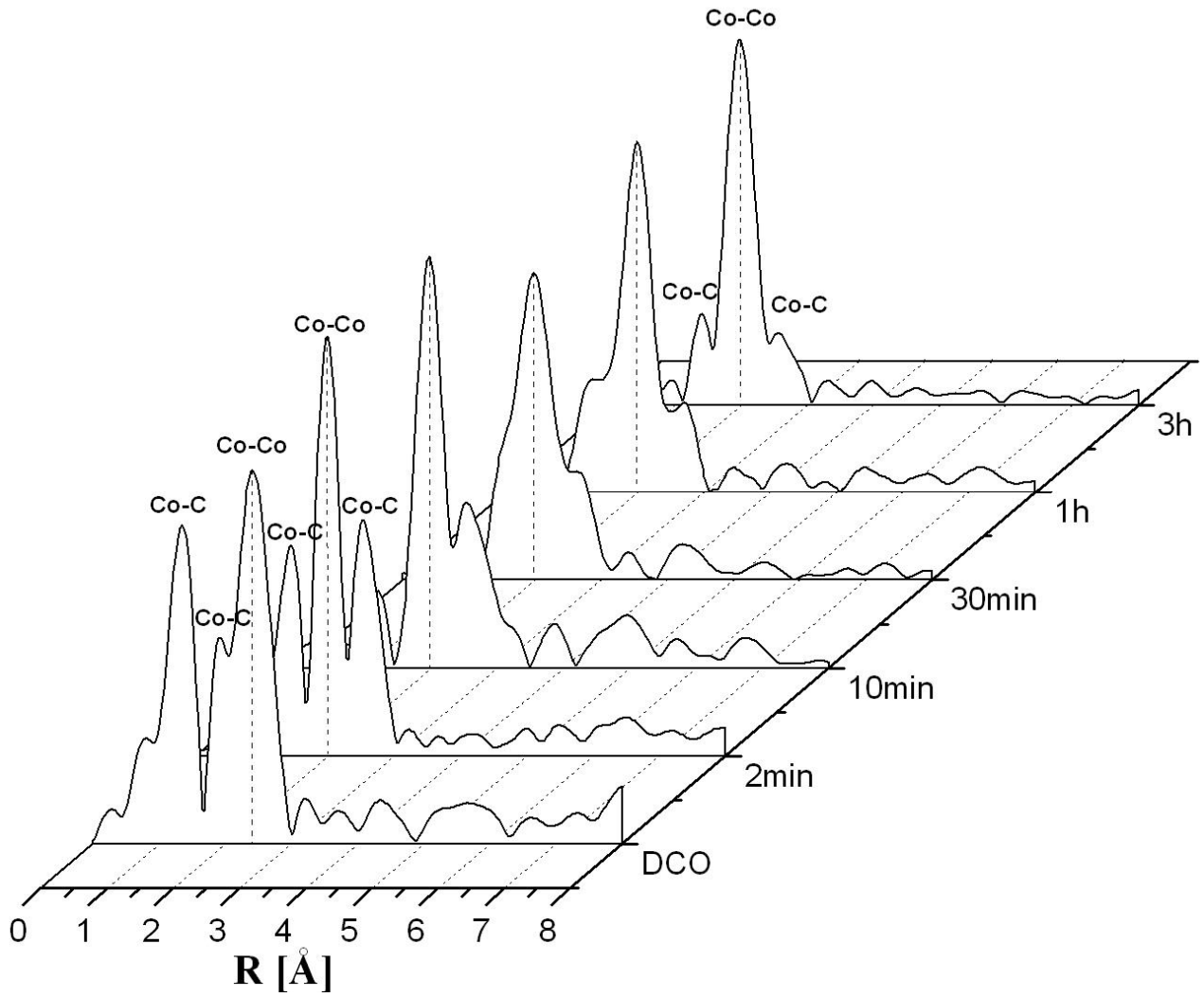

Figure 6.8 FT EXAFS spectra of the DCO starting complex, "DCO 2 min", "DCO 10 min", "DCO 30 min", "DCO 1h" and "DCO 3h" samples, k^3weighted (not phase corrected).

Table 4 EXAFS fitting parameters for the DCO complex. S_0^2= 0.825, *k*-range 1.8-10 Å^{-1}, *R*- range 1.5-3.2 Å. Crystallographic values are in brackets.

Paths	ΔE_0 [eV]	*R* [Å]	*N*	σ^2[Å^2]	*R factor of fit*
Co-C	12.0±0.5	1.83±0.10	4.1±2.0	0.006±0.005	0.04
		(1.80)	*(3)*		
Co-C		2.53±0.03	4.7±1.3		
		(1.92)	*(2)*		
Co-Co		2.74±0.05	3.2±0.5		
		(2.52)	*(1)*		

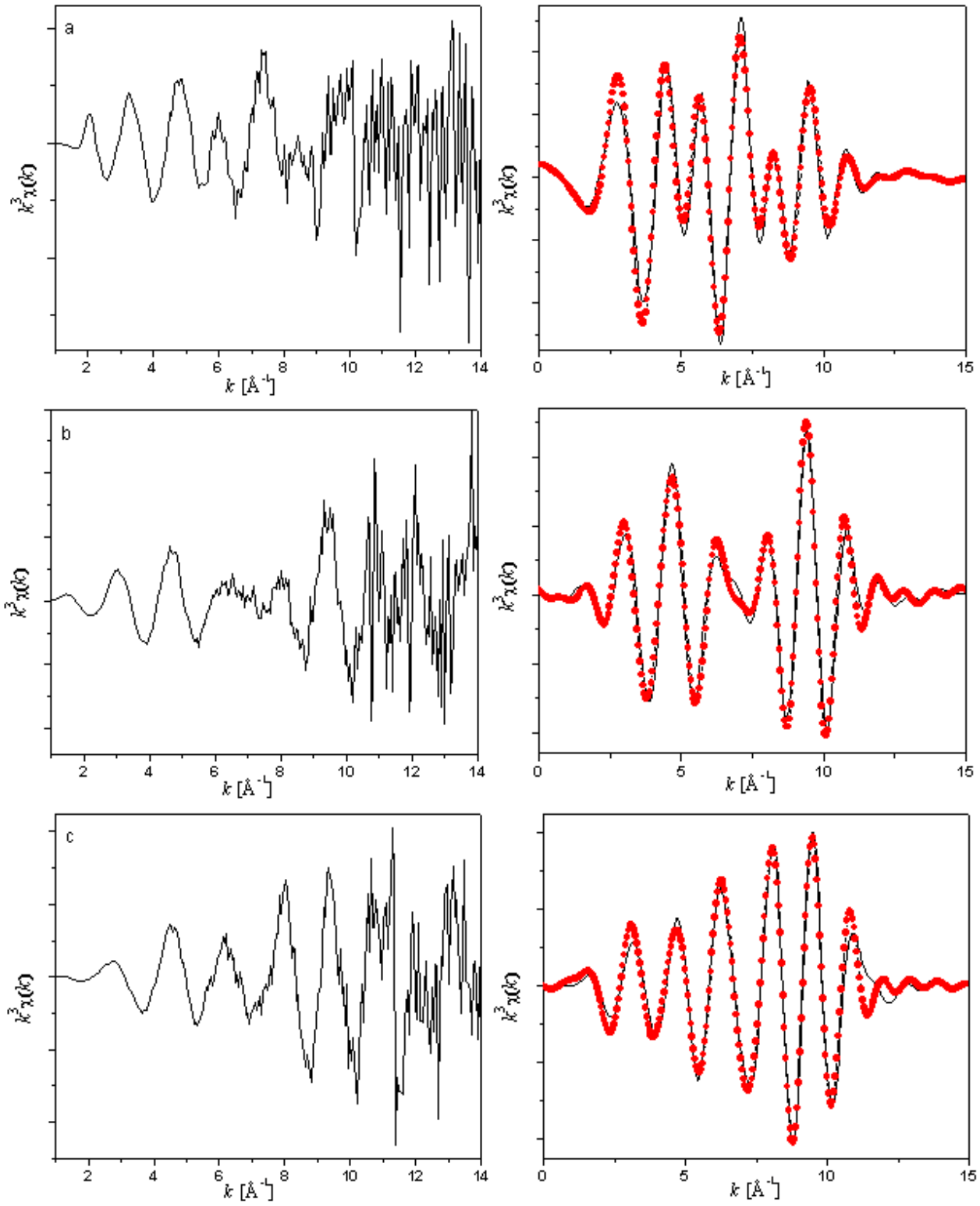

Figure 6.9 k^3weighted $\chi(k)$ Co K-edge EXAFS (left panel) and corresponding back transformed data and fit (right panel) of a) DCO, b) "DCO 2min", c) "DCO 10 min". Data are depicted as solid lines and the fits as solid circles.

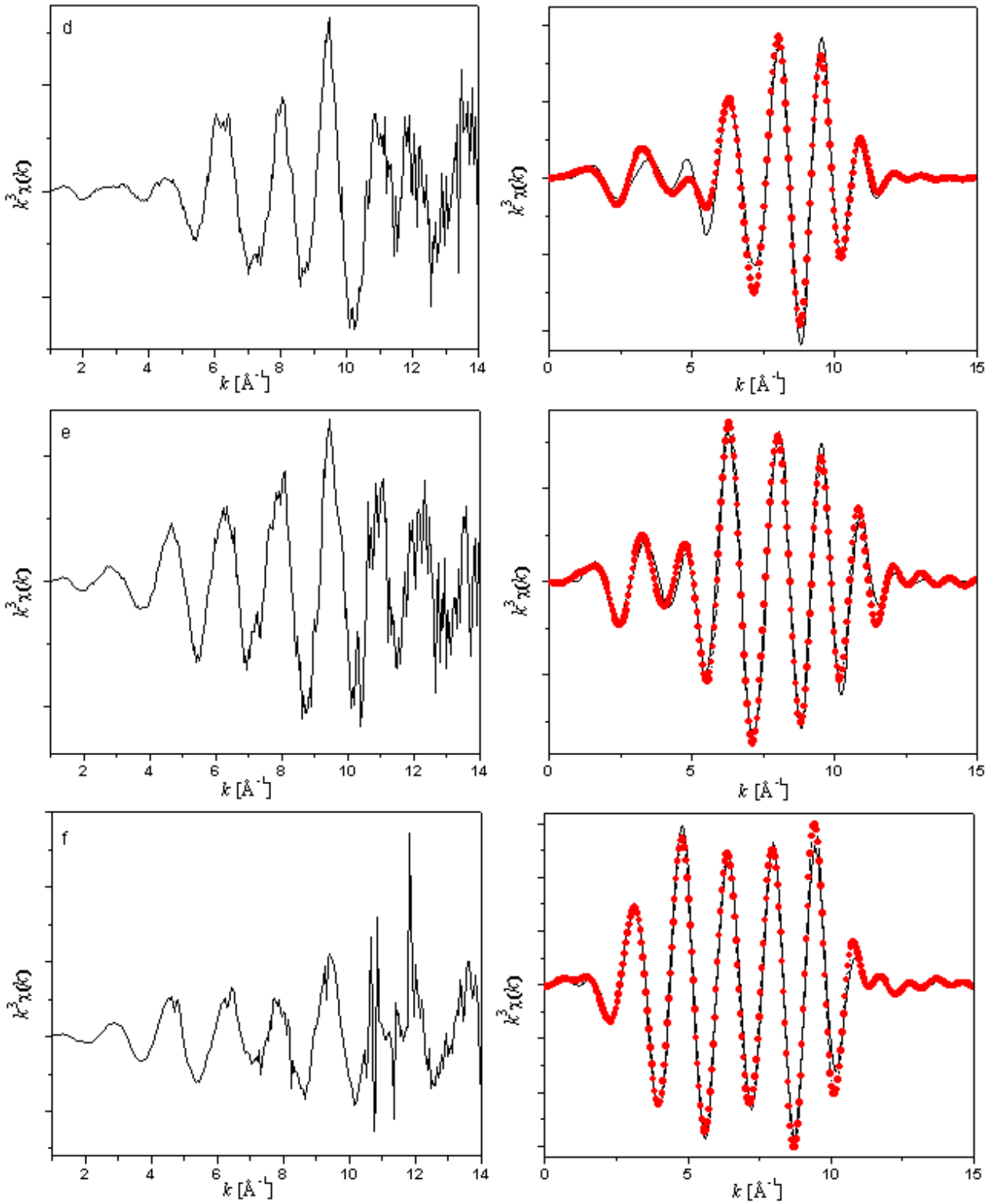

Figure 6.10 k^3weighted $\chi(k)$ Co K-edge EXAFS (left panel) and corresponding back transformed data and fit (right panel) of d) "DCO 30 min", e) "DCO 1h", f) "DCO 3h". Data are depicted as solid lines and the fits as solid circles.

In the first step of the decarbonylation that is after 2 min. of the synthesis the Co-Co peak appeared at distance of 2.48 Å which is decreased compared to 2.74 Å of the starting complex. Besides, two Co-C peaks at 1.77 Å and 3.07 Å are observed. The decreased Co-Co distance, is comparable to the bulk value (2.49 Å) and suggests $Co_4(CO)_{12}$ formation as a first reaction intermediate (vide supra).

Table 5 EXAFS fitting parameters for the "DCO 2 min", "DCO 10 min", "DCO 30 min", "DCO 1h" and "DCO 3h" samples. S_0^2= 0.825, k-range 1.8-10 Å^{-1}, *R*- range 1.5-3.2 Å.

	"DCO 2 min"	"DCO 10 min"	"DCO 30 min"	"DCO 1 hour"	"DCO 3 hours"
ΔE_0, [eV]	0.2±0.5	-0.5±1.0	-1.2±0.7	0.2±1.0	1.2±0.01
R_{Co-C}, [Å]	1.77±0.01	1.99±0.02	2.01±0.01	1.97±0.01	2.18±0.01
N_{Co-C}	1.1±0.2	0.9±0.2	1.5±0.2	1.2±0.3	1.0±0.2
R_{Co-Co}, [Å]	2.48±0.01	2.47±0.01	2.45±0.004	2.46±0.01	2.46±0.04
N_{Co-Co}	1.7±0.2	1.5±0.1	1.1±0.1	1.3±0.3	1.7±0.1
R_{Co-C}, [Å]	3.07±0.01	3.05±0.01	3.05±0.02	3.02±0.02	2.96±0.09
N_{Co-C}	12.3±1.2	10.4±2.6	3.4±0.9	3.4±0.5	2.1±0.6
σ^2_{Co},[Å^2]	0.004±0.002	0.003±0.0004	0.003±0.0004	0.003±0.002	0.003±0.0005
σ^2_{C},[Å^2]	0.004±0.002	0.004±0.002	0.003±0.0004	0.003±0.002	0.004±0.002
R factor of fit	0.03	0.04	0.04	0.04	0.009

Also for all other reaction intermediates Co-Co peak appears at distances very close to the bulk and not to the DCO complex value. Therefore FT EXAFS data of the reaction intermediates suggest rapid decomposition of the DCO starting complex (within 2 min of the reaction). The shorter metal bond distances reflect the nucleation of metal species with a structure that is more consistent with the final close-packed nanoparticles than that of the precursor.

After 2 minutes and within the next ~ 3 hours of the synthesis the coordination numbers (CN) of the Co-Co bond and Co-C nearest neighbor bond (between 1.77 and 2.18 Å) show a non-trivial behavior, depicted in Figure 6.11. Apparently, the decarbonylation is not a linear process. In fact, this diagram is also supported and coincides well with the non-trivial variation of the respective Co-C bond distance (highlighted in Table 5).

The bonding of CO to a metal consists of two steps. The first step is a two electron donation of the lone pair on carbon (coordination exclusively through the oxygen is extremely rare) into a vacant metal *d*-orbital. This electron donation makes the metal more electron rich, and in order to compensate for this increased electron density, a filled metal *d*-orbital may interact with the empty π^* orbital on the carbonyl ligand to relieve itself of the added electron density. This second component is called π-backdonation. This is shown schematically as well as through a simple molecular orbital picture in Figure 6.12.

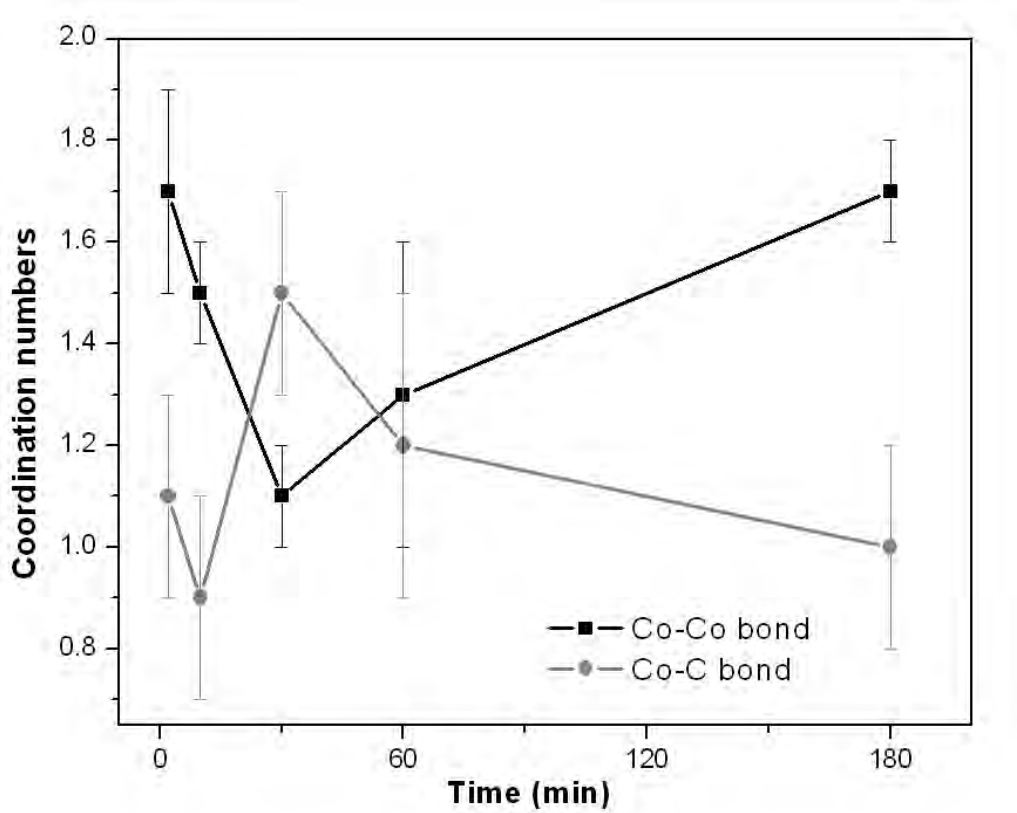

Figure 6.11 Variation of Co-Co and Co-C nearest neighbor bond CN as functions of synthesis time.

The observed increase in the Co-C nearest bond distance from 1.77 to 2.01 Å may be attributed to the reduction of the $d \rightarrow \pi^*$ back donation[66] because CN of Co atoms is decreasing and CO increasing during that period (from 2 min to 30 min). Further decrease of the Co-C bond distance to 1.97 Å is corresponding to the extension of the $d \rightarrow \pi^*$ backdonation and again corroborates with increasing Co and decreasing CO CN (from 30 min to 1 hour of the synthesis). Finally at 3 hours of the synthesis the bond distance is increased up to 2.18 Å due to the decreased $d \rightarrow \pi^*$ back donation because of the increased Co-Co and decreased Co-C CN.

The coordination number of Co-C bond at ~3 Å distance is gradually decreasing along the synthesis (highlighted in Table 5) and clearly visible in Figure 6.8, where the Co-C peak amplitude is decreasing. This corroborates the loss of carbonyl groups along the cobalt cluster formation. Nevertheless the presence of the Co-C peaks in the FT of the "DCO 3h" sample suggests that the formed cobalt clusters are not "naked" but are bonded with CO ligands.

In the diagram of cobalt cluster formation (Figure 6.11) the time region between 20 and 50 minutes is "anomalous" and might be considered as a crucial point in the nucleation process. At that time (30 min. of the synthesis) the shortest Co-Co bond distance of 2.45 Å (Table 5) is observed, intuitively suggesting a nucleation of metal species. Also in the above XANES analysis the "DCO 30 min" was the first sample where significant rearrangements around the absorbing atom were denoted. If this is the case and the "DCO 30 min" can be considered as first stable nuclei then it is important to note its CN. The EXAFS results support the idea of the $Co_n(CO)_m$ critical nuclei with n=2 and m=5.

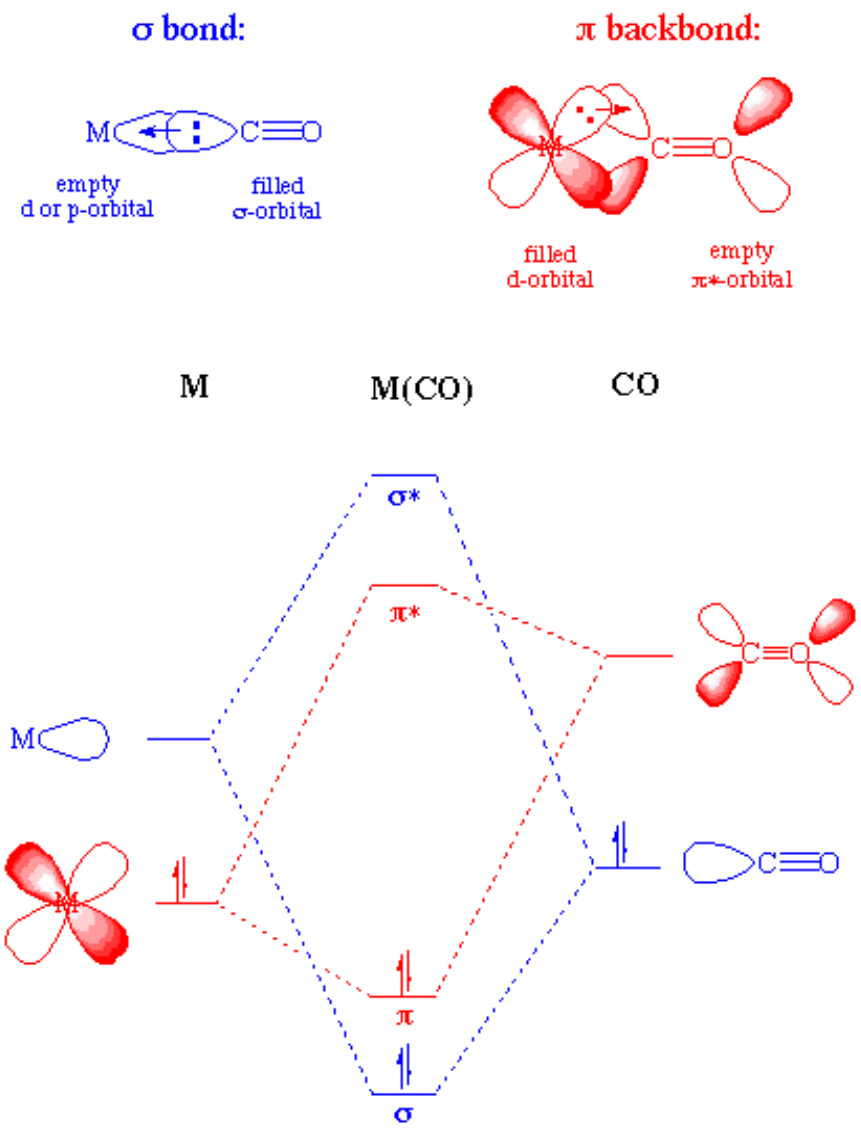

Figure 6.12 The diagram of metal CO bonding.

Insight into the growing phase was obtained by examining the Co K-edge X-ray absorption near-edge structure of the "DCO 6h", "DCO 9h", "DCO 12h" and "DCO 18h" samples in comparison with Co foil, CoO and $CoCO_3$ reference spectra (Figure 6.13).

The spectra of the "DCO 6h" and "DCO 9h" samples show an overall similarity. For both spectra a slightly more intense white line compared to the Co foil is observed, suggesting the presence of a fraction of the Co bound in the form like $Co_n(CO)_m$ surface complexes. The intensity of the pre-edge shoulder is very close to that of Co foil, especially for the "DCO 9h" sample. The energy positions of the shape resonances A and B (Figure 6.13) are identical to cobalt foil. These observations suggest the formation of an increasingly metallic state.

However, the next pair of spectra the "DCO 12h" and "DCO 18h" exhibits differences with the metallic cobalt foil spectrum. In contrast to the "DCO 9h" and "DCO 6h" the WL intensity is more increased and the pre-edge starts to decrease, suggesting the decrease of the metallic core.

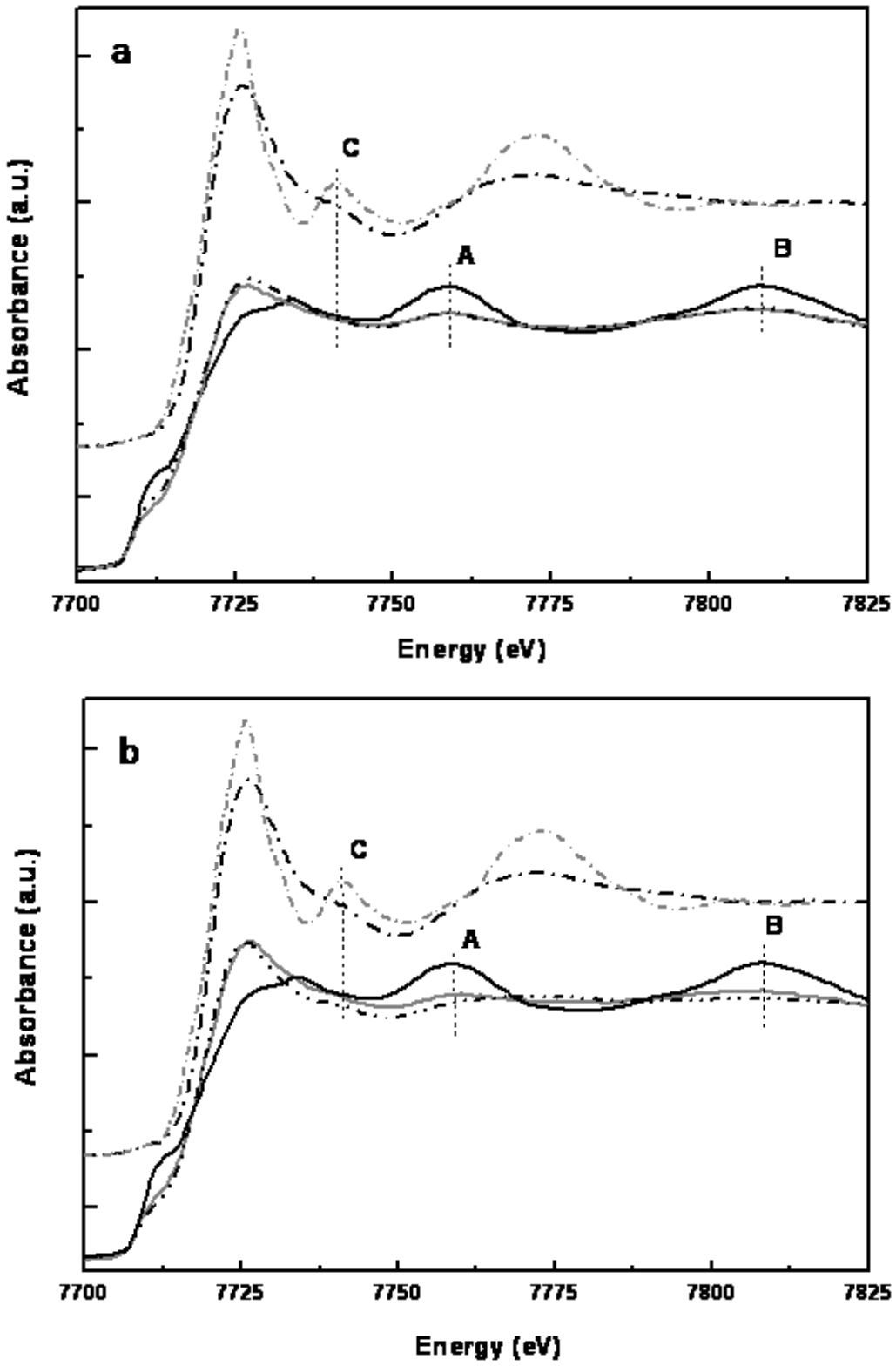

Figure 6.13 Co K-edge XANES spectra of (a): "DCO 6h" (solid gray) and "DCO 9h" (dash dot dot black); (b) "DCO 12h" (symbol gray) and "DCO 18h" (dash dot dot black) in comparison with Co foil (solid black), CoO (dash dot gray), and $CoCO_3$ (dash dot black).

This is strange and contradicts the generally expected particles agglomeration or growth by means of Ostwald ripening at the last stage of the synthesis. Such an unusual behavior is also supported by TEM analysis (Chapter 4, Table 3).

The appearance of an additional shape resonance C at 7738 eV is similar to that of CoO or $CoCO_3$ reference spectra. Also somewhat "washed out" two maxima at 7758.5 and 7808 eV (A and B) characteristic for cobalt metal phase; instead, tendency to one broad maximum indicate about partial oxidation of particles or decoration with a CoO like shell. This evidence is more pronounced for the "DCO 18h" sample.

To further investigate these time-dependent structural changes, the local coordination environment of cobalt atom was probed using EXAFS analysis. Fourier transformed EXAFS spectra of the "DCO 6h", "DCO 9h", "DCO 12h" and "DCO 18h" are present in Figure 6.14. The EXAFS functions, $\chi(k)$, are k^3weighted and Fourier transformed; k range of 2.3-11.3 $Å^{-1}$ is used.

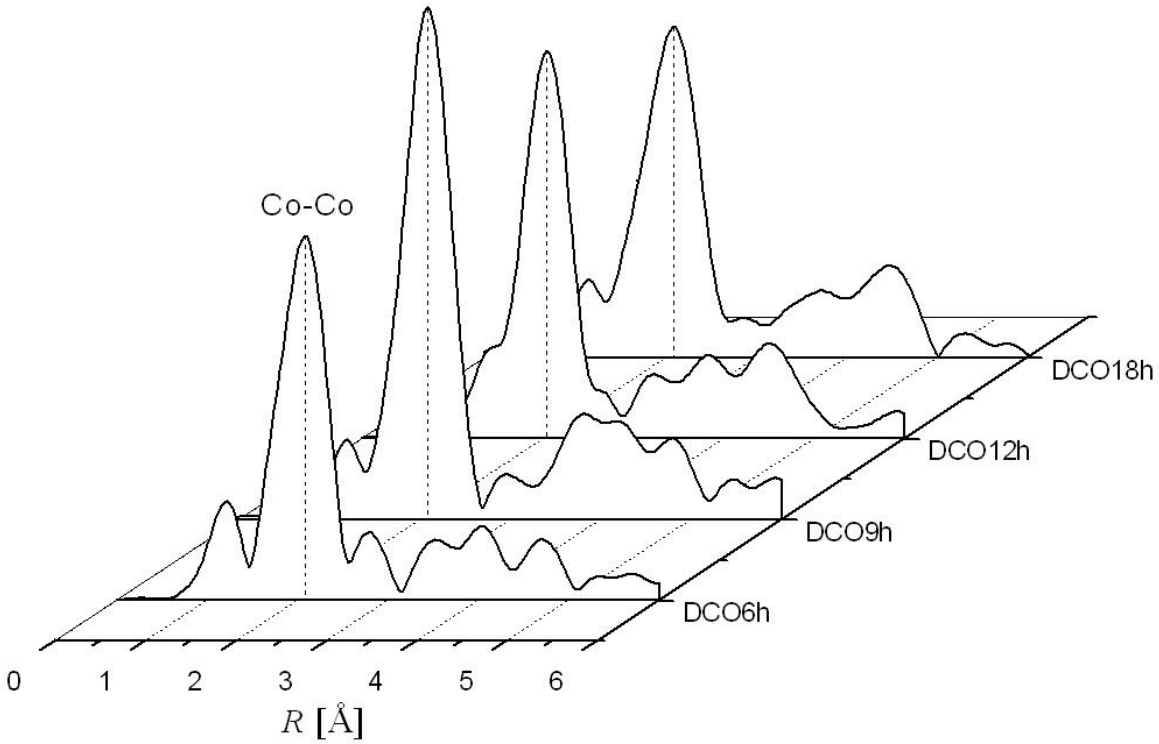

Figure 6.14 FT EXAFS spectra of "DCO 6h", "DCO 9h", "DCO 12h", and "DCO 18h" samples, k^3weighted (not phase corrected).

The time-dependent FT EXAFS data provide a convenient representation of the qualitative changes occurring in the average coordination environment of the absorbing Co atom during the nanoparticles growth process. The FT EXAFS spectra of all samples show observable features at distances as large as 5 Å indicating the presence of medium-range order beyond the first coordination shell. Inspection of the data shows that the intensity of the peak centered at ~2 Å (not phase corrected), resulting from Co-Co bonding interactions, is increasing up to 9 hours of the synthesis, but then decreases. That corresponds to a growth of the nanoparticles followed by a decrease of particles size, as was already suggested in the above analyses. In addition to the

metal contribution all samples also show some structure below 1.5 Å and its amplitude is gradually increasing for 12 and 18 hours samples. These low-*R* peaks result from interactions occurring between the metal and low-*Z* elements (i.e., O or C). This conclusion was confirmed by analyzing this region using suitable model for these bonding interactions (i.e., CoO) (vide infra).

Although it was possible to analyze the EXAFS data recorded at all time intervals (6h, 9h, 12h and 18h), the detailed analysis only for the "DCO 9h" and the "DCO 18h" is present below. This was decided because already from the qualitative analysis it is obvious that samples of 6 and 12 hours of the synthesis are not the crucial points in the path of nanoparticles formation and no new phases are observed at those times. Whereas the "DCO 9h" and the "DCO 18h" are the culminating moments in the synthesis and the information on the final clusters is one of our prime interests.

Figure 6.15 shows the experimental data as well as the results of the EXAFS analysis for the "DCO 9h"sample, which are also summarized in Table 6. Fitting was performed over the 1.4-5.2 Å range. Some oxide atoms are detected in the environment of cobalt absorber atoms. This coordination is logical to expect at the surface of the cobalt nanoparticles due to high air sensitivity of the cobalt. The relative contribution of Co-C coordination is very small. The major neighbors are other Co atoms. An observed decrease in Co-Co bond distance (2.41±0.03 Å compare to the 2.48 Å in the hcp crystal structure) might be caused by several factors such as surface coordination of O, relatively high disorder (σ^2), and imperfection of crystal structure of the nanoparticles.

The FT EXAFS spectra of the "DCO 18h", obtained fits and the best fitting parameters are present in Figure 6.16 and Table 7. Using the XANES indication about Co core CoO-like shell formation for the "DCO 18h" sample it is reasonable to make a model for EXAFS fit which consists of cobalt metal phase and several layers of cobalt oxide. Calculations of the theoretical EXAFS signal of several monolayers of CoO was done with FEFF8 code where contribution of atoms only with z coordinates 0 and 2 Å (corresponding to the two layers of CoO) or 0, 2, and 4 Å (corresponding to the three layers of CoO) were accepted and all the rest atoms are discarded. Particularly the best fit was obtained using the two monolayers of CoO phase. To emphasize the signal from low Z elements (oxide in our case) weighting factor of k^0 was used. Fitting of the higher coordination shells was done with the same modification factor of the degeneracy values and the same Debye-Waller factor obtained for the first shell. This allowed preserving distinct amount of cobalt oxide phase obtained from the fit of the first coordination shell –approximately 25 %. Fitting was performed over the range of 0.6-5.2 Å.

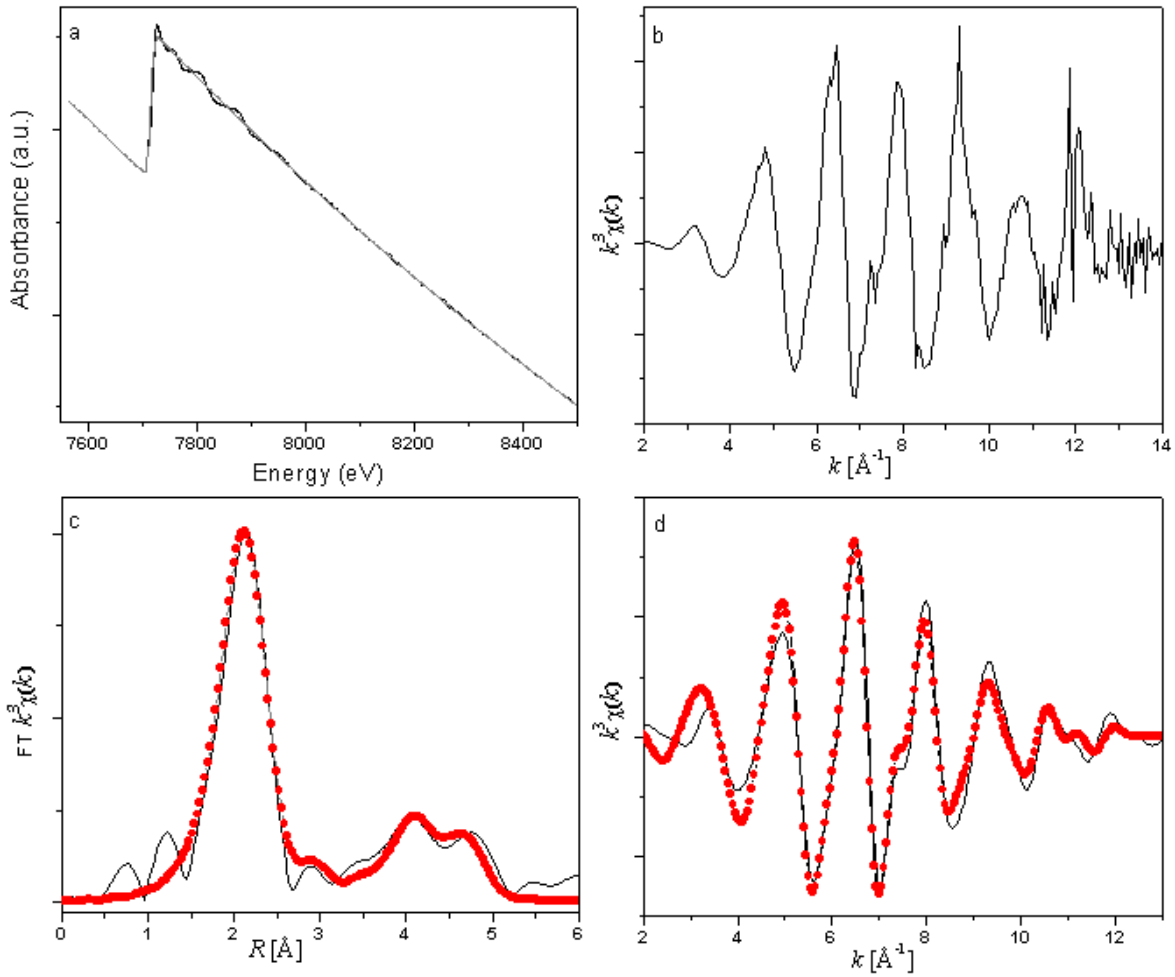

Figure 6.15 Analysis of Co K-edge EXAFS of the "DCO 9h" sample: (a) data and background function, (b) extracted $\chi(k)$, (c) Fourier transformation in k^3-weighting along with fit (circles) and (d) back transformed signal with fit (circles). Uncorrected for photoelectron phase shift.

Table 6 EXAFS fitting parameters for the "DCO 9h" sample.
S_0^2 = 0.825, k-range 2.3-11.3 Å^{-1}, *R*- range 1.4-5.2 Å.

Paths	ΔE_0 [eV]	R [Å]	N	σ^2[Å^2]	*R factor of fit*
Co-O	-2.55±0.33	2.17(C)*	1.1(C)	0.008±0.001	0.06
Co-Co		2.41±0.03	6.2±0.4		
Co-Co		2.50±0.01	2.6±0.4		
Co-C		2.96(C)	1.1(C)		
Co-Co		3.45±0.07	1.1±1.2		
Co-Co-Co-Co		3.77±0.22	19(C)		
Co-Co		4.32±0.03	4.7±2.4		
Co-Co		4.68±0.06	2.5±2.1		
Co-Co-Co-Co		5.04±0.03	4.8±1.5		

* C stands for constrained and indicates that the parameter was fixed in the fit.

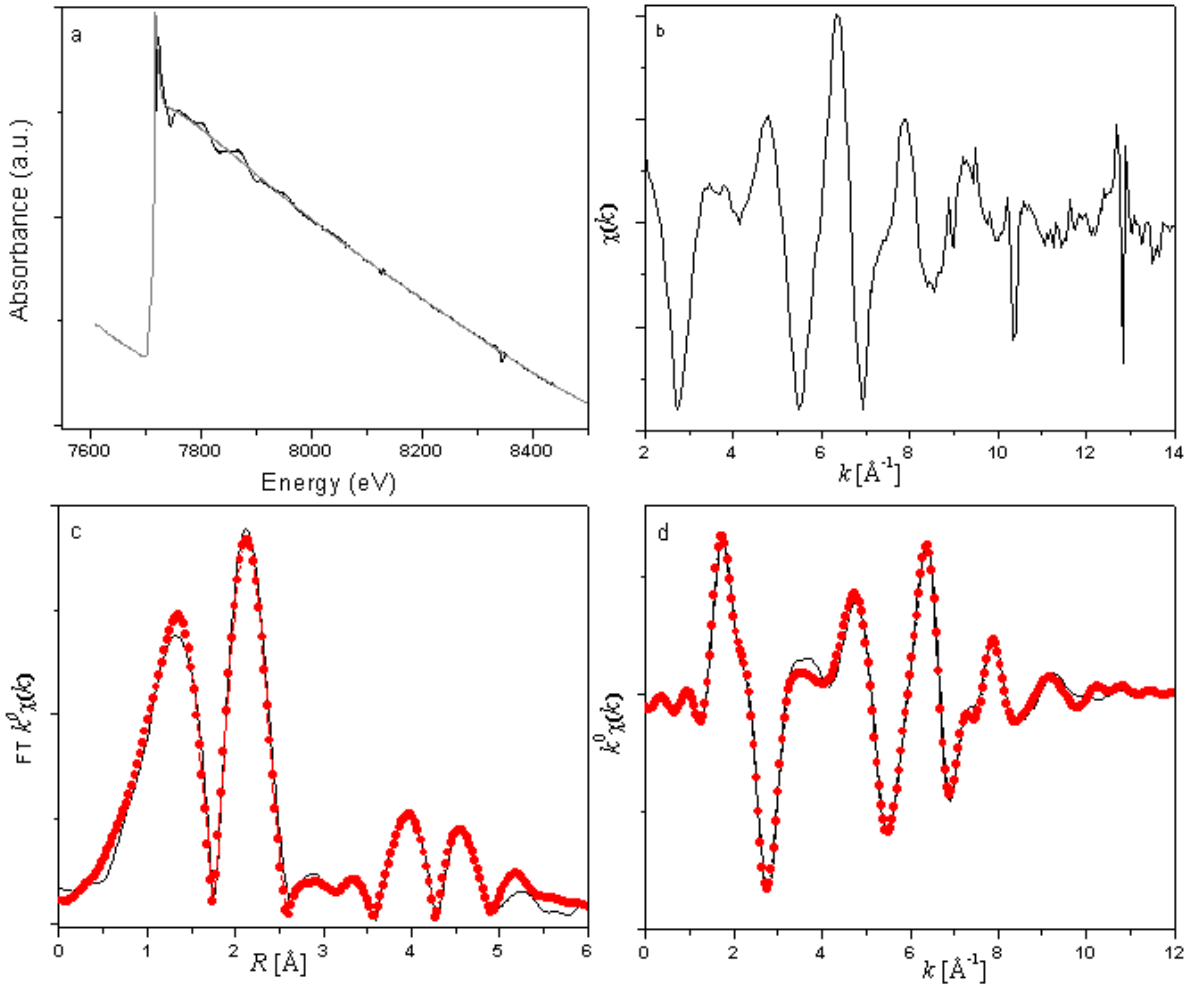

Figure 6.16 Analysis of Co K-edge EXAFS of the "DCO18h" sample: (a) data and background function, (b) extracted $\chi(k)$, (c) Fourier transformation in k^0-weighting along with fit (circles) and (d) back transformed signal with fit (circles). Uncorrected for photoelectron phase shift.

Table 7 EXAFS fitting parameters for the "DCO 18h" sample.
S_0^2 = 0.825, k-range 2.5-10 Å^{-1}, *R* range 0.6-5.2 Å.

Paths	ΔE_0 [eV]	*R* [Å]	*N*	σ^2[Å^2]	*R factor of fit*
CoO phase:					
Co-O	3.6±1.2	1.92±0.03	1.3±0.1	0.003(C)	0.01
Co-Co		2.58±0.02	2.4(C)		
Co-O		3.76±0.08	0.8(C)		
Co-Co		4.22±0.08	0.8(C)		
Co-O		5.11±0.10	2.4(C)		
Co-Co		5.08±0.05	1.6(C)		
Co metal phase:					
Co-Co		2.48±0.01	4.1±0.5	0.005±0.002	
Co-Co		3.58±0.04	0.9±0.2		
Co-Co		4.45±0.02	3.5±1.4		
Co-Co		5.33±0.04	3.0±1.3		

So far the role of aluminumorganics in the synthesis was not specified. As it was shown previously, the molar ratio of $Co_2(CO)_8$ to $Al(R)_3$ as well as the chain length R_3 influences the size of nanoparticles.[67] But no strong (chemical) interaction was observed in the XAS spectra. Therefore, it was concluded that the $Al(R)_3$ plays a more catalytic role in the thermolysis of $Co_2(CO)_8$ and does not react directly with formed Co nanoparticles, but rather detaches the CO from the $Co_2(CO)_8$. However, the stability of the nanoparticles against agglomeration is provided by $Al(R)_3$, therefore some amount of $Al(R)_3$ has to be present in the surface of the nanoparticles. But stabilization against oxidation for as-prepared nanoparticles does not hold. The nanoparticles are highly air sensitive and stabilization against oxidation normally done by additional surfactants which can be adsorbed on the surface of the nanoparticles.

Summing up the results, the following model of the cobalt nanopartice formation may be proposed (Figure 6.17):

1. The decomposition of the DCO complex into the $Co_4(CO)_{12}$ intermediate complex is observed within the first two minutes of the reaction.

2. Further reduction of the $Co_4(CO)_{12}$ complex and removal of CO ligands is followed by nucleation of $Co_2(CO)_m$ ($m \cong 5$) species between 20 and 50 minutes of the synthesis. The nucleation is indicated by shorter metallic spacing in $Co_2(CO)_m$ species compared to M-M bond distance in the intermideate organometallic complexes.

3. The nucleation stage is followed by diffusive agglomerative growth of those initially formed nuclei to a cluster of Co atoms of higher nuclearity along with further decarbonylation. The size of the first detected particles is 1.78±0.01 nm after 3 hours of the synthesis. Formed particles are not “naked” but some CO and $Al(R)_3$ species are adsorbed on the surface.

4. The culminating moment of the growth phase is appeared to be after ~9 hours of the synthesis with averaged size of the particles 7.41±0.09 nm.

5. Surface decoration resulting in metal-core oxide-shell formation is found to be present after the growth phase within the next 9 hours of the synthesis. This process is going at the expanse of outer layer of Co clusters, which became oxidized and the size of the metallic core is reduced to 3.8±0.2 nm.

It should be stressed that the mechanism of the nanoparticle formation is very complicated and the scheme below illustrates a simplistic view of cobalt nanoparticle formation.

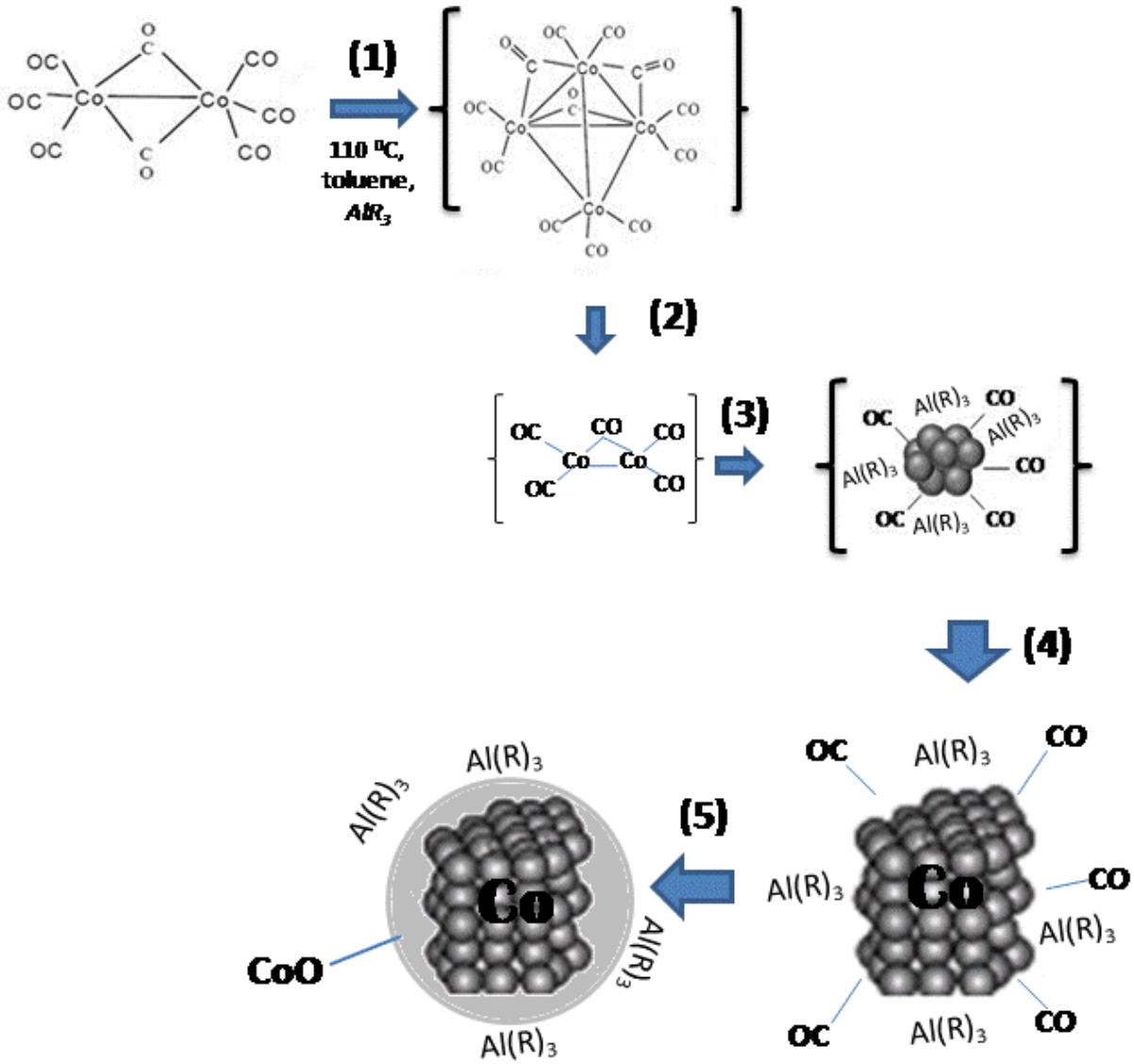

Figure 6.17 Scheme of Co nanoparticle formation from the decomposition of the DCO organometalic complex in the presence of aluminum tryoctal $Al(R)_3$.

6.2 "ADH synthesis"

For a comparative study of the mechanism of Co nanoparticles formation as well as to understand the effect of the nature of the precursor on this mechanism a second synthesis with the ADH precursor was investigated. Time-dependent XANES spectra of the ADH synthesis in comparison with the DCO synthesis are present in Figure 6.18.

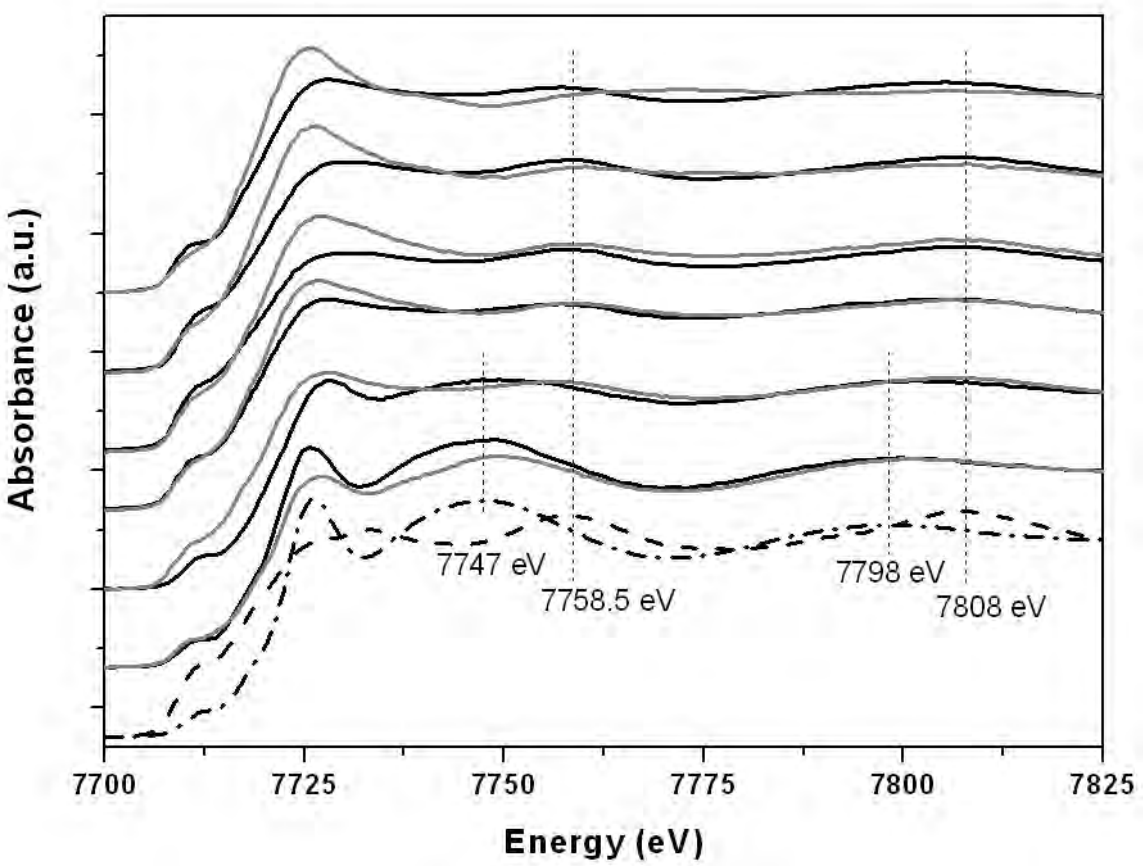

Figure 6.18 Co K-edge XANES spectra of the ADH synthesis (solid black) in comparison with the DCO (solid gray) from top to bottom: 18h, 12h, 9h, 6h, 3h, 2min. Co foil (dash black) and ADH (dash dot black) reference spectra are shown in the lower panel of the graph.

Looking at the spectra of the two syntheses, it turns out that particles resulting from the ADH precursor are obviously free from any oxygen impurities on the surface since neither chemical shift of the absorption edge to higher energy, nor systematically higher white line intensity are observed compared to the respective DCO synthesis. The pre-edge intensity is in many cases even higher than for the DCO synthesis.

The features of the ADH time-dependent spectra also can be assigned to different phases of Co nanoparticles formation. Following similar arguments as in the case of the DCO synthesis, we can distinguish three stages in the reaction pathway. Spectra of the "ADH 2 min" and "ADH 3h" belong to the nucleation stage, since the WL appearance and the shape resonances at 7747 and 7798 eV are similar to the positions of cobalt organometallic complexes like the ADH or "DCO 2 min" but differ from the Co metal phase (7758.5 and 7808 eV).

The spectrum of the “ADH 6h” is becoming more similar to the Co metal phase and very similar to the “DCO 3h” spectrum (Figure 6.19). The increased pre-edge intensity, the WL appearance as well as the energy positions of the shape resonances at 7757 and 7806 eV are comparable to those of Co foil; that suggest the formation of Co clusters with some CO bonds at the surface.

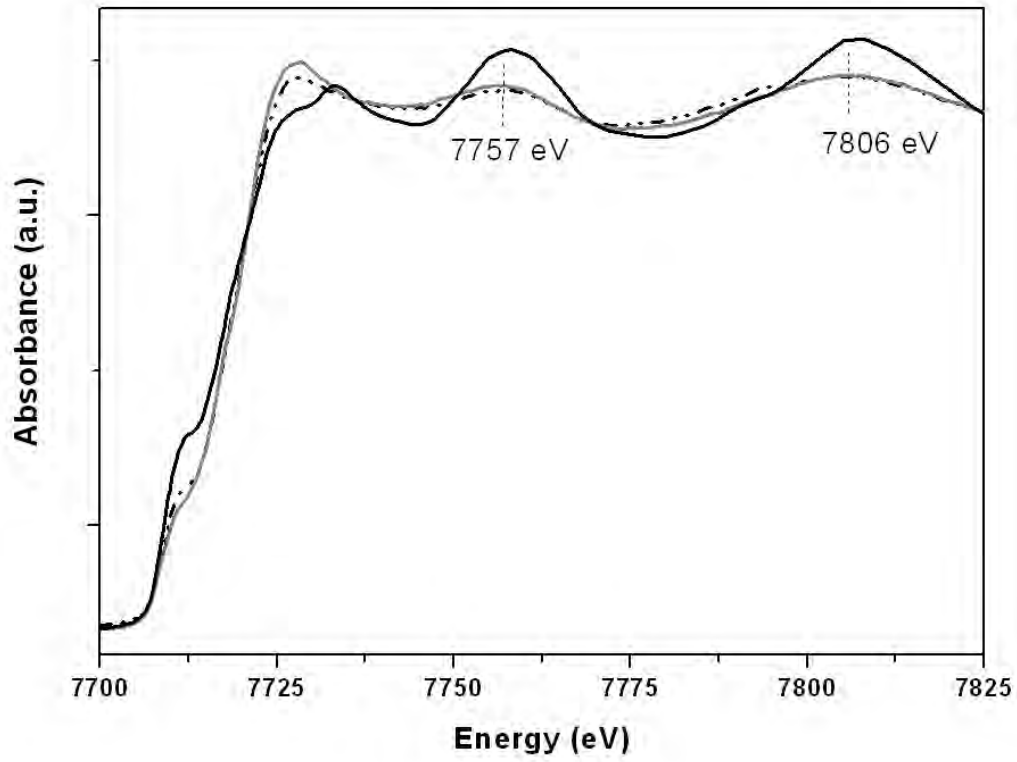

Figure 6.19 Co K-edge XANES spectra of the “ADH 6h” (dash dot dot black) in comparison with the “DCO 3h” (solid gray) and Co foil (solid black) spectra.

Further on since 6 hours up to 9 hours of the synthesis particles are growing. In the ADH like in the DCO synthesis, sample taken at 9 hours presents the culminating moment of the growth phase. The decreased intensity of the WL and considerably increased pre-edge intensity also indicate that particles are becoming more metallic via a further decarbonylation process (Figure 6.20). Very good agreement with the spectrum of Co foil is observed with respect to those spectral features as well as position of the shape resonance. However, the two peaks in the white line are not resolved as in the Co foil spectrum. The shape of the WL of the “ADH 9h” spectrum does not show resemblance neither to the fcc phase, as there is no increased WL, nor to the Co foil hcp because second peak at 7734 eV are also not presented (see Figure 6.4 for reference spectra of hcp and fcc phases). In fact, results of magnetic measurements (see Appendix A) suggest the presence of both phases- hcp and fcc.

The “ADH 12h” and “ADH 18h” spectra show more resemblance to the fcc phase with the WL maximum shifted to the lower energy ~7727 eV (Figure 6.20). Also the decrease of the pre-edge intensity form the “ADH 12h” to the “ADH 18h” indicates that a particle size decreases like it was observed earlier in the DCO synthesis. However the changes appeared between 9 and 18 hours of the ADH synthesis are different from the surface decoration observed for the “DCO 12h” and “DCO 18h” samples. For both spectra the “ADH 12h” and “ADH 18h” the two

maxima over 7750 eV region identical to the Co metal spectrum are observed (Figure 6.18). On the nanoscale, contribution of the surface energy term increasing for small particles can cause a complete or partial phase transition. Therefore, the present changes for the “ADH 12h” and the “ADH 18h” might be correlated with the formation of cobalt fcc phase. It should be noted here that the DCO synthesis does not possess such clarity about phase transformation because of the CoO phase contribution.

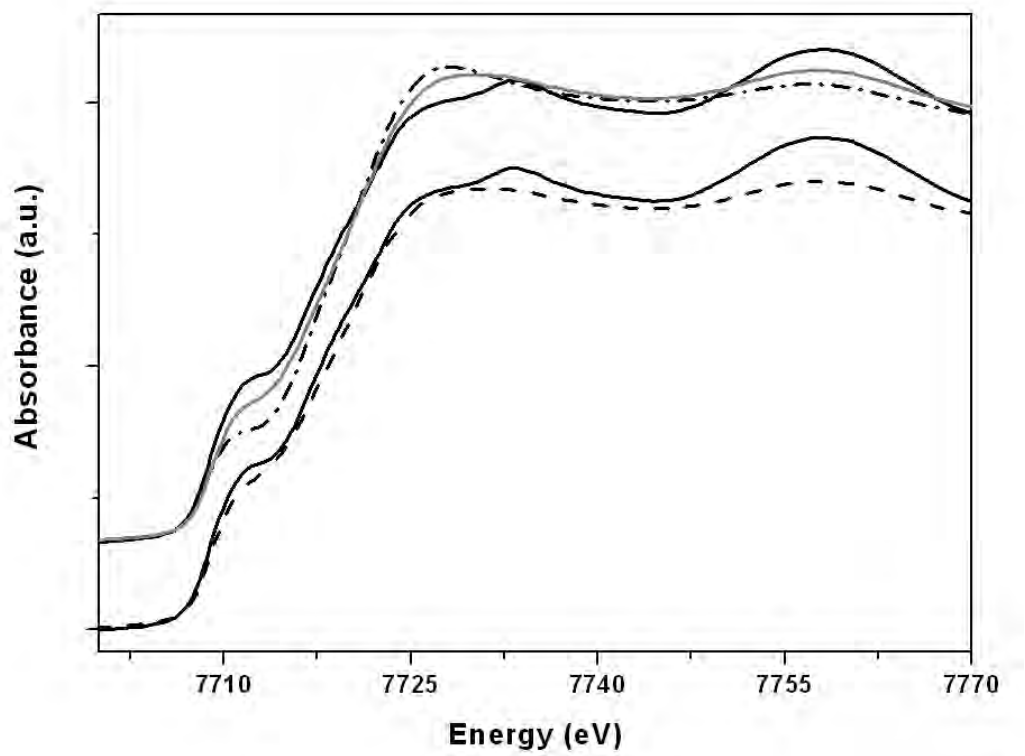

Figure 6.20 Co K-edge XANES spectra of the “ADH 9h” (dash black) “ADH 12h” (solid gray) and “ADH 18h” (dash dot black) in comparison with Co foil (solid black).

From the comparison of the DCO and ADH synthesis it is obvious that the ADH precursor has a different decomposition rate, compare to the DCO. Different kinetic behavior occurs before nucleation, which is clearly observed from the comparison of time dependent XANES spectra of the ADH samples to the DCO. To follow the decomposition of the ADH precursor additional spectra between 2 minutes and 3 hours of the reaction were recorded like in the DCO synthesis (Figure 6.21).

From the first look the changes in the corresponding XANES spectra are qualitatively similar to those observed in the DCO synthesis, but on a different time scale. Also here moderate changes in the WL region corresponding to the varying local CO environment around the absorbing atom during the decomposition are observed. Significant structural rearrangements observed for the “DCO 30 min” in this case appeared at ~1 hour of the synthesis.

Quantitative structural information about Co coordination environment and various intermediate species were obtained by analyzing corresponding Fourier transforms of k^3 weighting $\chi(k)$ Co K-edge EXAFS and back transformed signal (Figure 6.22- Figure 6.24). *k*-range of the Fourier

transform and *R*-range of fitting were 2-10.5 $Å^{-1}$ and 1-3 Å, respectively. Table 8 shows the structural parameters obtained by the fitting analysis.

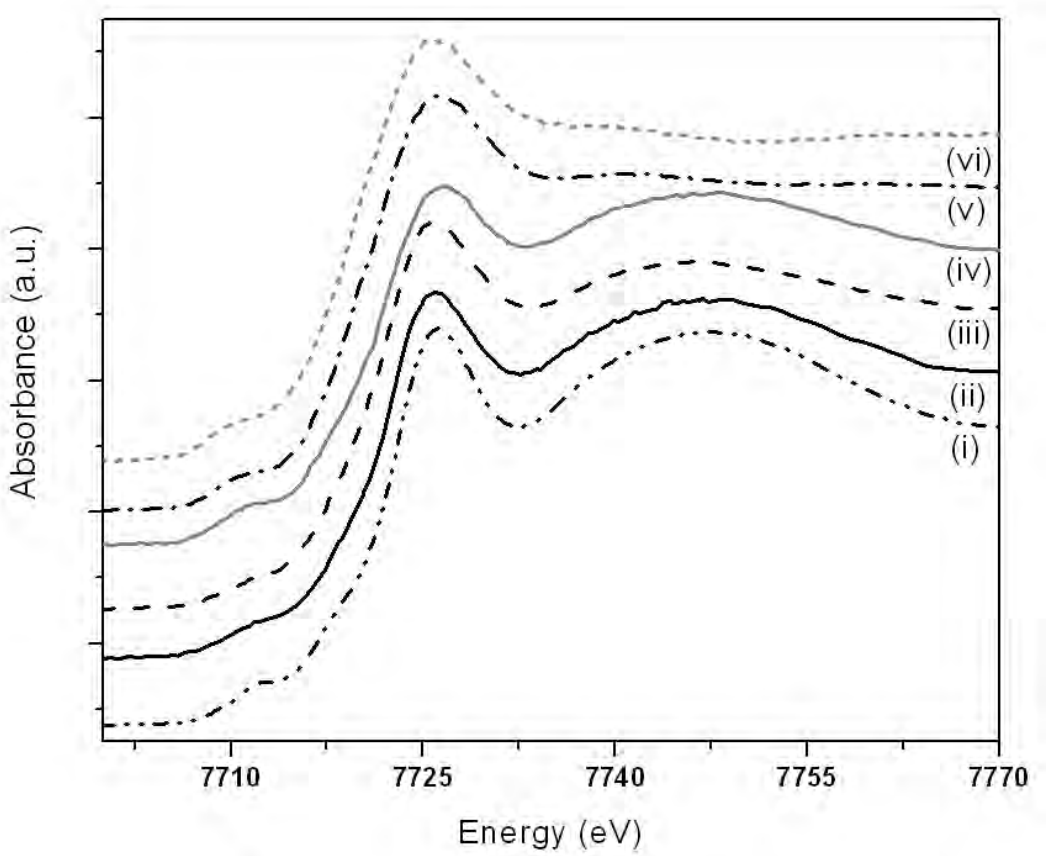

Figure 6.21 Co K-edge XANES spectra i) ADH, ii) "ADH 2 min", iii) "ADH 10 min", iv) "ADH 30 min", v) "ADH 1h", vi) "ADH 3h".

EXAFS spectrum of the ADH starting complex was fitted with Co-C bonds at 1.86 Å and 2.55 Å distances and Co-Co bond at 2.75 Å. After 10 min of the synthesis the intensity of the Co-C peaks begin to decrease and the Co-Co increases. The EXAFS signal after 30 minutes required an additional bond to fit the data, suggesting that the "ADH 30 min" is a mixture of two different intermediate species. In fact, this was observed already in a previous study.[61] Decomposition of the ADH under identical conditions as for the DCO monitored by FT-IR at regular intervals shows no formation of the intermediate, $Co_4(CO)_{12}$ as was observed for the DCO. However, it was found that a mixture of tricyclic organocobalt complexes, $[Co_3(CO)_9CCOOCH_3]$ and $[Co_3(CO)_9CCH_3]$ is formed. After 1 hour of the synthesis the intensity of the Co-Co peak is decreased and the peak shifted to 2.38 Å. The shortest metal-metal bond distances observed at this point of time are more similar to the final close-packed structure (2.49 Å) than to that of the precursor (2.75 Å) and reflect the nucleation process. The "ADH 1h" spectrum was fitted with CN of 1.9 for the Co-Co bond and of 2.9 for the Co-C bond, suggesting a $Co_3(CO)_3$ as a stable nuclei. After 3 hours of the synthesis the Co-C peaks disappears, Co-Co distance becomes more similar to the final close-packed structure and the intensity of this peak is increasing, suggesting the growth of the cluster.

In Figure 6.25 the evolution of the first-shell coordination environment during the nucleation as a function of time is present. It should be noted that after 30 minutes of the synthesis two intermediates were considered but only one is shown in the diagram with averaged Co-Co bond CN=2 and Co-C CN=1.5. Constant linear decrease of Co-C coordination numbers suggest more gradual ADH decomposition compare to that observed for the DCO complex earlier.

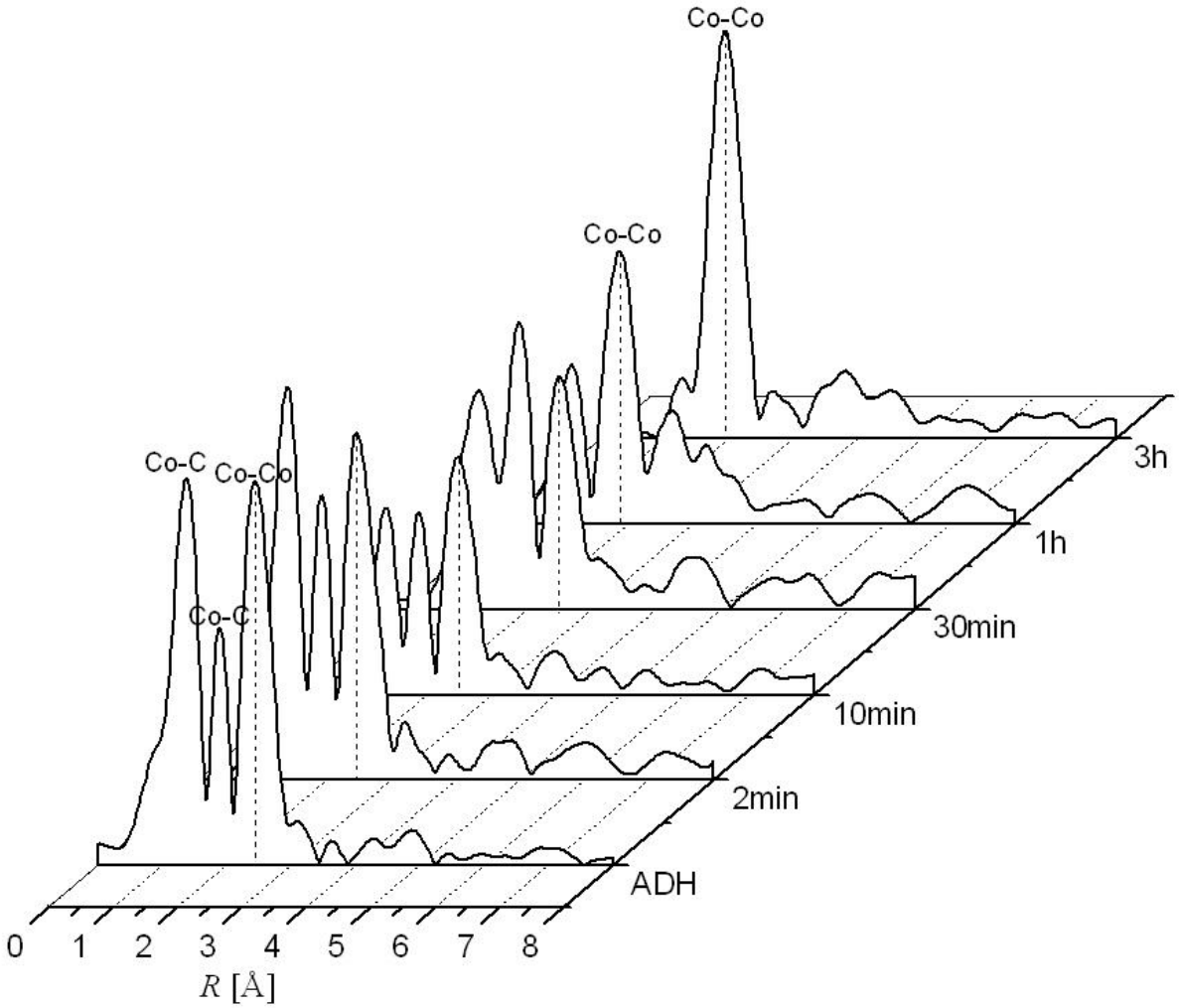

Figure 6.22 FT EXAFS spectra of the ADH starting complex, "ADH 2 min", "ADH 10 min", "ADH 30 min", "ADH 1h" and "ADH 3h" samples, k^3weighted (not phase corrected).

Different decomposition rates as well as different intermediates of the DCO and ADH lead to different concentrations and sizes of initial Co nuclei formed, which also was observed in the previous investigation.[61] Higher rate of the DCO decomposition led to a larger number of smaller nuclei, while slower decomposition rate of the ADH gave rise to a smaller number but nuclei of bigger size. The size of initially formed particles observed after 3 hours of the ADH synthesis is found to be 4.49 ± 0.09 nm compare to 1.78 ± 0.01 nm of the DCO synthesis.

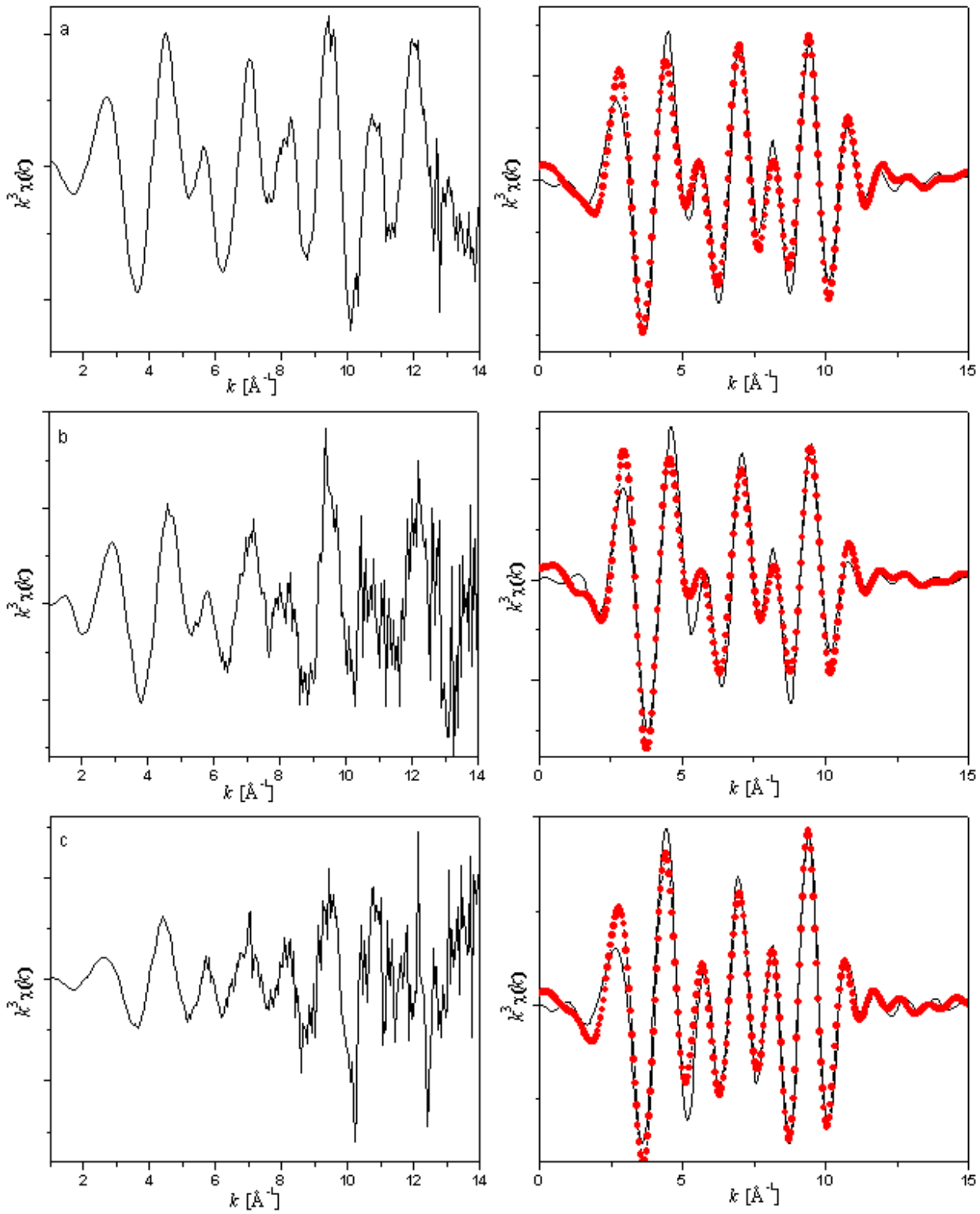

Figure 6.23 k^3weighted $\chi(k)$ Co K-edge EXAFS (left panel) and corresponding back transformed data and fit (right panel) of the a) ADH, b) "ADH 2min", c) "ADH 10 min". Data are depicted as solid lines and fits as solid circles.

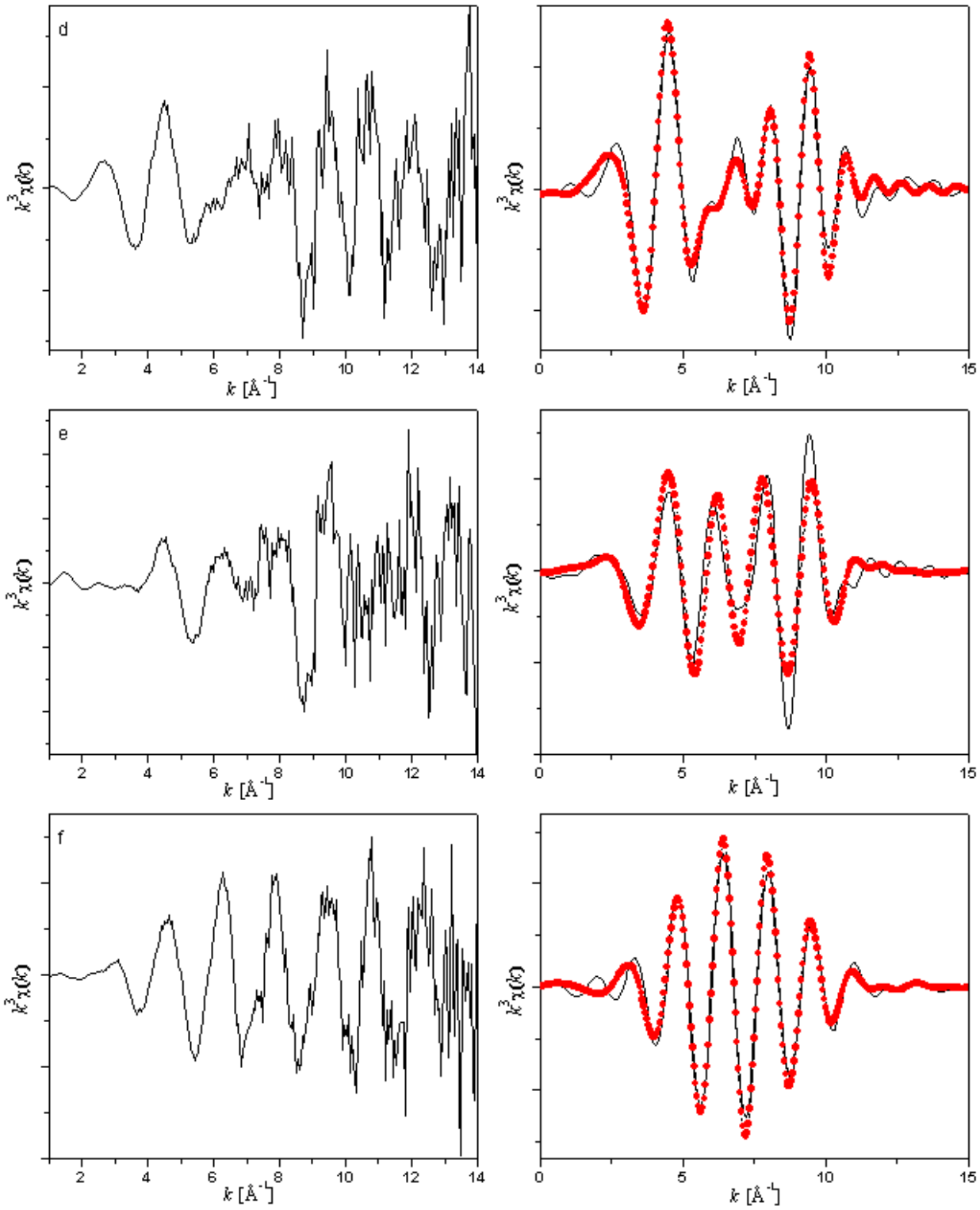

Figure 6.24 k^3weighted $\chi(k)$ Co K-edge EXAFS (left panel) and corresponding back transformed data and fit (right panel) of the d) "ADH 30 min", e) "ADH 1h", f) "ADH 3h". Data are depicted as solid lines and fits as solid circles.

Table 8 EXAFS fitting parameters for the ADH "ADH 2 min", "ADH 10 min", "ADH 30 min", "ADH 1h" and "ADH 3h" samples. S_0^2= 0.825, k-range 2-10.5 Å^{-1}, *R*- range 1-3 Å.

Paths	N	*R* [Å]	σ^2[Å^2]
ADH (ΔE_0=12.1±1.4 eV, *R factor of fit* 0.03)			
Co-C	3.2±1.2	1.86±0.07	0.004±0.003
Co-C	6.3±1.3	2.55±0.02	0.004±0.003
Co-Co	2.6±1.2	2.75±0.01	0.004±0.003
"ADH 2 min" (ΔE_0=10.1±0.7 eV, *R factor of fit* 0.05)			
Co-C	3.1±1.0	1.85±0.09	0.004±0.001
Co-C	6.5±1.3	2.54±0.02	0.004±0.001
Co-Co	2.2±0.2	2.75±0.01	0.003±0.001
"ADH 10 min" (ΔE_0=10.2±1.1 eV, *R factor of fit* 0.05)			
Co-C	1.5±0.6	1.85±0.09	0.004±0.001
Co-C	5.8±0.5	2.56±0.01	0.004±0.001
Co-Co	2.3±0.3	2.77±0.01	0.003±0.001
Co-C	3.3±0.9	2.98±0.02	0.004±0.001
"ADH 30 min" (ΔE_0=6.3±3.4 eV, *R factor of fit* 0.06)			
Co-C	1.5±0.5	1.74±0.04	0.004±0.001
Co-C	1.6±0.9	1.98±0.07	0.004±0.001
Co-C	9.7±1.9	2.54±0.02	0.004±0.001
Co-Co	4.1±1.0	2.75±0.01	0.003±0.001
Co-C	9.3±4.3	2.92±0.01	0.004±0.001
"ADH 1h" (ΔE_0= -11.1±4.6 eV, *R factor of fit* 0.21)			
Co-C	1.1±0.4	1.75±0.02	0.002±0.001
Co-Co	1.9±0.2	2.38±0.02	0.006±0.002
Co-C	1.8±1.2	2.92±0.01	0.002±0.001
"ADH 3h" (ΔE_0= -10.3±3.8 eV, *R factor of fit* 0.03)			
Co-Co	3.2±0.8	2.41±0.07	0.008±0.002

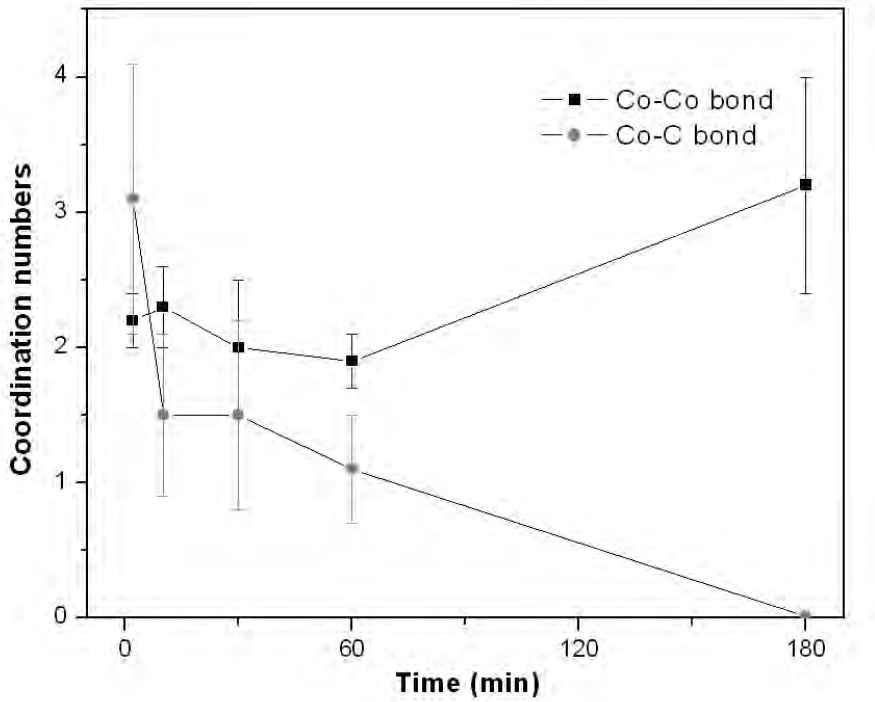

Figure 6.25 Variation of Co-Co and Co-C nearest neighbor bond CN as functions of synthesis time.

Qualitative changes occurring in the average coordination environment of the absorbing Co atoms from 9 hours up to 18 hours of the synthesis are present in the FT k^3 weighted EXAFS data of the "ADH 9h", "ADH 12h", and "ADH 18h" (Figure 6.26). The FT EXAFS spectra of all samples show observable features at distances as large as 5 Å indicating the presence of medium-range order. The positions of Co-Co peak at ~2.1 Å (not phase corrected) are almost identical for all samples, but the amplitude of this peak has decreased for the "ADH 18h" spectrum compared to the "ADH 9h". This situation is similar to the one observed earlier in the DCO synthesis and indicates that particles size has again decreased.

The three resolved peaks beyond the first coordination shell are changing their positions and relative amplitudes during the time of the synthesis. As in XANES, the positions and relative amplitudes are characteristic features and can serve as a fingerprint of the distinct phase. For example, in Figure 6.27 FEFF8 calculated FT EXAFS spectra of cobalt hcp and fcc are presented, where significant differences in the higher coordination shells are observed. The changes observed between the "ADH 9h" and "ADH 18h" are similar to those between the hcp and fcc phases and corroborate the XANES analysis. The relative amplitudes of the "ADH 9h" spectrum are more similar to the hcp phase with the I and the III peaks are close in intensity and the II one been the highest. In the "ADH 18h" only II and III peaks are well resolved and the I peak is damped which refer to the fcc structure.

In attempt to differentiate between the two phases for the "ADH 9h" sample, two independent fits were carried out using the hcp and fcc theoretical models. The EXAFS functions, $\chi(k)$, are k^3weighted and Fourier transformed in the k range of 2-12 $Å^{-1}$. Fitting is done in R space over the range of 1.4-5.1 Å. The results are present in Figure 6.28 and the best fit parameters are summarized in Table 9 for comparison.

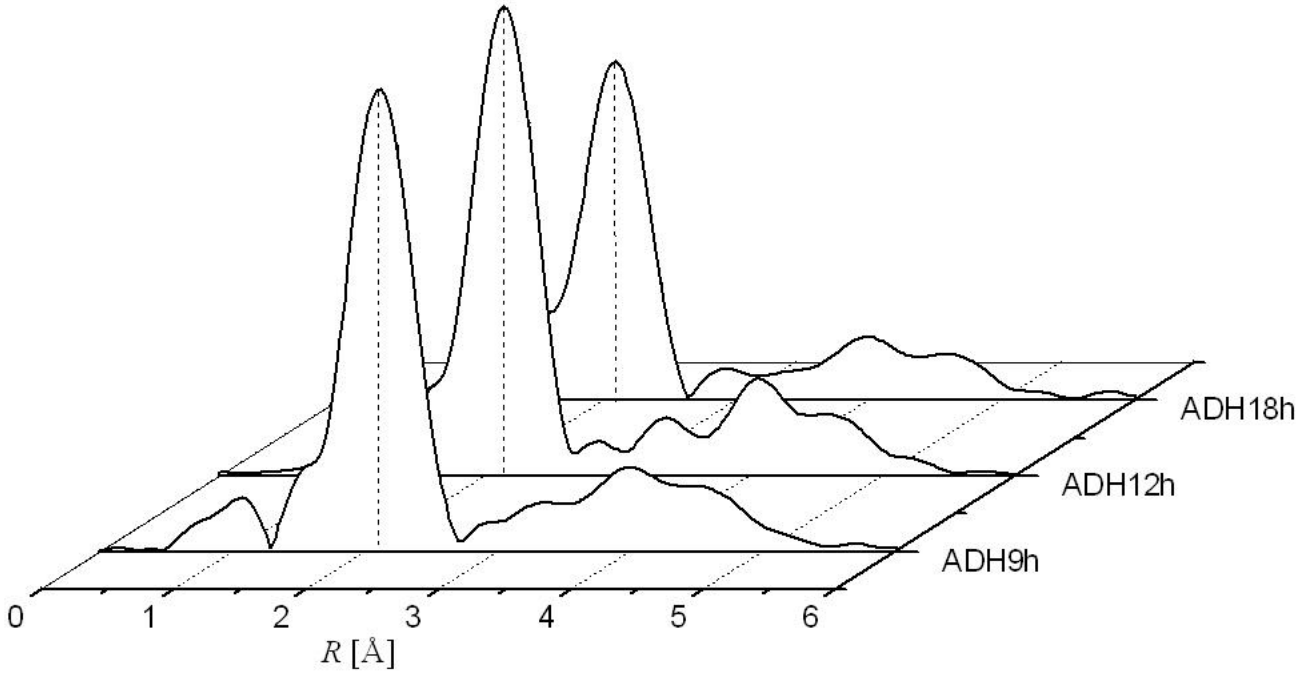

Figure 6.26 FT EXAFS spectra of the "ADH 9h", "ADH 12h" and "ADH 18h" samples, k^3weighted (not phase corrected).

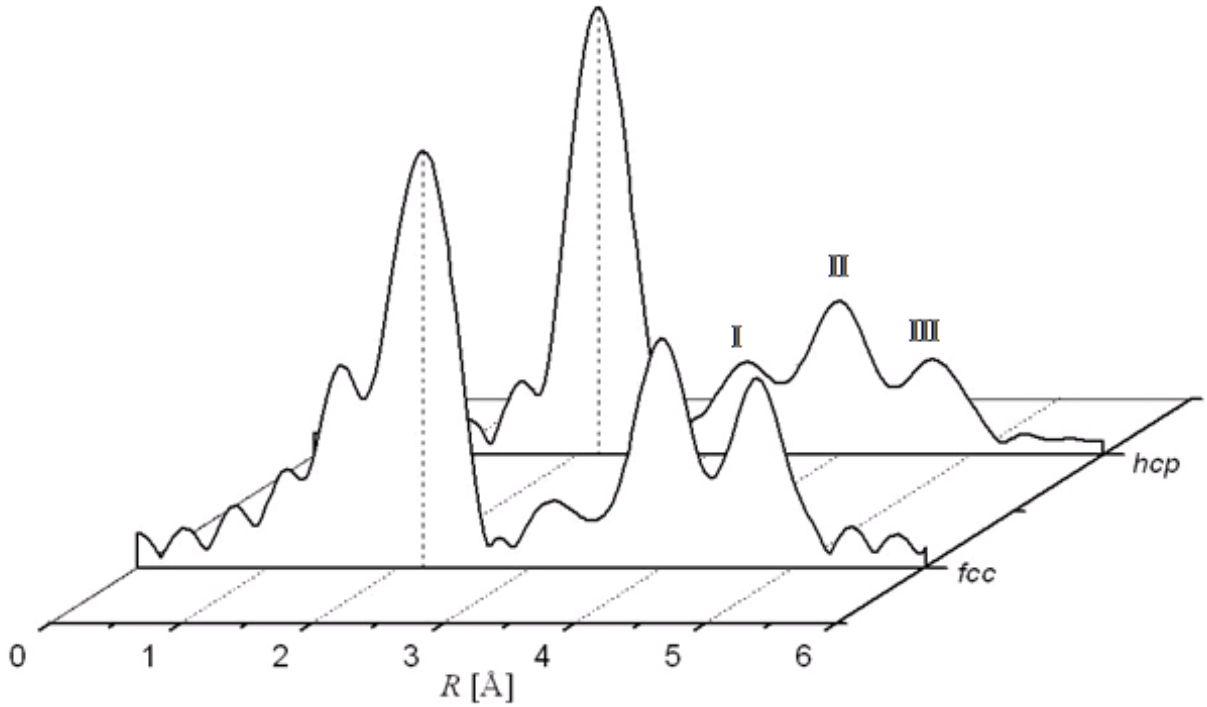

Figure 6.27 FEFF8 calculated FT EXAFS spectra of the cobalt hcp and fcc phases, k^3weighted (not phase corrected).

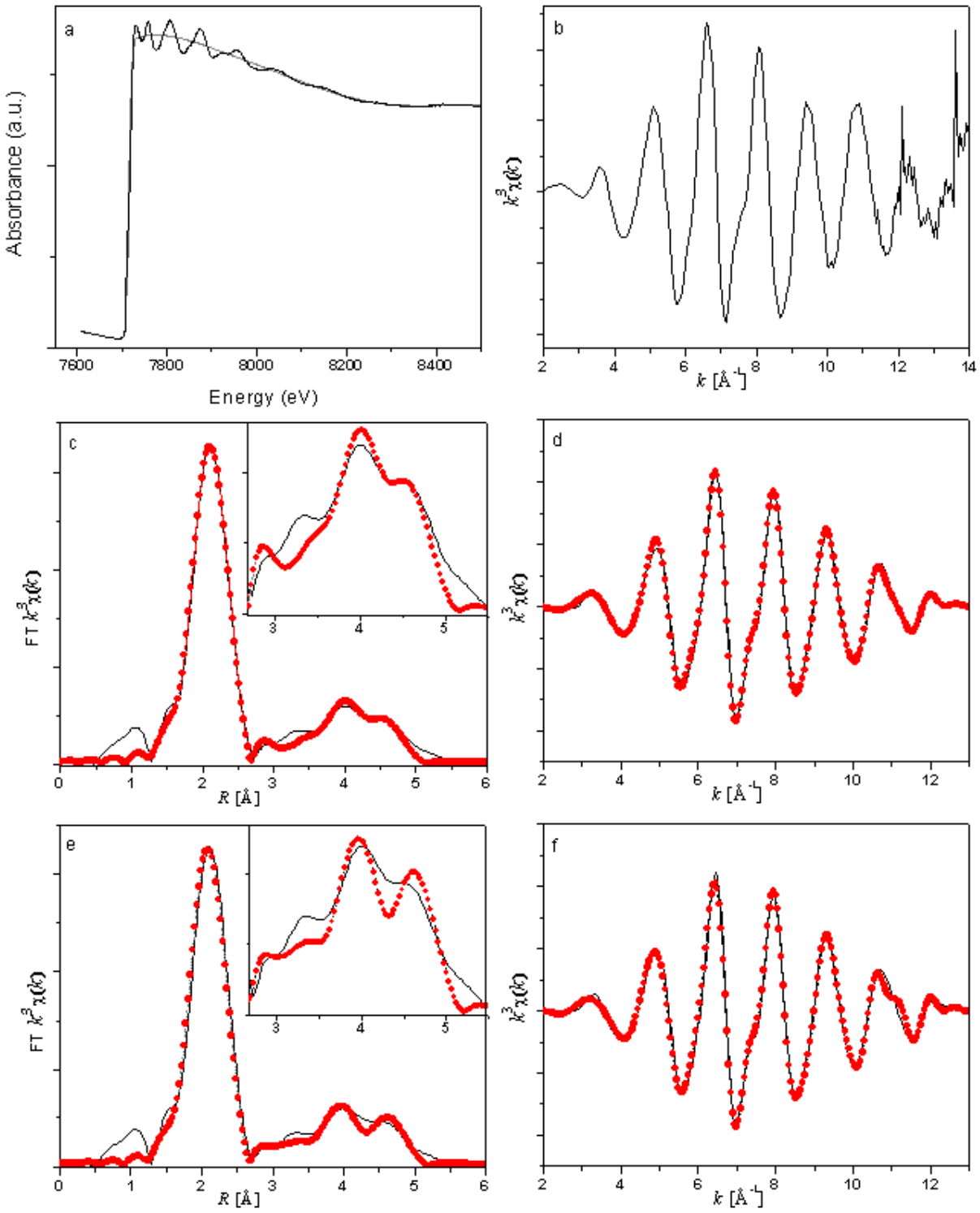

Figure 6.28 Analysis of Co K-edge EXAFS of the "ADH 9h" sample: (a) data and background function, (b) extracted χ (k), (c) Fourier transformation in k^3-weighting along with hcp fit (circles) and (d) back transformed signal with fit (circles), (e) and (f) FT and back transformed signal with fcc fit, respectively. Uncorrected for photoelectron phase shift. Enlarged view of higher coordination shells are shown in the insets.

Table 9 EXAFS fitting parameters for "ADH 9h" sample. S_0^2= 0.825, k-range 2-12 Å^{-1}, *R* range 1.4-5.1 Å.

fit parametrs	fcc	theoretical values	fit parametrs	hcp	theoretical values
ΔE_0 [eV]	-3.2±0.4		ΔE_0 [eV]	-3.2±0.4	
σ^2 [Å^2]	0.007±0.001		σ^2 [Å^2]	0.006±0.001	
R_{Co-Co}, [Å] N_{Co-Co}	2.47±0.01 5.9±0.6	2.51	R_{Co-Co}, [Å] N_{Co-Co}	2.48±0.01 6.2±0.1	2.49
R_{Co-Co}, [Å] N_{Co-Co}	3.48±0.02 1.16±0.41	3.55	R_{Co-Co}, [Å] N_{Co-Co}	3.48±0.03 0.9±0.5	3.54
			R_{Co-Co}, [Å] N_{Co-Co}	4.17±0.11 1(C)	4.07
R_{Co-Co}, [Å] N_{Co-Co}	4.32±0.01 4.4±0.7	4.34	R_{Co-Co}, [Å] N_{Co-Co}	4.32±0.01 3.1±0.5	4.34
			R_{Co-Co}, [Å] N_{Co-Co}	4.75±0.01 3.2±0.8	4.78
$R_{Co-Co-Co-Co}$, [Å] N_{Co-Co}	5.04±0.01 3.3±0.6	5.02	$R_{Co-Co-Co-Co}$, [Å] N_{Co-Co}	5.07±0.01 1.7±0.5	5.07
χ_ν^2	46		χ_ν^2	22	
R factor of fit	0.01		*R factor of fit*	0.006	

The fitting of the first coordination shell peak (1.4÷2.5 Å) does not support the presence of a light backscatterer, such as O or C, around the absorbing atom. This confirms the XANES analysis. Both hcp and fcc models produced reasonably good fits in the first coordination shell, but in the higher coordination shells from the visual inspection (insets Figure 6.28) we can conclude that fit produced by hcp model more resembles to the data. Also, comparing the "goodness" and uncertainties of the fits we get more proof of the predominantly hcp phase of the particles, as *R factor* and reduced chi-square (χ_ν^2) of the hcp fit are considerably smaller than those of the fcc. The parameters obtained for both fits are nearly identical, but at the same time they both differ from the theoretical values. Therefore both phases hcp and fcc might be present, as was also suggested by the results of magnetic measurements (Appendix A).

For the "ADH 18h" sample an excellent fit was obtained based on the fcc model, as was predicted by XANES and EXAFS "fingerprint" analyses. The fitting parameters are identical to those of the "ADH 9h" sample (vide supra); the results are presented in Figure 6.29 and summarized in Table 10.

In order to explain the hcp and fcc phase formation and further hcp-fcc phase transformation of nanosized cobalt the thermodynamic properties and the stability of grain boundaries in nanometric metals and the concept of the lattice stability should be considered.

From the thermodynamic point of view, nanopowder is a metastable state whose Gibbs free energy is greater than that of the bulk state, suggesting the existence of activation energy. Activation energy can be calculated from the values of the maximum and minimum excess Gibbs free energies.[68] The excess Gibbs free energy, given by equation $\Delta G(V,T) = \Delta H(V,T) - T\Delta S(V,T)$, where ΔH, ΔS and ΔV are the enthalpy, entropy and volume gradient ($\Delta V = 0.0$ value corresponds to the crystalline state), respectively. For nanocrystalline Co hcp at 300 K the value of the activation energy is 1.05 x 10−20 J/atom or about 0.066 eV/atom.[69] Using the concept of lattice stability it is possible to estimate the excess Gibbs free energy for the fcc phase. The lattice stability parameter for cobalt hcp with respect to cobalt fcc is $Co_{fcc \rightarrow hcp}$ = [-460 + 0.628 T] (J mol^{-1}). At 300 K, the value of the lattice stability parameter is about -271.6 (J mol^{-1}) or -28 x 10^{-4} (eV/atom), i.e. a very small value.[69] Thus the Gibbs free energies of the hcp and fcc phases are almost equal and both phases can be formed during the synthesis. The relationship between these two close packed geometries was already present early in this chapter through the stacking sequences …ABCABCA… for the hcp and …ABABA… for the fcc differs only in the position of second nearest neighbors. The hcp-fcc transformation occur as a displacement of the crystal lattice in each second nearest layer by an amount of $a/3[120]_{hcp}$. The $[001]_{hcp}$ direction becomes a cubic $< l\ l\ l >_{fcc}$ direction and one of the close packed rows $[100]_{hcp}$ or $[110]_{hcp}$ coincides with a cubic $<211>_{fcc}$ direction. The hcp- fcc phase transformation is caused by stacking faults. The first stage of the transformation corresponds to noncooperative movements of atoms (fluctuations of the boundaries). The driving forces for this type of transformation are possibly of electronic nature as suspected by Christian.[70]

In summary a pathway of Co nanoparticles formation from the ADH organometalic precursor can be proposed (Figure 6.30):

1. The ADH organometallic complex decomposed into the two intermediate complexes $[Co_3(CO)_9CCOOCH_3]$ and $[Co_3(CO)_9CCH_3]$ after 10 minutes of the reaction.

2. The removal of CO ligands is followed by nucleation of $Co_3(CO)_3$ metallic species between 30 minutes and 1 hour of the synthesis.

3. The slow decomposition rate of the ADH gives rise to nuclei of bigger size. The size of initially formed particles observed after 3 hours of the synthesis is found to be 4.49 ± 0.09 nm.

4. Like in the DCO synthesis the nucleation stage is followed by diffusive agglomerative growth of those initially formed nuclei to a cluster of Co atoms of higher nuclearity and also completed after ~9 hours of the synthesis with averaged size of the particles 5.00 ±0.05 nm.

5. The hcp-fcc phase transformation is found to take place after the growth of the nanoparticles.

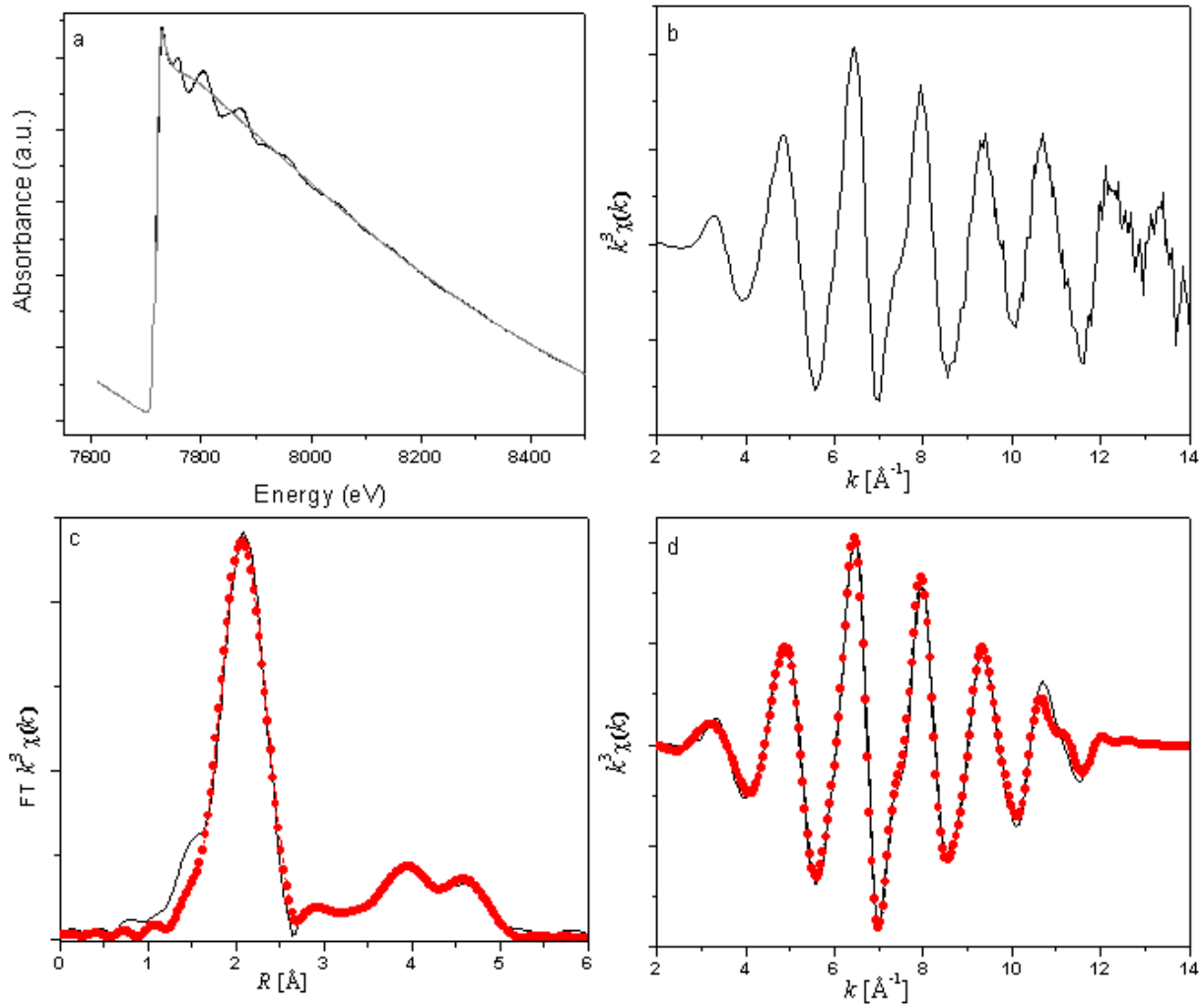

Figure 6.29 Analysis of Co K-edge EXAFS of the "ADH18h" sample: (a) data and background function, (b) extracted $\chi(k)$, (c) Fourier transformation in k^3-weighting along with fit (circles) and (d) back transformed signal with fit (circles). Uncorrected for photoelectron phase shift.

Table 10 EXAFS fitting parameters for the "ADH 18h" sample. S_0^2= 0.825, k-range 2-12 Å^{-1}, R range 1.4-5.1 Å.

Paths	ΔE_0 [eV]	R [Å]	N	σ^2[Å^2]	*R factor of fit*
Co-Co	-3.39±0.5	2.47±0.01	5.43±0.2	0.009±0.001	0.007
Co-Co		3.45±0.02	1.07±0.4		
Co-Co		4.31±0.01	4.05±0.8		
Co-Co		5.03±0.01	3.22±0.7		

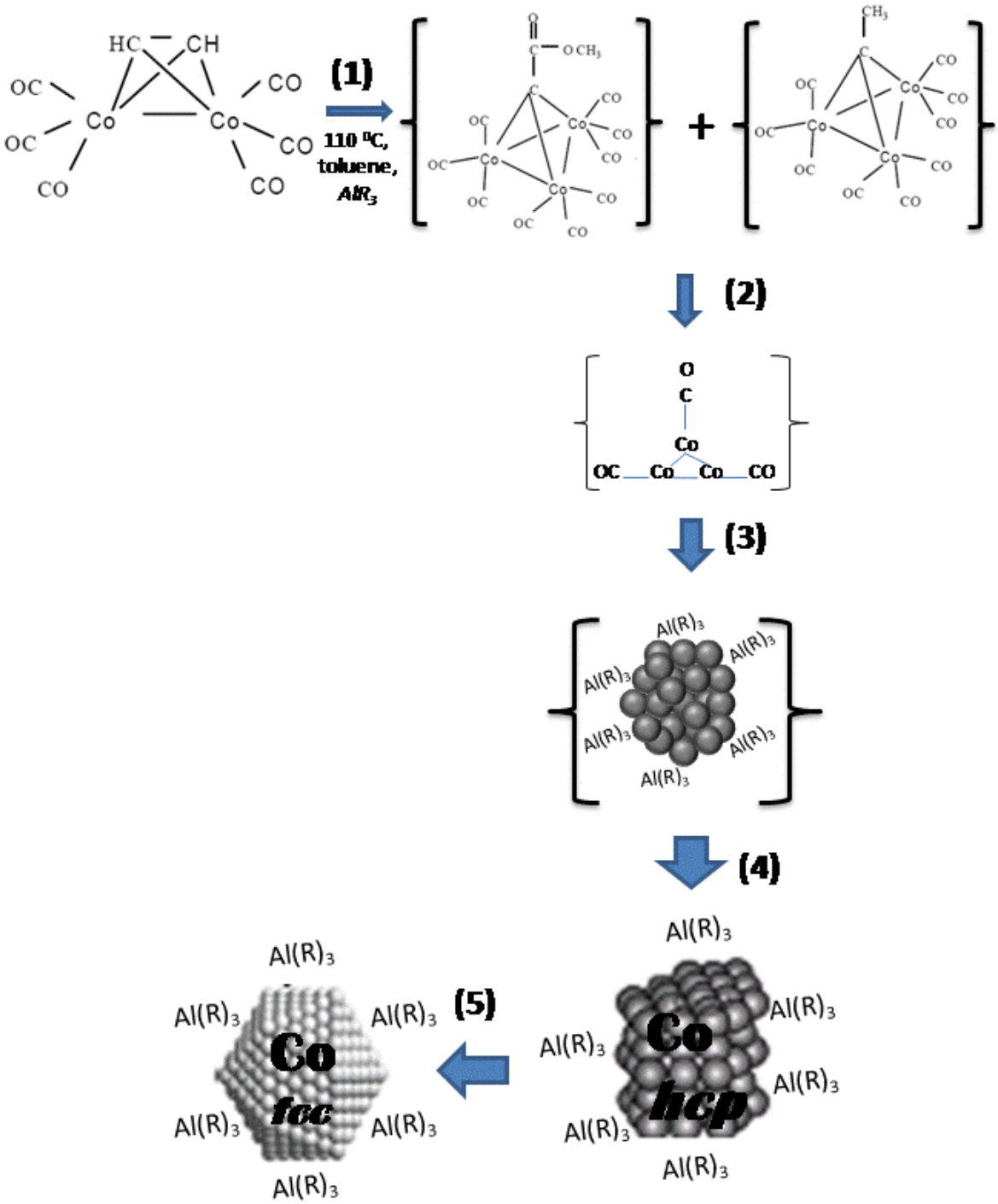

Figure 6.30 Scheme of Co nanoparticle formation from the decomposition of the ADH organometalic complex in the presence of aluminum tryoctal $Al(R)_3$.

6.3 Conclusions

The investigation of the formation of Co nanoparticle via the decomposition of two organometallic precursors the DCO and ADH in the presence of trioctal aluminum shows evidence of reaction pathways very different from both the atom based La Mer model and the autocatalytic surface growth model.

Comparing the time-dependent XAS analysis of Co nanoparticle formation from the DCO and ADH precursors, it is clear that cobalt nanoparticle formation follows generally accepted nucleation and growth stages albeit strongly influenced by precursors and their intermediates. The time-dependent EXAFS analysis identified the loss of carbonyl ligands during the nucleation stage. In the DCO case the results suggest the decomposition of $Co_2(CO)_8$ into the $Co_4(CO)_{12}$ intermediate organometallic complex within the 2 minutes and followed by nucleation of $Co_2(CO)_5$ metallic species after ~ 30 minutes of the synthesis. Whereas in the ADH synthesis, $[(Co_2(\mu\text{-}HC{\equiv}CH)(CO)_6]$ is decomposed into the $[Co_3(CO)_9CCOOCH_3]$ and $[Co_3(CO)_9CCH_3]$ intermediates within ~10 minutes and through gradual decarbonylation followed by the nucleation of $Co_3(CO)_3$ metallic species after ~1hour of the synthesis. Therefore the differences in the decomposition rates are observed even prior to the nucleation. Different decomposition rates as well as different intermediates of the DCO and ADH lead to different concentrations and sizes of initial Co nuclei formed, higher rate of the decomposition of the DCO lead to a larger number of smaller nuclei, while slower decomposition rate of the ADH gives rise to a smaller number but nuclei of bigger size. The size of initially formed particles observed after 3 hours of the ADH synthesis is found to be 4.49 ± 0.09 nm compare to 1.78 ± 0.01 nm of the DCO synthesis.

In both cases there is lack of spectroscopic eveidence for isolated Co^0_m clusters as initial nuclei. Instead, data support the hypothesis that the critical nucleus is composed of metal atoms coordinated with ligands in the form of $Co_n(CO)_m$ where n=2 or 3, m is between 3 and 5.

Growth phase consist of diffusive agglomeration of those initially formed nuclei. Even so the nucleation of the ADH particles started after a longer time compared to the DCO particles the growth phase in both cases is completed after ~9 hours of the synthesis.

The observed decrease of the particles size at the end of the syntheses unlike to the Ostwald ripening is not completely understood. Also, the surface modification of the nanoparticles from the DCO precursor starting after 9 hours of the synthesis and resulting in a CoO-like shell formation cannot be explained at the moment. In the case of the DCO synthesis, during each time interval, a presence of a light backscatterer, such as O or C, coordinated to the cobalt atoms was observed, whereas nanoparticles obtained from the ADH precursor were mostly free from any oxide impurities at every stage of the reaction. Obviously, already at the very early stages of the reaction, surfactant-effect, precursor and its intermediates should be considered simultaneously in order to understand the reaction pathway of cobalt nanopaticle formation and nanoparticle formation in general.

Besides, both the reaction time as well as nature of the precursor had an influence not only on the size, size distribution and crystal structure but also magnetic properties of the cobalt nanoparticles obtained. Therefore another conclusion of this investigation from application point

of view indicates that understanding of the reaction pathway of cobalt nanopaticle formations helps in identifying the right time of the reaction and nature of the precursor in order to obtain nanoparticles of desired properties.

Chapter 7 "In-situ" investigation of Co nanoparticle formation by spatially-resolved X-ray spectroscopy

7.1 Microfluidic system – as a platform for "in situ" investigation

Commonly applied techniques to follow an ongoing reaction "in situ" are the energy dispersive spectroscopy (EDS) and Quick-EXAFS (QEXAFS). The QEXAFS technique[71] allows an EXAFS spectrum to be recorded in a short period of time (50-100 s). The scan time is reduced by moving the monochromator at a constant angular speed and recording the data "on the fly" (each absorption value is integrated for typically 0.01-0.05 s), therefore eliminating the overhead time associated with moving the monochromator on a step-by-step basis. Obviously, the quality in terms of signal to noise is less for very quick scans, but is usually satisfactory to follow reactions in situ. A detailed study of nickel formate dihydrate has been used by Edwards *et al.*[72] to investigate the relationship between monochromator scan speed, integration time and spectral quality in QXAFS spectra. This has shown that good quality XANES spectra can be obtained in *ca*. 4 s, and that EXAFS data collected in either 83 or 33 s is in good agreement with data collected in a conventional step-scan method over a period of 32 min, but that the EXAFS data obtained in 16 s was severely degraded. In the EDS technique[73] a bent triangular single crystal serves as a dispersive monochromator and a photodiode array as a detector. The examples of energy dispersive XAFS (DEXAFS) and QEXAFS measurements for the time-resolved experiment were discussed in Chapter 5.[50,51]

However, these techniques (QEXAFS and EDS) require significant integrations time per energy step and per spectrum, respectively, because of the normally low concentration of the "active" components in the reaction chamber. Thus, it is not possible to use the full potential of these techniques regarding their time resolution.

Also there are drawbacks of traditional batch process for "in situ" characterization. Even when reducing the volume for a given reaction, there are always inhomogeneities in the chemical environment, pressure, temperature and concentration of various components across the beaker, particularly during injection of reagents.

In recent years, considerable progress has been made in the development of microfluidic systems. "Microfluidics" is the term that is used to describe flow in devices having dimensions ranging from millimetres to micrometres and capable of handling volumes of fluid in the range of nano- to microlitres (10^{-9} -10^{-6} l). Interest in miniaturizing is that physical processes are easy to control when instrumental dimensions are reduced to the micro scale. On these length scales, laminar flow and high heat and mass transfer rates can be exploited to exercise superior control over fluid, mass, and energy transport. Because of the laminar flow, diffusion length scales are controlled by channel geometry, permitting more control of reagent mixing conditions.[74]

Microfluidic system can be configured, so that multiple process steps and parallel reactions can potentially be integrated on a single chip of individually addressable microchannels and reservoirs.

There are a number of fields that share an interest in this area: analytical chemistry,[75] high-throughput synthesis,[76] microbiological analysis systems[77] and applications of the 'lab-on-a-chip' concept.[78]

Recently, several researchers have explored also the use of microreactors in the production of nanoparticles of: copper,[79] palladium,[80] silver[81] and gold.[82] Particles of well-defined size and shape were synthesized directly without use of any posttreatment (such as centrifugation, sonication, or precipitation).

In this section, we demonstrate spatially resolved monitoring of Co NP synthesis in a continuous-flow microfluidic reactor. The microfluidic system uses the flow of a fluid to linearly transform space (length of channel) into time (reaction time). For a chemical reaction, this transformation is simple: a solution of reagent A and a solution of reagent B are injected as steady streams into a microfluidic channel and at the initial point d=0 the reaction between them begins (t=0). Simply speaking, as the reaction mixture is transported by the fluid stream at a constant velocity U, every spatial point d corresponds to a time point t, the reaction time, where t=d/U (Figure 7.1).

If the reactions are accompanied by an optical signal (e.g. changes in fluorescence or absorption), time-resolved measurements of the reaction can be obtained from spatially resolved spectra. Therefore the combination of a microfluidic system for synthesis of nanoparticles and spatially-resolved X-ray absorption spectroscopy is a useful tool for "in situ" investigation of the reaction pathway. An entire time course of a chemical reaction can be investigated with millisecond resolution by analyzing fluorescence spectra taken at different points along the channel. Because the flows are steady this spectrum does not have to be time-resolved and can be obtained with long integration time for a fluorescence detector. Also, steady continuous flow of the microreactor inherently improves reproducibility of the synthesis.

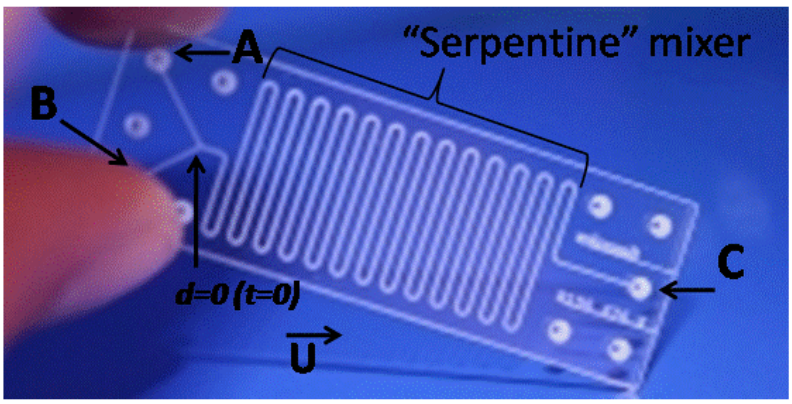

Figure 7.1 Microfluidic reactor for the synthesis of nanoparticles.

7.2 Time resolution

The reaction times that are required for the synthesis of nanoparticles of a given size in the microreactor are determined by reaction kinetics (material itself, solvent, surfactant, reducing agent, concentration of the materials) and diffusion factors such as mixing efficiency. As there are a broad range of parameters to control residence-time in the reactor channels (size and length

of the channels, pressure, passive mixtures etc.) the design of the microchannel can be adjusted to the requirement of the corresponding reaction and the time resolution that will allow observing even short lived reaction intermediates.

The residence time for the here used reactor was measured by timing painted liquid as it traveled through the reactor. This experiment was done several times and an averaged residence time of 50 seconds was obtained. With a channel length of 10 cm, a residence time of 50 seconds and a focused beam height of 50 µm, the time resolution of this system about 2 ms is obtained. That is at least a factor of 100 better than to previous DEXAFS or QEXAFS studies. However, one has to keep in mind that the microreactor that was used for this experiment is operated in the laminar flow regime. Thus a parabolic velocity profile is established over the cross-section with fluid velocity zero at channel walls and maximum at the center. This yields a residence-time distribution that may cause significant variation in the yield, efficiency and product distribution.

7.3 Experiment

Flexible PTFE (Polytetrafluorethylen) tubes[83] (inner diameter: 0.8 mm) were fitted into the fluid ports A, B and C (Figure 7.1) and sealed permanently using hot melt glue *(Bostik® Thermogrip® 0140 glue stick).*[84] This method of interconnection was used because the microreactor had to be placed in the X-ray chamber surrounded by electrical circuitry and the possibility of accidental leaks had to be avoided. Micro-dispensing, solenoid actuated pumps (*Bio-chem valve inc*., 120SP 24 Vdc)[85] were used for filling the reactor with reagent solutions. A slow continuous flow rate on the order of 1.3µl/min was achieved.

Through the two inlets (Figure 7.1 A and B) the flow of cobalt acetate and SB12 surfactant is combined with the flow of reducing agent (at the point d) and followed by a mixing in a "serpentine" section toward the outlet (C). The reagents and final product of the reactor were strictly kept under nitrogen flow. The experimental set-up (during the trials outside the hutch) is shown in Figure 7.2.

XANES spectra were measured at four points along the channel (Figure 7.3): I- at the mixing point, II- after 0.5 sec. of the reaction, III- after 5 sec. of the reaction and IV- at the end of the channel that is ~50 sec. of the reaction. The so chosen time points allowed detailed monitoring of the reaction, especially at the nucleation stage and real-time product identification of the synthesis.

The XANES spectra were scanned within -20; +40; +80 eV intervals relative to the Co K-edge and step width 0.4, 1 eV per respective interval with integration time 3 sec. per step. Reproducibility was validated in triplicate experiments. After every experiment the microreactor was washed with a dilute solution of nitric acid to get rid of residuals and absorbates from the walls of the channels. This is a limitation of the apparatus. Particles nucleate and deposit on the channel walls, leading to clogging and unstable reactor conditions, particularly in narrow channels. The microreactor could be operated continuously for no more than 15 minutes, so the XANES scan parameters were adjusted to meet that limitation. Another limitation was unwittingly set by type of connecting tubes to the microfluidic ports. The glue, that was used has "fair" chemical resistance to acids, therefore the microreactor could be used for no more than 3 times. Future designs should accommodate better connectors.

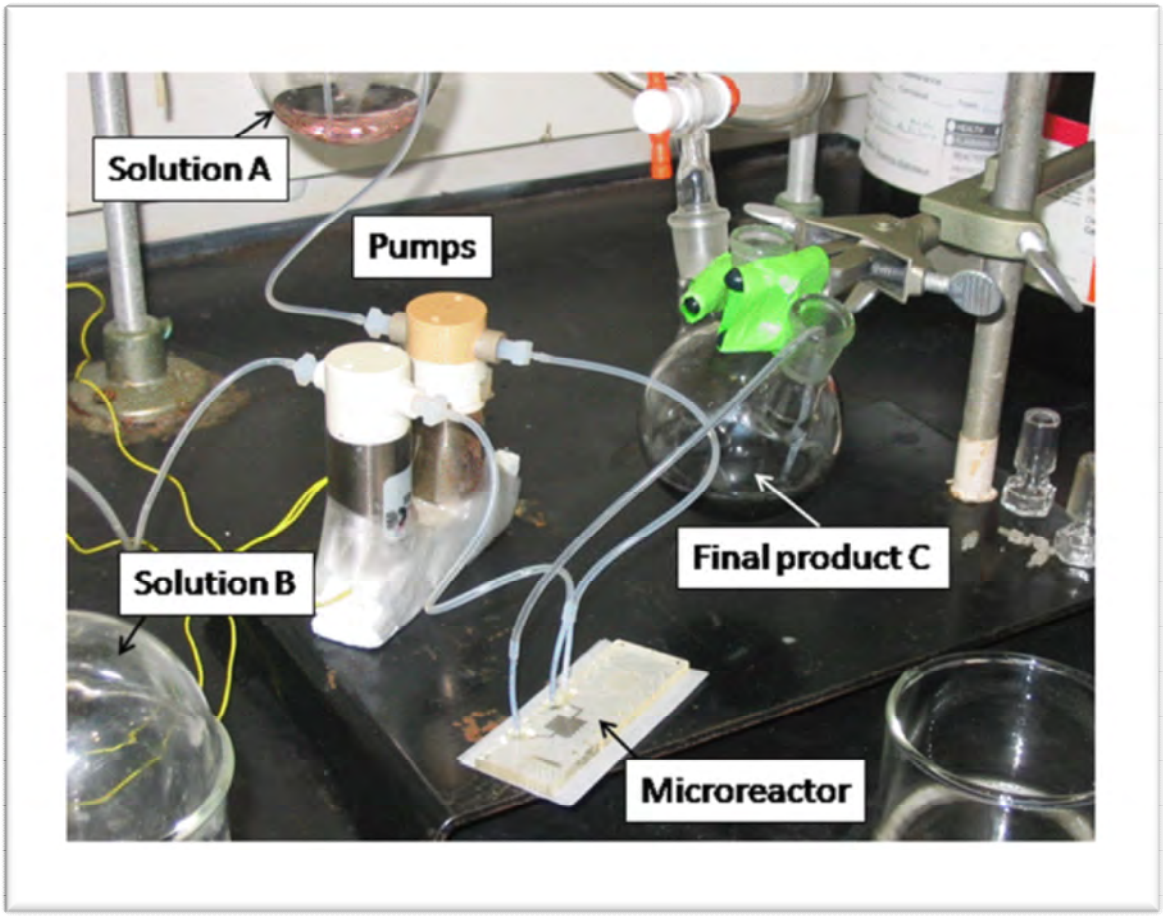

Figure 7.2 The experimental set up for microfuidic synthesis.
Solution A is Co acetate with SB12; Solution B is a reducing agent; Final product C is Co nanoparticles dispersed in nanopure water.

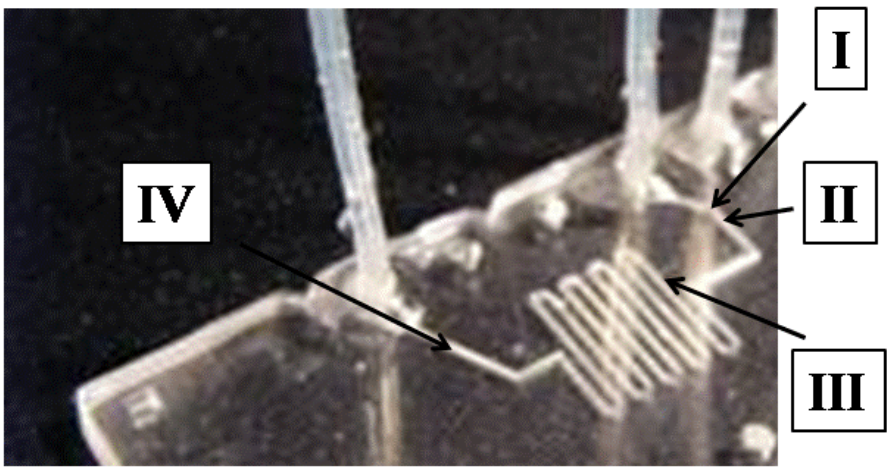

Figure 7.3 The picture of microfluidic reactor with the points marked (I-IV) at which XANES spectra were collected.

7.4 "In situ" XANES analysis

Co K-edge XANES spectra recorded at the very early stages of the reaction (that is at the mixing point (d=0, t=0) and 0.5 sec after reagents are brought together) in comparison with the Co foil and precursor reference spectra are shown in Figure 7.4.

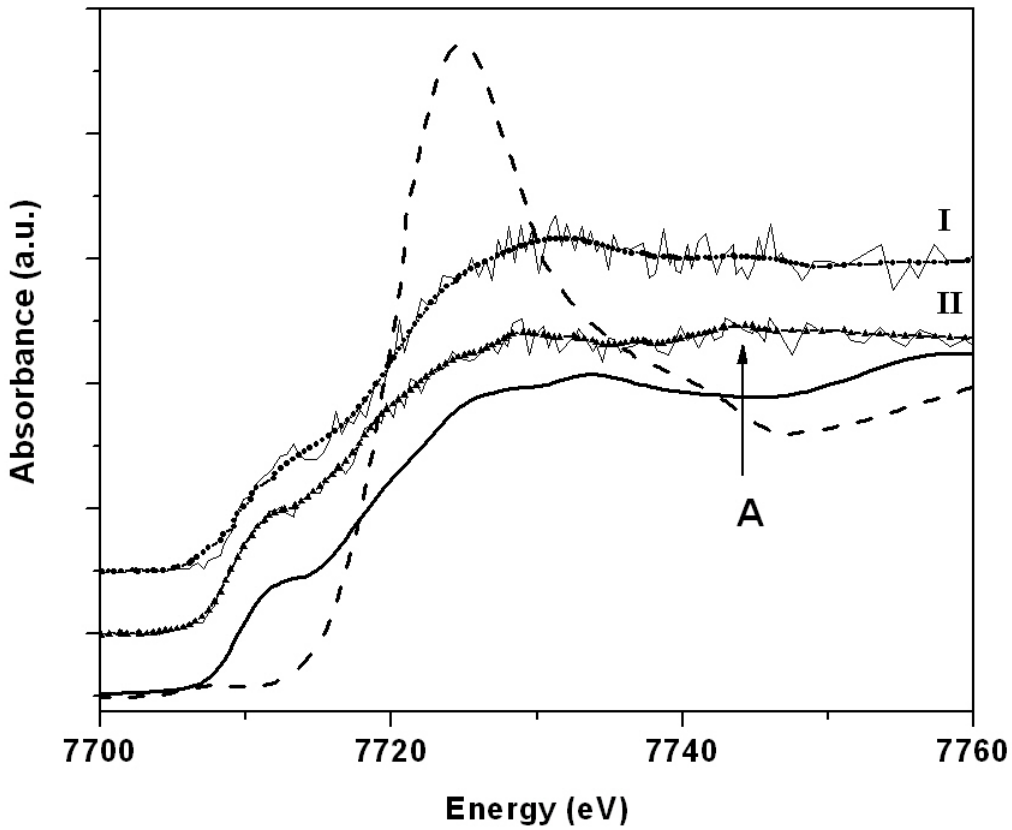

Figure 7.4 Co K-edge XANES spectra from top to bottom: taken at the mixing point I, at the point II (raw data & smoothed with 4 points FFT filter) with Co acetate (dash black) and Co foil (solid black) spectra for comparison.

Looking at the spectra it is obvious that the first steps of the reaction are extremely fast. Both spectra at the point I and II with half a second time difference have different shape resonances. From the comparison of spectra at the mixing point I with those of the precursor one can see that as soon as reagents are brought together there is no evidence for unreacted precursor complex left, because the spectrum becomes absolutely different from that of precursor. This is expected because of their redox potentials most of the transition metals are reduced by sodium borohydrate instantaneously (10-th of ms). On the other hand the spectrum does not look like the atomic spectrum of Co atoms. The atomic spectra of transition metals are dominated by a prominent line at threshold which precedes a smooth continuum extending to higher energies.[86] For comparison in Figure 7.5 example of Mn atomic 1*s* absorption spectra (experimental and calculated theoretically) are shown. Therefore free Co atoms are not observed at this stage, as the spectrum does not show the typical resonance of atomic transition metals K-shell spectra.

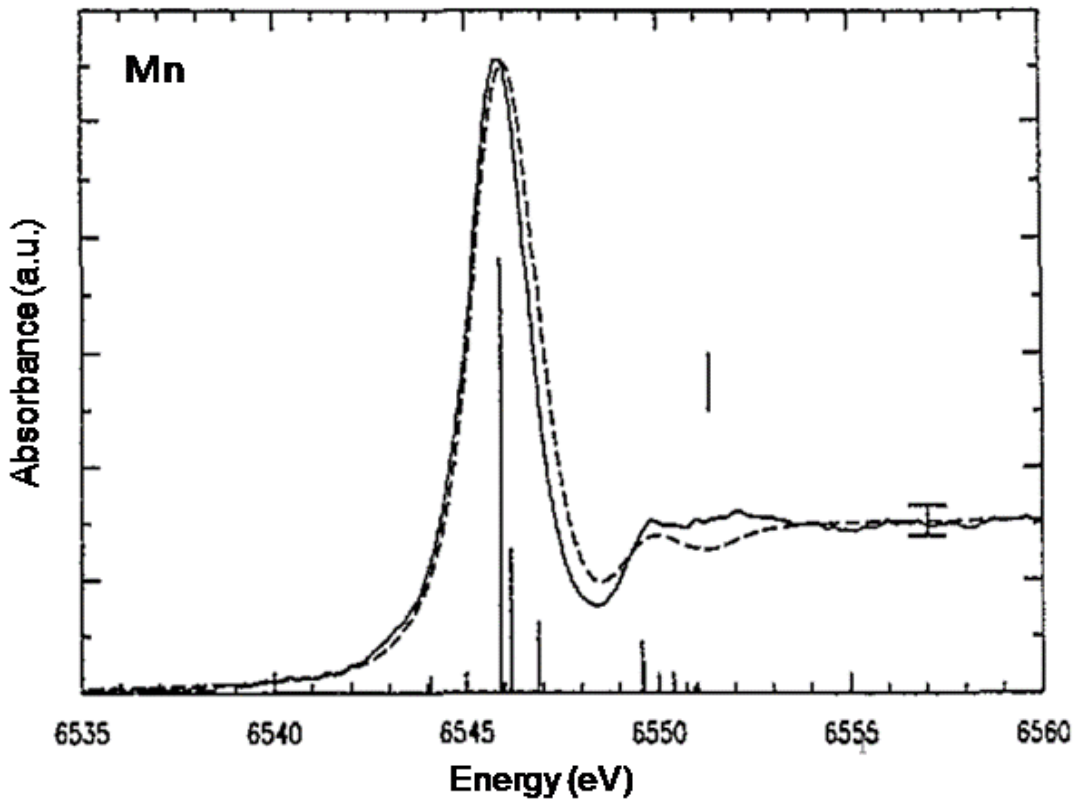

Figure 7.5 1*s* absorption spectra of atomic Manganese determined experimentally (solid black line) and calculated theoretically (dashed black line).[86]

Also from the comparison to the Co foil spectrum we can conclude that at this point of time the electronic and geometric structure around the absorbing atom are different from bulk Co. Even so there is pronounced pre-edge intensity comparable to that of Co foil indicating that the majority of Co is reduced to a metallic form with valency zero the shape resonance over the edge is different from the Co foil. A slight increase of the WL intensity as compared to Co foil and additional maximum (A) between 7740-7750 eV are observed.

As the reaction proceeds, after 0.5 sec. another stage of the Co nanoparticle formation is already observed. The energy position of the first inflection point is similar to those of previous spectra at point I and of Co foil (7709 eV), see Figure 7.6. The pre-edge gained more intensity, whereas the WL intensity decreased. That is again an indicator of changes in the vicinity of the absorbing atom and its electronic structure. To analyze in detail what has happened to cobalt ions from the Co acetate complex, it is necessary to think about possible reference compounds and therefore about the reaction of cobalt acetate and sodium borohydtrate.

The borohydride reduction chemistry is quite complex and the nature of the products depends on the reaction conditions.[87] Klabunde et. al.[87b] has shown that rapid mixing of cobalt ions and borohydrides under aerobic conditions yields metal particles and cobalt borides under anaerobic conditions. Furthermore, the solvent used in producing the particles plays an important role in formation of the final product. In fact, the mechanism differs markedly between aqueous and non-aqueous solution.

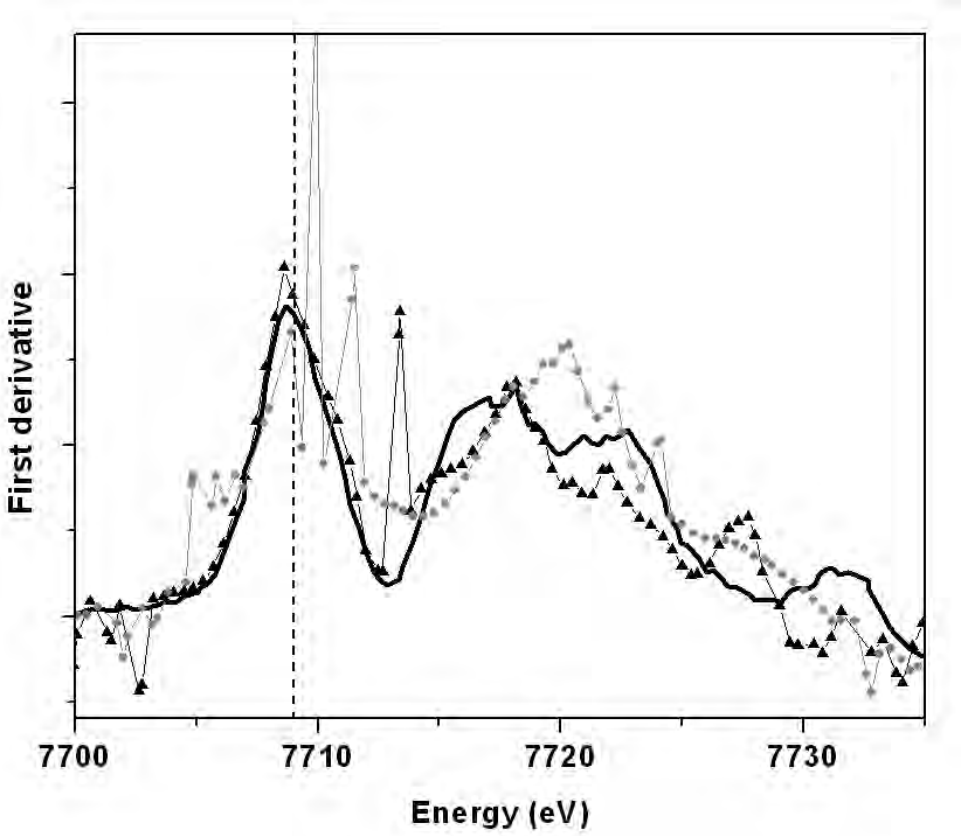

Figure 7.6 First derivative of I (solid line with ● symbol, gray), II (solid line with ▲symbol, black) and Co foil (solid black) spectra. The energy position of Co K edge 7709 is marked with dashed line.

In aqueous solution, black precipitates of metal boride particles are formed as follows[87b]:

$$2Co^{+2} + 4BH_4^- + 9H_2O \rightarrow Co_2B + 12.5H_2 + 3B(OH)_3$$

In non-aqueous solution, or aqueous solution with a surfactant, cobalt metal particles are formed. This has been explained by the fact that the non-aqueous solvent or surfactant acts as a ligand, *L*:

$$Co^{2+} + 2NaBH_4 + nL \rightarrow (L)_nCo(BH_4)_2 + 2Na^+$$

The mechanism of cobalt nanoparticles formation is not obvious:

$$(L)_nCo(BH_4)_2 \rightarrow (L)_nCo + H_2 + B_2H_6 \text{ or}$$

$$(L)_nCo(BH_4)_2 \rightarrow Co + H_2 + B_2H_6 + nL$$

Therefore, to gain a better understanding of the changes observed in the electronic and geometric structures of Co ions in the above spectra and consequently about the nucleation process it is reasonable to make a comparison with Co borides.

Figure 7.7 shows Co K edge XANES spectra with variation of B content in the cobalt borides compounds in comparison with the Co foil spectrum.[88]

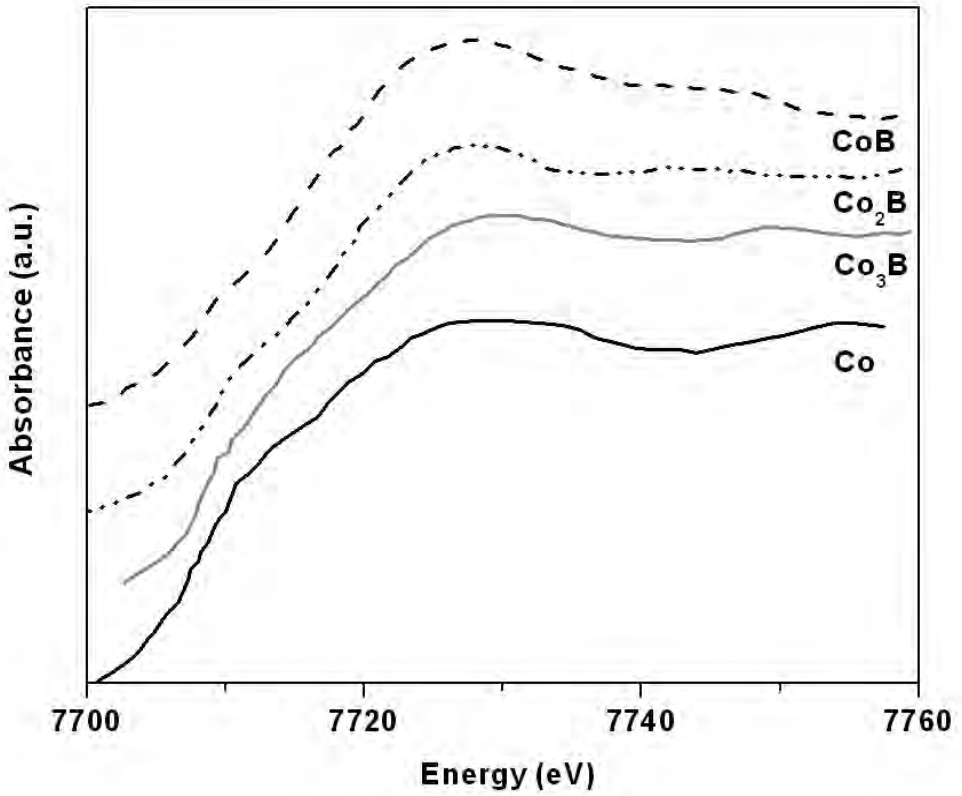

Figure 7.7 Co K-edge XANES spectra from top to bottom: CoB (dash black), Co_2B (dash dot dot black), Co_3B (solid gray) and Co foil (solid black).[88]

In all borides formed, the boron atoms are covalently bound to cobalt atoms therefore there is a redistribution of valence-active electrons of both partners among bonds of three different types: the metallic Co-Co bond, the covalent-ionic Co-B bond, and the covalent B-B bond. These changes are reflected in the increase of the WL intensity and decrease of the pre-edge compare to the Co foil upon Co borides formation.

Comparison of spectra taken at points I and II with Co_2B, CoB compounds and Co foil as reference spectra is shown in Figure 7.8. In both spectra I and II a slight increase of the WL intensity and the appearance of an additional shape resonance (A) between 7740-7750 eV are similar to the spectral features of Co borides reference spectra. The intensity ratio of the WL and the shape resonance (A) and the decreased pre-edge in the spectrum taken at the point I are more similar to the CoB reference spectrum. The spectrum taken at point II is more similar to the Co_2B reference spectrum.

Therefore in situ monitoring of the reaction did not show the formation of bare Co_m complexes, instead B atoms bond to Co ions, thereby stabilizing them and lowering the free energy of cluster formation.[89] Thus complexes such as Co_mB (m=1 or 2) should be considered as first stable nuclei.

Next spectrum taken at the point III that is a first curl of the serpentine mixer and ~5 sec. of the reaction is present in Figure 7.9(a). At a first look we can conclude, that this spectrum possesses

an outstanding spectral feature that is hardly any fine structure on the continuum, and it can be interpreted as a spectrum of a very small Co clusters (3 or 4 atoms).

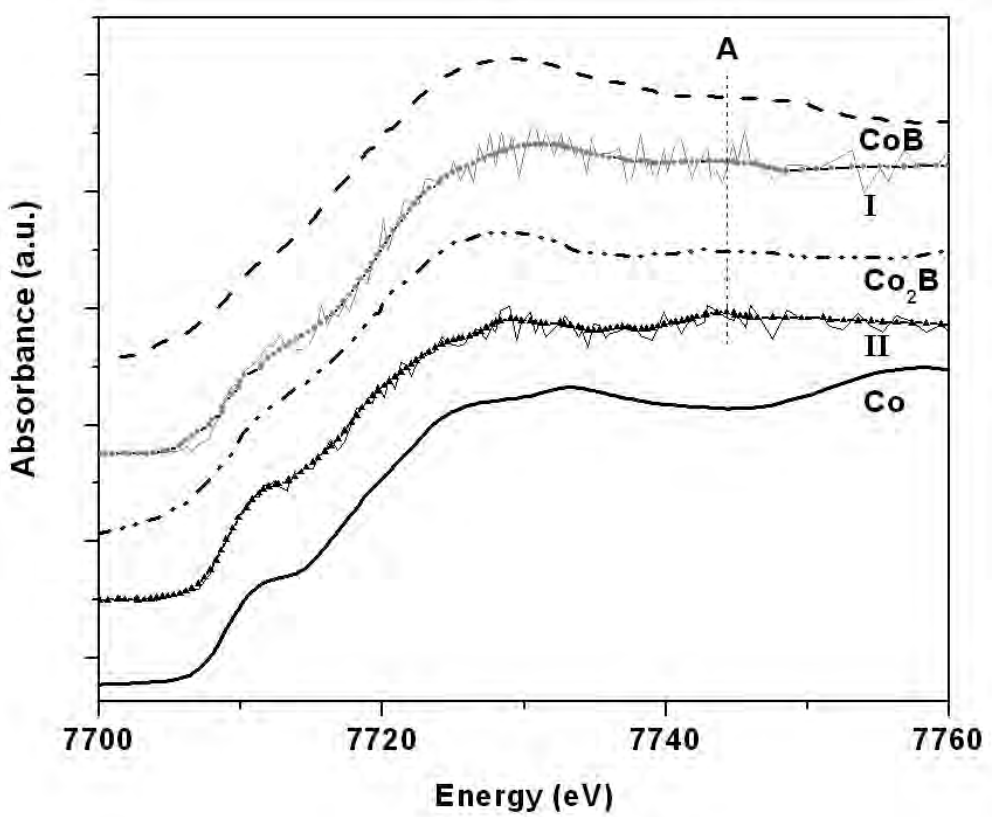

Figure 7.8 Co K-edge XANES spectra taken at the point I, at the point II (raw data & smoothed with 4 points FFT filter) in comparison with Co_2B (dash dot dot black)[88] and Co foil spectra (solid black).

The Co K-edge XANES spectrum taken at the final point of the microreactor IV that is ~50 sec. of the reaction in comparison with reference spectrum of the Co foil is shown in Figure 7.9 (b). Even though the fine structure of the spectrum is somewhat "washed out" good agreement with the Co foil spectra is achieved with respect to the position and the intensity of the shape resonance as well as the position of the first inflection point, which is clearly seen in the first derivatives (Figure 7.10). The differences in the WL maximum position may be attributed to the formation of the fcc phase (or mixture fcc and hcp), where the amplitude of the first peak is higher than the second.

Finally, particles were collected at the exit of the microreactor. Powder sample was prepared and XANES spectra in the transmission mode were recorded. In Figure 7.11 a comparison of the in-situ XANES spectrum taken at the end of the microreactor (point IV) with the microreactor final product is present. Similarity of spectral features of the final product and the spectrum measured in situ at the point IV is clearly visible. The difference in the pre-edge intensity may be attributed to particles of different size. The final product was collected into the flask for ~18 minutes without quenching (that is one in situ XANES scan duration) therefore Ostwald ripening could take place during that time if small Co clusters are remained available in the solution.

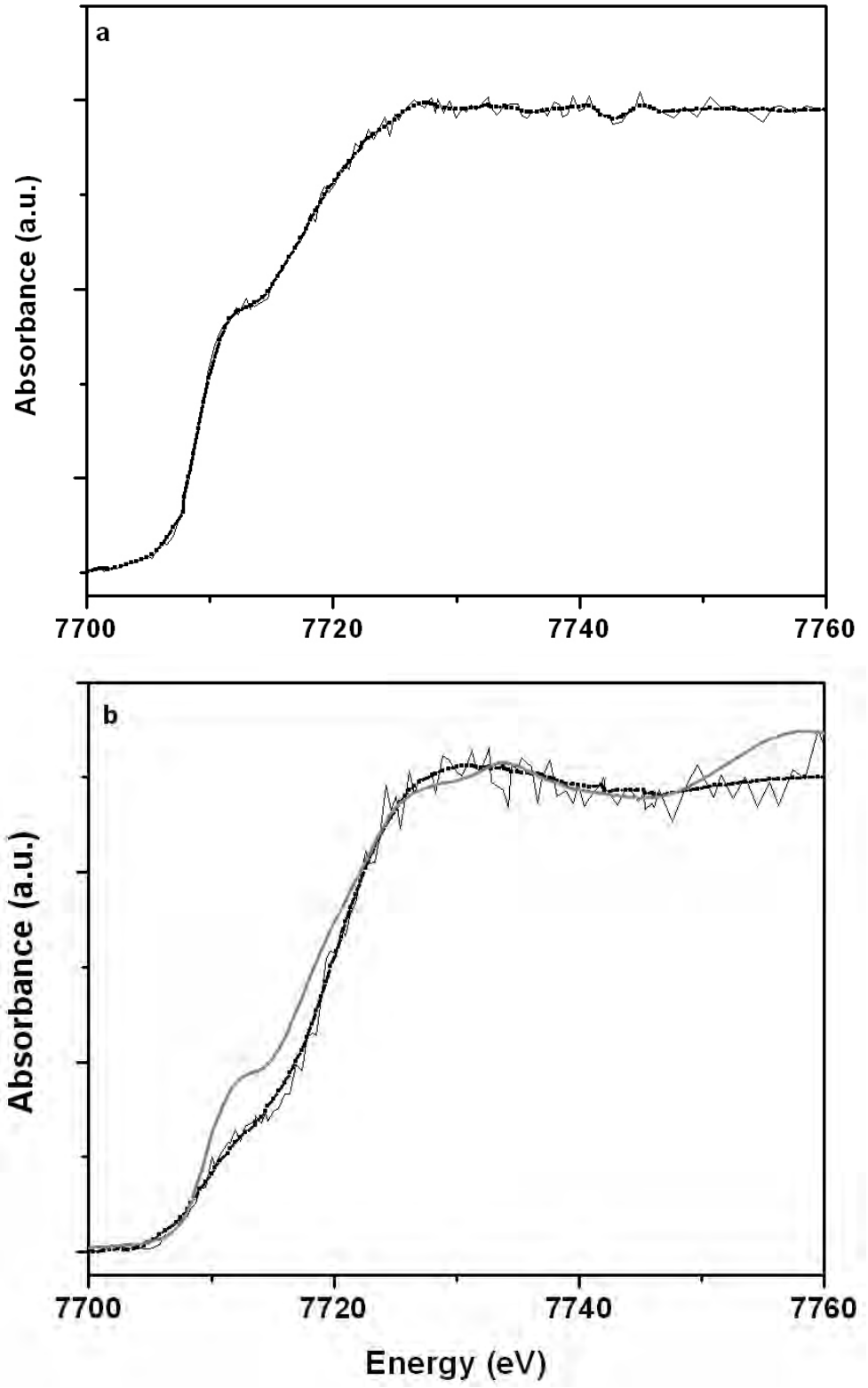

Figure 7.9 Co K-edge XANES spectra: a) taken at the point III, b) at the point IV (raw data & smoothed with 4 points FFT filter; line with ■ symbol black) and Co foil (solid gray).

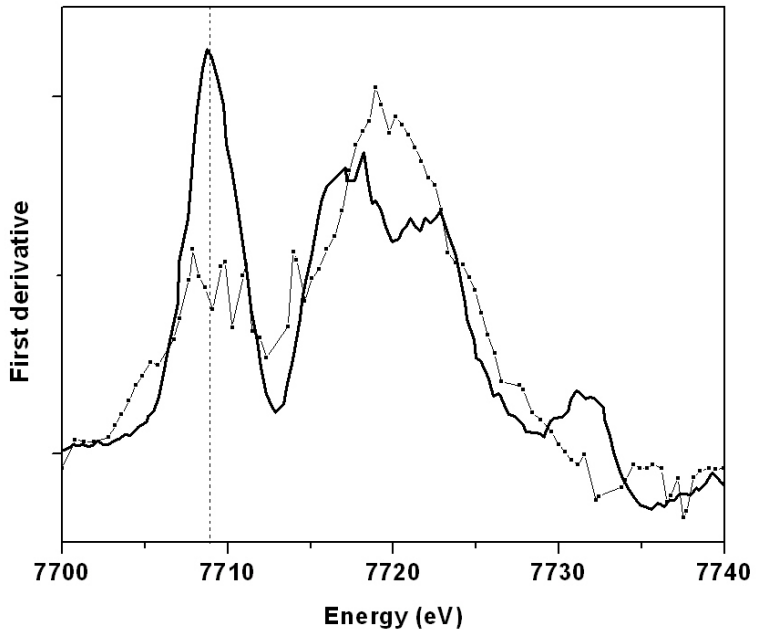

Figure 7.10 First derivative of spectra taken at the point IV (solid line with ■ symbol, black) and Co foil (solid black). The energy position of Co K edge 7709 is marked with dashed line.

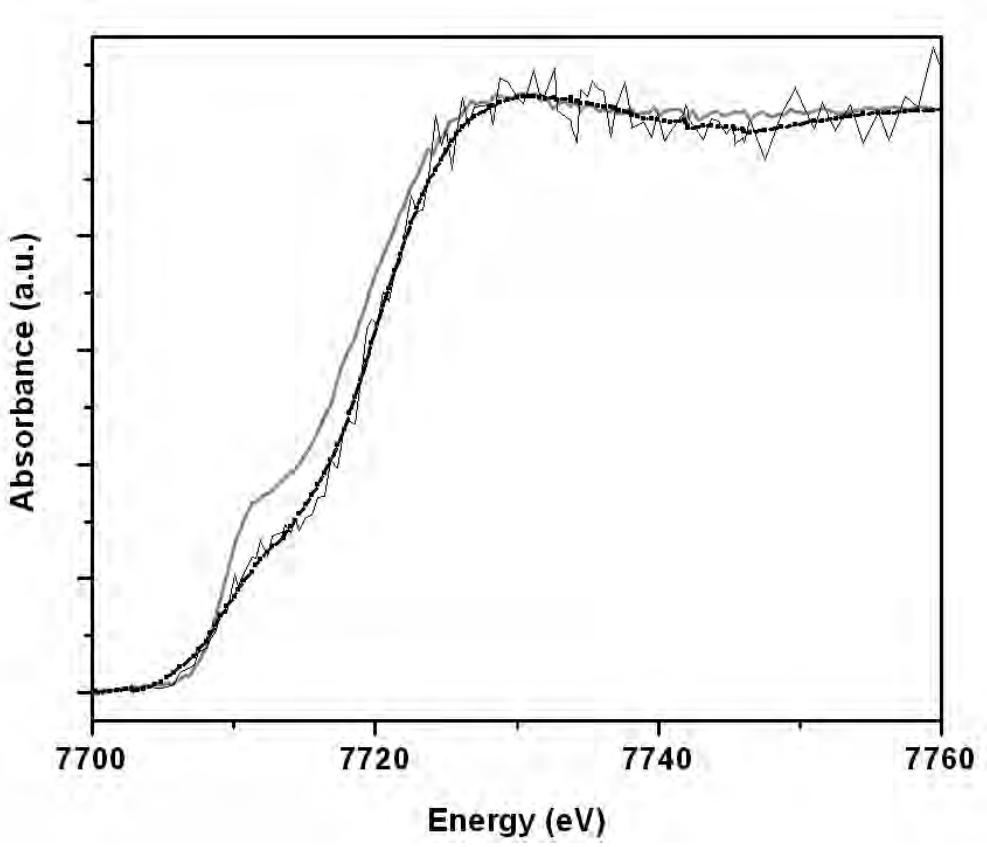

Figure 7.11 Co K-edge XANES spectra taken at the point IV (raw data & smoothed with 4 points FFT filter; line with ■ symbol black), in comparison with the microreactor final product (solid gray).

From the comparison of microreactor Co nanoparticles with aluminumorganics stabilized nanoparticles obtained wet chemically via thermolysis, described in Chapter 6 it is in principle possible to define the size, surfactant and specific phase effects. In Figure 7.12 Co K-edge XANES spectra of the microreactor final product, "ADH 9h", "ADH 18h" samples and FEFF8 calculated spectra of the hcp and fcc phases are shown. From the above analysis (Chapter 6) the "ADH 9h" spectrum with particles size of about 5.00 ± 0.05 nm was assigned to the hcp phase. For the "ADH 18h" spectrum synthesis were continued for 9 hours longer under the same conditions and that led not only to the unexpected change in the particle size (now 4.56 ± 0.21 nm) but also to a change of the crystallographic phase; this spectrum resembles the fcc phase.

The microreactor final product spectrum has a fine structure similar to the "ADH 18h" spectrum, but the pre-edge intensity and therefore particles size are more close to the "ADH 9h" sample. The differences observed in the WL region correspond to a different electronic structure and attributed to the different surfactants used: aluminumorganics ($Al(R)_3$) in the thermolysis and SB12 in the microfluidic reaction. Therefore Co core interact with the different environment. In the case of microfluidic reaction the interaction between SB12 surfactant and Co core is most probably presented through the Co-S bond. However, to verify this interaction one would need a S K-edge XANES spectrum, which is unfortunately missing in this work. If there are not too much of S atoms at the surface of the nanoparticle, then it is much harder to "see" this interaction from the Co K-edge. As an example where it was possible XANES analysis of Co nanoparticles peptized by L-cysteine ethyl ester can be found in Appendix B. There Co-S bond led to drastic changes in the electronic structure, such as chemical shift of the Co K-edge towards slightly higher energy and increase in the energy position of the shape resonance at 7758.5 eV, which are not observed in the current case. The first inflection point and the position of the shape resonance over the edge are extremely similar to the Co foil (see Figure 7.12, Figure 7.13). Nevertheless, SB12 like $Al(R)_3$ surfactant stabilize Co nanoparticles against agglomeration, thus some amount of SB12 should be present in the surface of the nanoparticles. Stabilization with SB12 against oxidation for microreactor nanoparticles does not hold as well as with $Al(R)_3$ in the thermolysis. The microreactor nanoparticles are highly air sensitive.

For comparison, the same reaction was carried out using a batch process. The reactant solutions had the same composition as used in the microreactor. XANES spectra of both final products (microreactor and batch reaction) are shown in Figure 7.14(a). The spectra are similar. The different pre-edge intensity is attributed to the different particles sizes. The microreactor final product was collected in about 18 minutes without quenching the solution; therefore the Ostwald ripening could take place. Whereas, the batch process was carried out for 50 seconds and then immediately quenched. This was done to get comparable reference to the microfluidic reaction where residence time is ~50 seconds. The similarity of the batch Co nanoparticles to the in situ spectrum taken at the point IV of the microreactor is clearly seen in Figure 7.14(b).

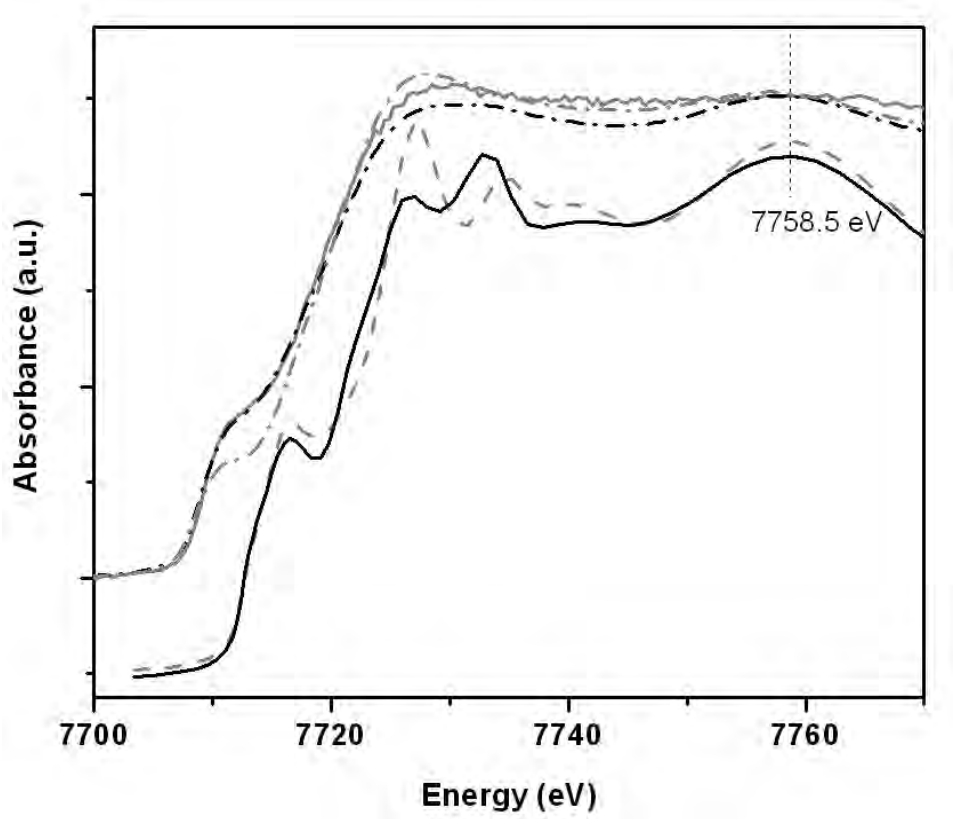

Figure 7.12 Co K-edge XANES spectra of microreactor final product (solid gray), "ADH 9h" (dash dot black), "ADH 18h" (dash dot gray) and FEFF8 calculated spectra of fcc (dash gray) and hcp (solid black) phases.

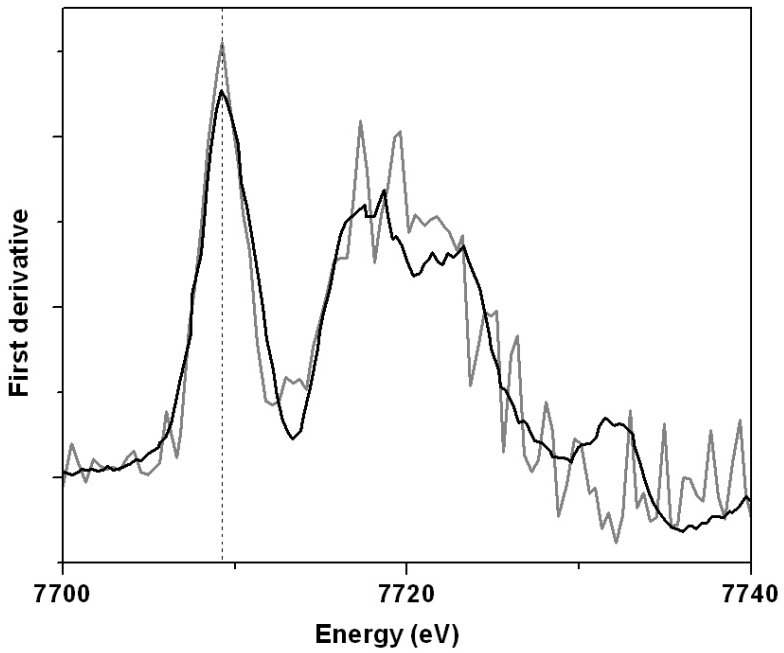

Figure 7.13 First derivative of microreactor final product (solid gray) and Co foil (solid black). The energy position of Co K edge 7709 is marked with dashed line.

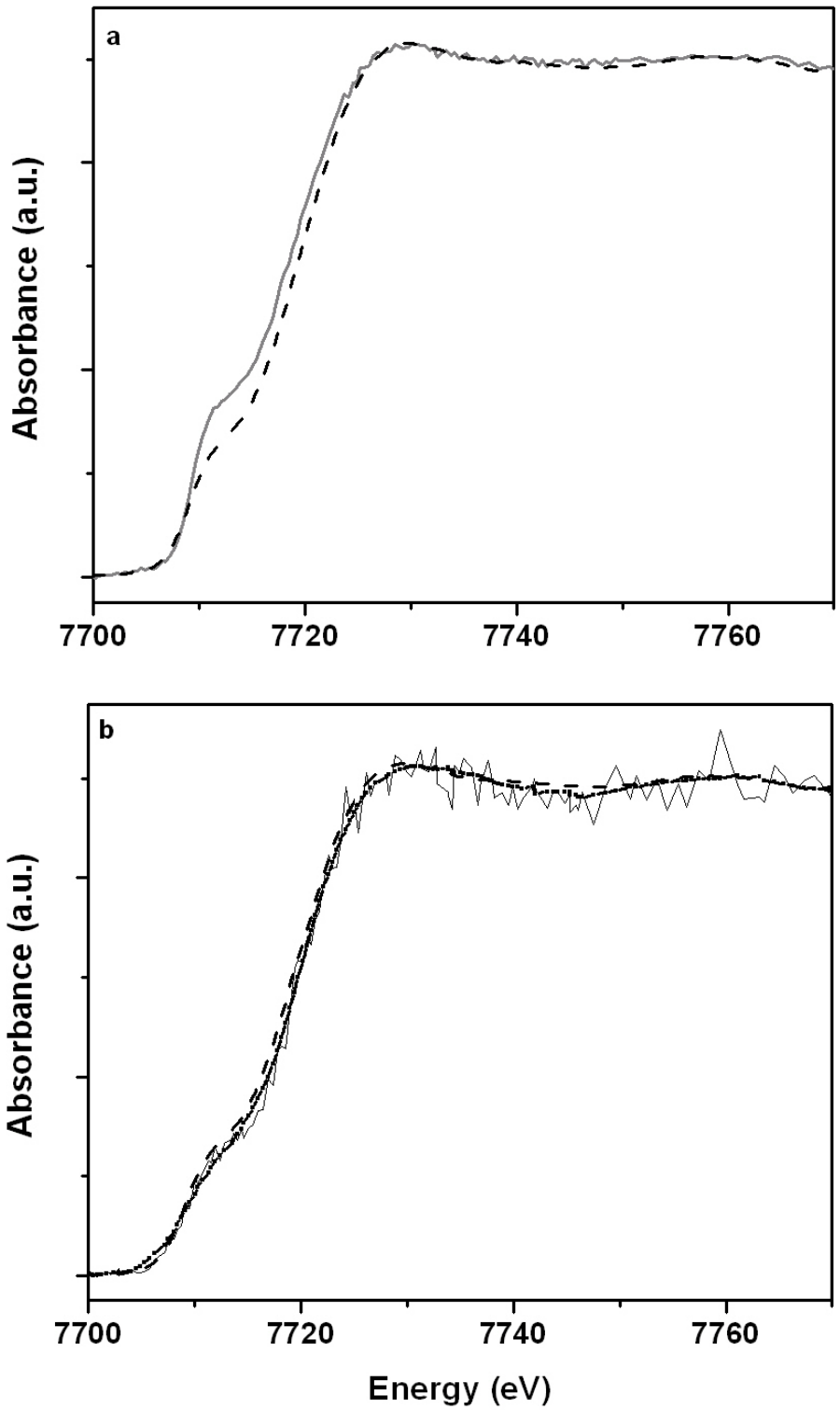

Figure 7.14 Co K-edge XANES spectra of Co nanoparticles via batch process (dash black) in comparison with a) microreactor final product (solid gray) and b) in situ spectrum taken at the point IV (raw data & smoothed with 4 points FFT filter; line with ■ symbol black)

7.5 Conclusions

The main aim of this work was to study "in situ" the synthesis of Co nanoparticle formation. Here experiments using a microreactor system for wet-chemical synthesis of cobalt nanoparticles in combination with spatially resolved X-ray absorption spectroscopy are presented. In such a system, the entire reaction is spatially resolved in the microreactor. Because the flows in the microreactor are steady, the spectrum does not have to be time-resolved and can be obtained with long integration time.

The microfluidic system that was used is easy to fabricate and operate as it has no active or moving components, and can be controlled simply by varying the rates of fluid flow. Both short (a few seconds) and long (~5 minutes) time scales can be accessed in the same microfluidic device simply by varying the flow velocity.

At the XMP/CAMD microprobe end station with the Kirkpatrick-Baez mirror focusing system, the focused monochromatic radiation of 80x50 μm (horizontal and vertical, respectively) beam spot size was achieved. The so obtained spatially resolved X-ray absorption spectroscopy gives possibility to study the entire time course of a chemical reaction along the microchannel with better than 2 milliseconds time resolution, as time resolution is determined by the vertical size of the X-ray beam.

From the in situ Co K-edge XANES spatially resolved experiments and the subsequent "fingerprint" data analysis, the following results can be summarized:

First of all, it is possible to transfer batch water based synthesis of Co nanoparticles into a microfluidic system where the decomposition of cobalt (II) acetate complex by sodium borohydrate in the presence of SB12 as a surfactant also leads to the formation of Co nanoparticles. That is a good indication towards a future successful scale up process. Both the batch and the microfluidic process lead to similar product- Co nanoparticles with predominantly fcc structure, but in the last case the exact reaction pathway can be understood and thus ability to produce products with desired properties are obtained.

All four spectra taken along the channel are different demonstrating that different stages of the synthesis are observed. Like in the previous chapter, but now with better time-resolution the reaction pathway are very different from the atom based La Mer model as well as the autocatalytic surface growth model. Immediately after the mixing of two streams of reagents formation of Co borides CoB and Co_2B were identified, followed by nucleation of small Co clusters. No evidence for isolated Co atoms was obtained. Instead, data support the hypothesis of Co_2B as a stable nucleus.

The current durability of reactors is determined to ~45 minutes life time (that is 3 reactions for 15 minutes with cleaning of channels after each reaction). To avoid particles deposition on the walls and clogging the channels, and therefore to increase current life time of the reactor developments should be introduced. By longer integration time or multiple experiments, improvement of signal-to-noise levels compared to those of conventional measurements would be obtained. The current work was limited by the number of reactors available.

Nevertheless, the potential of this new technique for fast time resolved in situ investigations of the wet chemical synthesis of Co NP’s formation was clearly demonstrated. In principle, it is also possible to evaluate to what extent the laminar flow in the microchannels affect the spectra, simply by measuring across the channel at a fixed position (=time of the reaction). In general, this technique might be a valuable tool in the investigation of other chemical reactions and processes where miniaturization and time-resolution are important.

Chapter 8 Summary and Conclusions

In this thesis some insight into the process of nanoparticle formation was obtained through XAS. It is evident that this technique is especially suitable for the investigation of nanoparticles as it does not require any long range order and allows separate investigation of each type of atom in a sample. Also it provides information on both electronic and geometric structure.

The systematic characterization of the mechanism of cobalt nanoparticle formation in the course of the thermal decomposition of the DCO and ADH complexes using the time-dependent X- ray absorption spectroscopy revealed evidence of reaction pathways very different from both the atom-based La Mer model and the Watzky and Finsky autocatalytic surface growth model. A more detailed mechanism of what happens during cobalt nanoparticle nucleation and growth was proposed. The mechanism, even so it is not as straightforward as La Mer or Watzky and Finsky 2-step models, is more descriptive of the formation of Co nanoparticles from organometallic precursors.

In the DCO case, the results suggest rapid decomposition of the $Co_2(CO)_8$ organometallic complex into the intermediate $Co_4(CO)_{12}$ organometallic complex. The nucleation process, indicated by shorter metal-metal bond distances compared to those in molecules of organometallic complexes, appeared at ~ 30 min. of the synthesis. The initial nuclei consist of $Co_2(CO)_5$ species, which as seeds give rise to the cobalt nanoparticles. Whereas in the ADH synthesis, $[(Co_2(\mu\text{-}HC{\equiv}CH)(CO)_6]$ complex is decomposed into the $[Co_3(CO)_9CCOOCH_3]$ and $[Co_3(CO)_9CCH_3]$ intermediates, which after ~ 1 hour nucleate as $Co_3(CO)_3$ species. In both cases there is a lack of spectroscopic evidence for isolated Co^0_m clusters as initial nuclei. Instead, data support the hypothesis that the stable nucleus is composed of metal atoms coordinated with ligands in the form of $Co_n(CO)_m$ where n=2-3 and m=3-5, respectively. The growth phase consists of diffusive agglomeration of those initially formed nuclei and is in both cases finished after 9 hours of the synthesis.

The observed decrease of the particles size at the end of the syntheses unlike to the Ostwald ripening is not completely understood. Also, the surface modification of the nanoparticles from the DCO precursor resulting in CoO-like shell formation is difficult to explain. In the case of the DCO synthesis, during each time interval, a presence of a light backscatterer, such as O or C, coordinated to the cobalt atoms was observed, whereas nanoparticles obtained from the ADH precursor were mostly free from any oxide impurities at every stage of the reaction. Obviously already at the very early stages of the reaction, surfactant-effect, precursor and its intermediates should be considered simultaneously in order to understand the reaction pathway of cobalt nanopaticle formation and nanoparticle formation in general.

The process of Co nanoparticle formation was also investigated using a reaction completely different from thermolysis of cobalt carbonyls, namely reduction of Co (II) acetate by sodium borohydrate. Here the combination of a microreactor system and spatially resolved XAS allowed in situ monitoring of the wet chemical synthesis. Where the several steps of the reaction was spatially resolved and the time resolution (better than 2 ms) is determined by the vertical size of the X-ray beam (50 µm).

All four spectra taken along the microchannel differ- demonstrating that different stages of the synthesis are observed. Immediately after the mixing of two streams of reagents- cobalt (II) acetate and SB12 as a surfactant with a sodium borohydrate as a reducing agent- formation of Co borides CoB and Co_2B was identified, followed by the nucleation of small Co clusters. No evidence for isolated Co atoms was obtained.

These results show the potential of this new method using a microreactor for in situ measurements of the reaction pathway and for the structural studies of such class processes where miniaturization and time-resolution are important.

It is clear that the mechanism of cobalt nanoparticle formation depends on reaction conditions, such as precursor, surfactant, solvent and type of reaction (microfluidic or batch). Nevertheless, the following issues can be summarized:

- The critical nucleus is composed of Co atoms/ions coordinated with ligands. Metal atoms/ions, with some of their associated ligands Co_nL_m nucleate and then clusters are reduced to Co (zerovalent) clusters, unlike to the postulated decomposition/reduction to Co^0 atoms followed by nucleation of Co^0 atoms.
- The critical nucleus Co_nL_m has n=2- 3 and m=3-5.
- Ligands are involved in every step of nanocluster formation and not are merely spectators until the nanoclusters are fully formed.

The ultimate aim of any investigation of nanoparticle formation is to develop some general principles, which would make it possible to predict precise reaction pathways leading to the formation of nanoparticles with desired characteristics and properties. The understanding of the kinetics and mechanisms of the formation and growth of nanoparticles is necessary for control of particle size, morphology, composition, and surface characteristics. It is hoped that the present work shed more light on it and assisted in achieving this goal.

Next, I would envision several follow-up experiments. It is clear that in situ investigation of nanoparticle formation is very challenging; I believe that by overcoming the challenges associated with the microchannel clogging and improving signal-to-noise level, EXAFS measurements will be possible. It is also necessary to evaluate to what extent the laminar flow in the microchannels affects the spectra. While from the application point of view, the nanoparticles obtained through the microfluidic process are comparable in monodispersity to those made in batch, future optimization of precursor and surfactant systems, pumping as well as the integration of more effective mixing, should allow for the synthesis of more monodisperse particles.

Appendix A Time dependent SQUID measurements of the DCO and ADH syntheses

Time dependent comparative study of SQUID measurements of two organometallic precursors the DCO and ADH has pointed out different magnetic properties of the resulting nanoparticles, influenced by both time of the reaction as well as nature of the precursor utilized. Figure A 1 shows magnetization versus applied magnetic field data at 10 K and at 300 K for the "DCO 9h", DCO 18h", ADH 9h" and "ADH 18h" samples. The slope of the magnetization curves almost saturate at high fields. Enlarged views of hysteresis curves confirm absence of asymmetrical loop shift thus indicating about not oxidized cobalt core.[90] The main parameters obtained from the magnetic data are given in Table 11. As can be seen from Figure A 1 (a), the "DCO 9h" sample of 7.4±0.09 nm Co nanoparticles show a coercive field (H_c) of 370 Oe and saturation magnetization (M_s) of 49.3 (emu/g). At the end of the synthesis, the "DCO 18h" sample of 3.8±0.2 nm particles show a decrease in coercivity to 275 Oe with increase in saturation magnetization up to 54.1(emu/g) (Figure A 1 (b)). This is anticipated, as the smaller particles will have smaller coercivities and exhibit soft magnetic properties. Also, an increasing of saturation magnetization is in agreement with previous experimental results and theoretical work that predicts an enhancement of the magnetic moment per atom in the two or three surface atomic layers in nanoscale particles.[91] On the other hand, H_c of Co nanoparticles from the ADH increase from 590 Oe for the "ADH 9h" sample to 1525 for the "ADH 18h" sample. In addition, TEM analysis showed the mean particle size remains the same within the error bars, along with the phase transformation to fcc structure, from XAS analysis. Similar, unexpected results were already observed in our group before[92] and by others[93]. These changes confirm that the magnetic behavior of the nanoparticles is the result of many factors such as the particle size, crystal structure[93], nature of surface adsorbate[94] interparticle coupling[95] and intraparticle interactions between the metal core and the surface oxide[96]. Overall comparison of the coercivity for the Co NPs from the ADH and DCO indicate that particles resulting from the ADH precursor show larger coercivities as well as remanence (M_r/M_s) 0.47 for the "ADH 18h" sample and 0.55 for the "ADH 9h" sample compared to 0.22 for the "DCO 18h" sample and 0.26 for the "DCO 9h" sample (Table 11).

Table 11 Magnetic parameters.

Sample	M_s (emu/g)	M_r/M_s	H_c (Oe)	T_b (K)
"DCO 9h"	49.31	0.26	370	67
"DCO 18h"	54.13	0.22	275	100
"ADH 18h"	64.26	0.47	1525	250
"ADH 9h"	180	0.55	590	300

The "DCO 9h" sample has a 67 K blocking temperature and a large increase in the FC magnetization with decreasing temperature (Figure A 2). Such large increase in magnetization at lower temeratures is known to be associated with thin oxide shell.[97] From previous investigation[61] we know that particles resulting from the DCO precursor are less stable against oxidation compared to those from the ADH. This supports XAS results that the "DCO 9h" sample has a light backscatter, such as O or C in the first coordination shell of corresponding Fourier transform. The blocking temperature above 300 K in the ZFC data and flatness of the FC

curve indicate magneto-static interparticle coupling upon cooling for the “ADH 9h” sample. The high blocking temperature of 250 K in the ZFC curve for the “ADH 18h” sample and flatness of the FC curve also indicate interparticle coupling compared to 100 K blocking temperature of the “DCO 18h” sample along with large increase in the FC magnetization with decreasing temperature. This again supports XAS results that Co NP’s from the DCO have a thin oxide shell.

Another interesting observation is the presence of a kink in the hyteresis loop of the “ADH 9h” sample (Figure A 1 (d)). Such a behavior was previously attributed to particles forming chains leading to magneto-static interaction as described by L. Zhang and A. Manthiram,[98] and enhanced energy product with high remanent magnetization and coercivity as described in the work of Zeng H. et al.[99] That approach can be extended to other multi-component systems or, as in our case, to a single component system which possesses different phases and/or phase transformations. In this model, a kink which the hystereses loop shows at low field (Figure A 1 (d)) suggests two -phase behavior, when hard and soft phases are not able to switch cooperatively. On the other hand, the coercivity enhancement in the “ADH 18h” sample might indicate an effective exchange interparticle coupling. Detailed understanding of interparticle coupling requires the study of ordered nanocrystal arrays with precisely controlled size and spacing of particles.

Results of magnetic measurements concurred with XANES and EXAFS analysis (Chapter 6) and with the previous results of our group on the effect of precursor on cobalt nanoparticles formation,[61] also indicating influence of the nature of the precursor and reaction time on the properties of nanoparticles obtained.

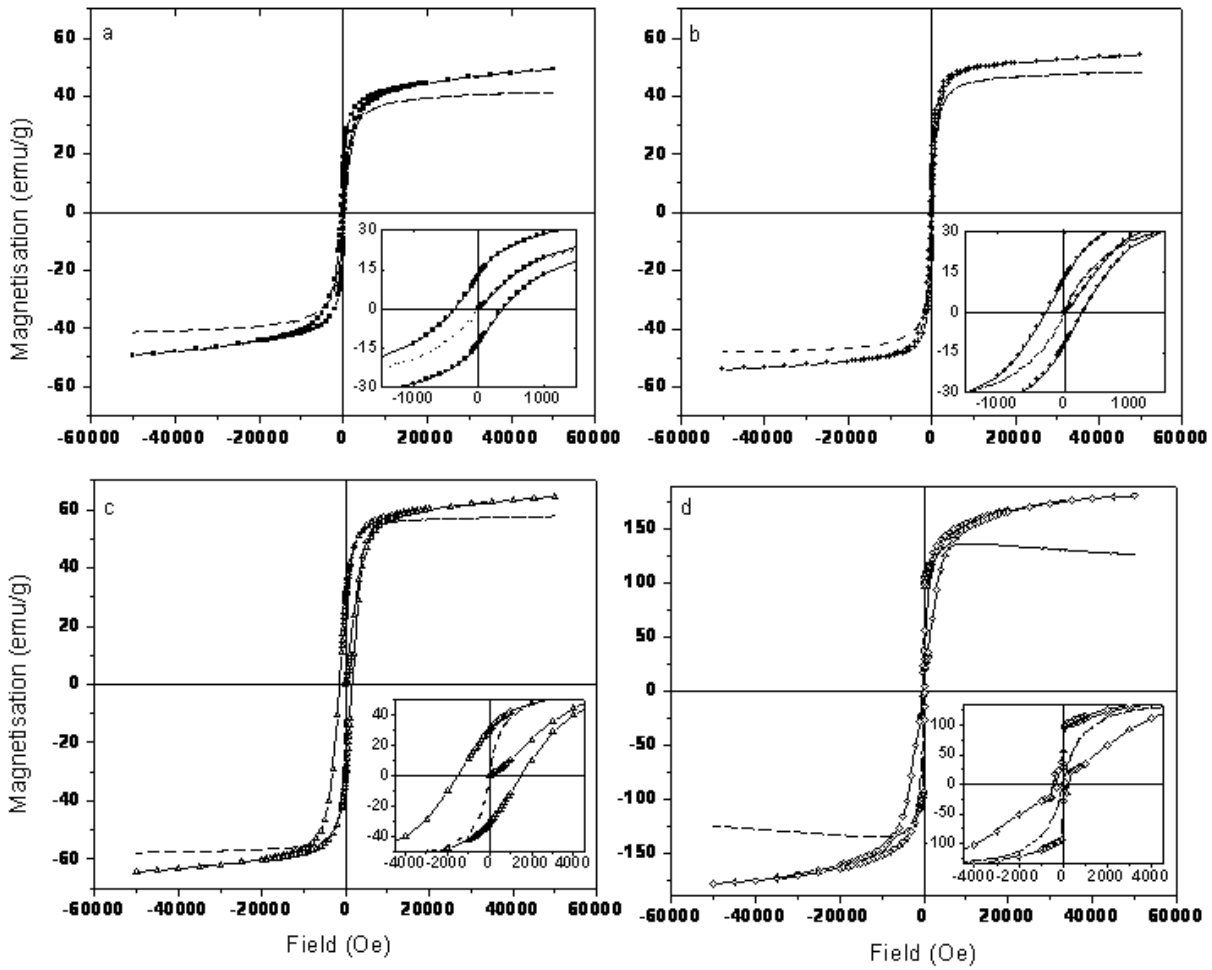

Figure A 1 Magnetization curve versus applied field at 10 K (dashed black) and 300 K (line with symbol black): a) "DCO 9h" b) "DCO 18h" c) "ADH 18h" d) "ADH 9h.

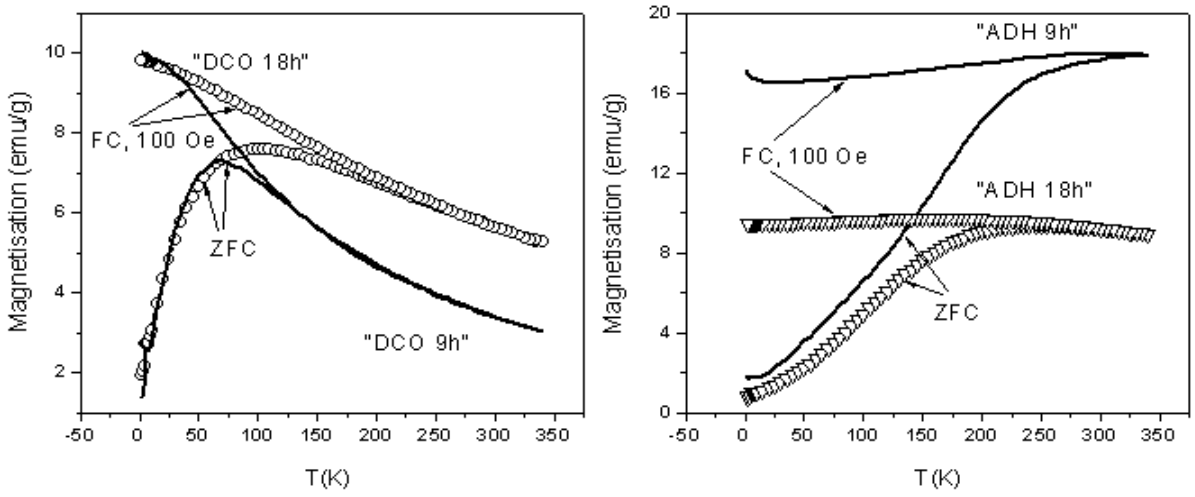

Figure A 2 ZFC/FC magnetization for the "DCO 9h", "DCO 18h", "ADH 9h" and "ADH 18h".

Appendix B Surface functionalization of Co NP's by L-cysteine ethyl ester

Several methods have been developed to modify the surface properties of the magnetic Co nanoparticles, suitable for attachment of functional, bioactive groups, for example, by peptization with functional organic molecules, silanization, and in situ polymerization.[100] The peptized particles exhibit a structure consisting of a metallic core, a protective oxide shell, and an outer layer formed by the surfactant. Naturally, it is of special interest to analyse what effects are induced by this modification to the structure and properties of the particle, as in general surface modification has been shown to have a notable influence on the electronic structure and magnetic properties of such particles.[101]

Co K-edge XANES spectra of modified with L-cysteine ethyl ester Co NP's, a spectrum of Co foil and Co NP's after "standard" synthesis (not modified) are shown in Figure B 1. The pre-edge intensity is reasonably close to that for metallic cobalt. Together with the absence of drastically increased white line intensity and the presence of only one broad resonance at 7773 eV in the spectra of cobalt oxide which were not observed for the Co NP's, this indicates that one is still dealing with metallic particles which are not oxidized, implying some degree of protection of the cobalt core. The small change in white line intensity relative to an hcp Co foil can be attributed to the presence of an fcc rather than an hcp core.

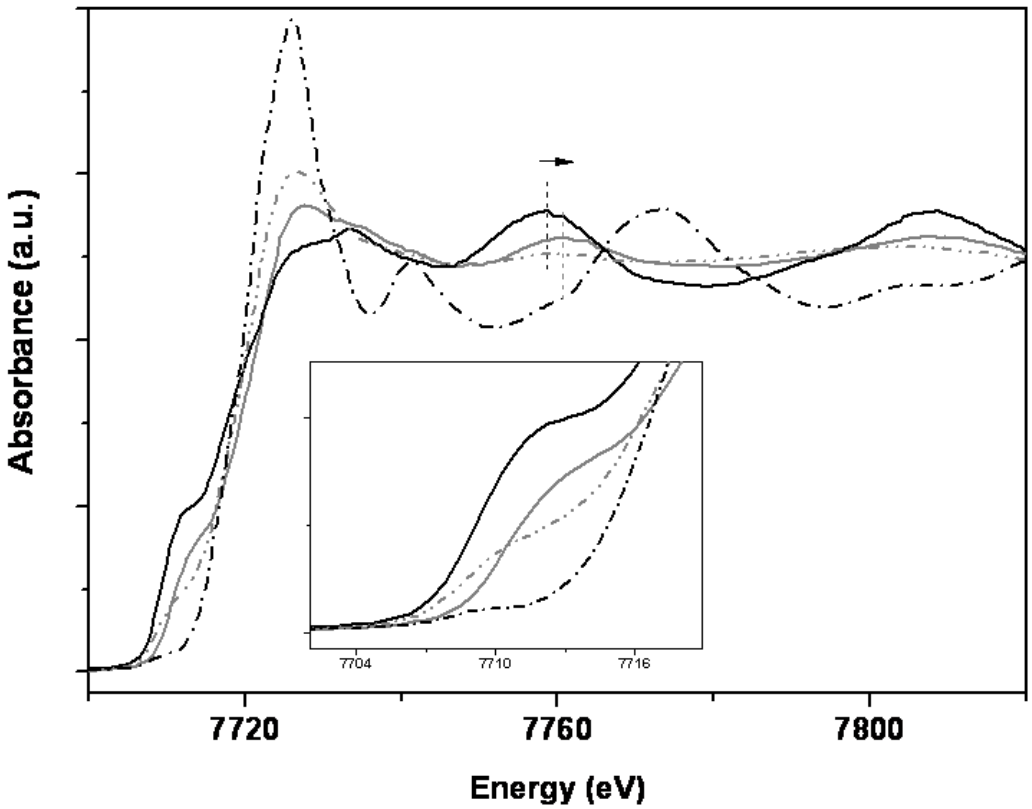

Figure B 1 Co K-edge XANES spectra of Co NP's peptized with L-cysteine ethyl ester in comparison with Co foil, Co NP's from "standard" synthesis and Co oxide reference spectra. Enlarged pre-edge region is shown in the inset.

There is, however, one clear deviation from the spectra of both reference foil and Co NP's obtained using an identical procedure, but without L-cysteine ethyl ester as peptization agent: there is a slight chemical shift of the absorption edge towards higher energy and a slight increase in the energy position of the shape resonance at 7760 eV. Tentatively, bearing in mind the importance of surface coordination on XANES spectra of nanoparticles, this change might be attributed to such an effect. In order to verify this assumption, it is first necessary to obtain information on the orientation of the peptization agent on the nanoparticle surface.

To do so, S K-edge XANES measurements have been performed, whose results are shown in Figure B 2 (a). Comparing the S K-edge XANES spectrum of the nanoparticles and the spectrum of the pure peptization agent, differences are observed: the white line is split and the position of the shape resonances changes completely. To understand these effects, one has to recall that in the XANES spectrum of low-*Z* elements life time broadening is sufficiently small- in the case of S K-edge spectra only 0.59 eV- to identify transitions into individual molecular orbitals quite easily. This is verified readily when looking at the cystine reference spectrum also displayed in Figure B 2 (a) in this spectrum, an S–S σ-bond and an S–C σ-bond are expected, which can be directly correlated to the split of the white line in the cystine spectrum. In fact, the only reason why in the cysteine spectrum only one resonance appears to contribute to the white line is the high similarity of the typical energy positions at which the S–C and the S–H sigma bonds typically occur.[102] More detailed information on the correlation between molecular orbitals/bond characteristics and changes in the white line, partly supported by quantum chemical calculations, can be found in the literature.[103]

Returning to the spectrum of interest, the spectacular shift to lower energy which is observed in the nanoparticle spectra can be assigned to the formation of a sulfur–metal bond, leading to a notable charge transfer towards the sulfur atom. This interpretation is supported by the CoS_2 spectrum and reference spectra with systematic variation of the formal valency of S shown in Figure B 2 (b), whose energy position can be used as an approximate scale on which the formal valency of the absorber atom in a given compound can be determined. In fact, this observation is suited to provide an explanation for the observed changes in the position of the absorption edge in the Co K-edge spectra of the nanoparticles peptized using L-cysteine ethyl ester, as such a charge transfer should lead to a global chemical shift in a metallic particle.

As the position of the second peak near the onset of the S K-edge absorption edge remains quite similar to the one of the precursor material, at first sight it might appear unclear whether the second peak corresponds to an S–C bond contribution like in the cystine spectrum, only with a slight shift towards lower energy caused by Co–S bond formation, or whether there are residues of unreacted surfactant, as the energy position of those peak matches very well with the one of L-cysteine. In the latter scenario, however, the corresponding influence of the shape resonances of potential unreacted peptization agent should be observable in the XANES spectrum of the particles, for which hardly any evidence is found in the spectrum. Therefore, it is likely that the cysteine group remains intact. The fact that the amino acid remains free and intact was also confirmed by infrared spectra.[104]

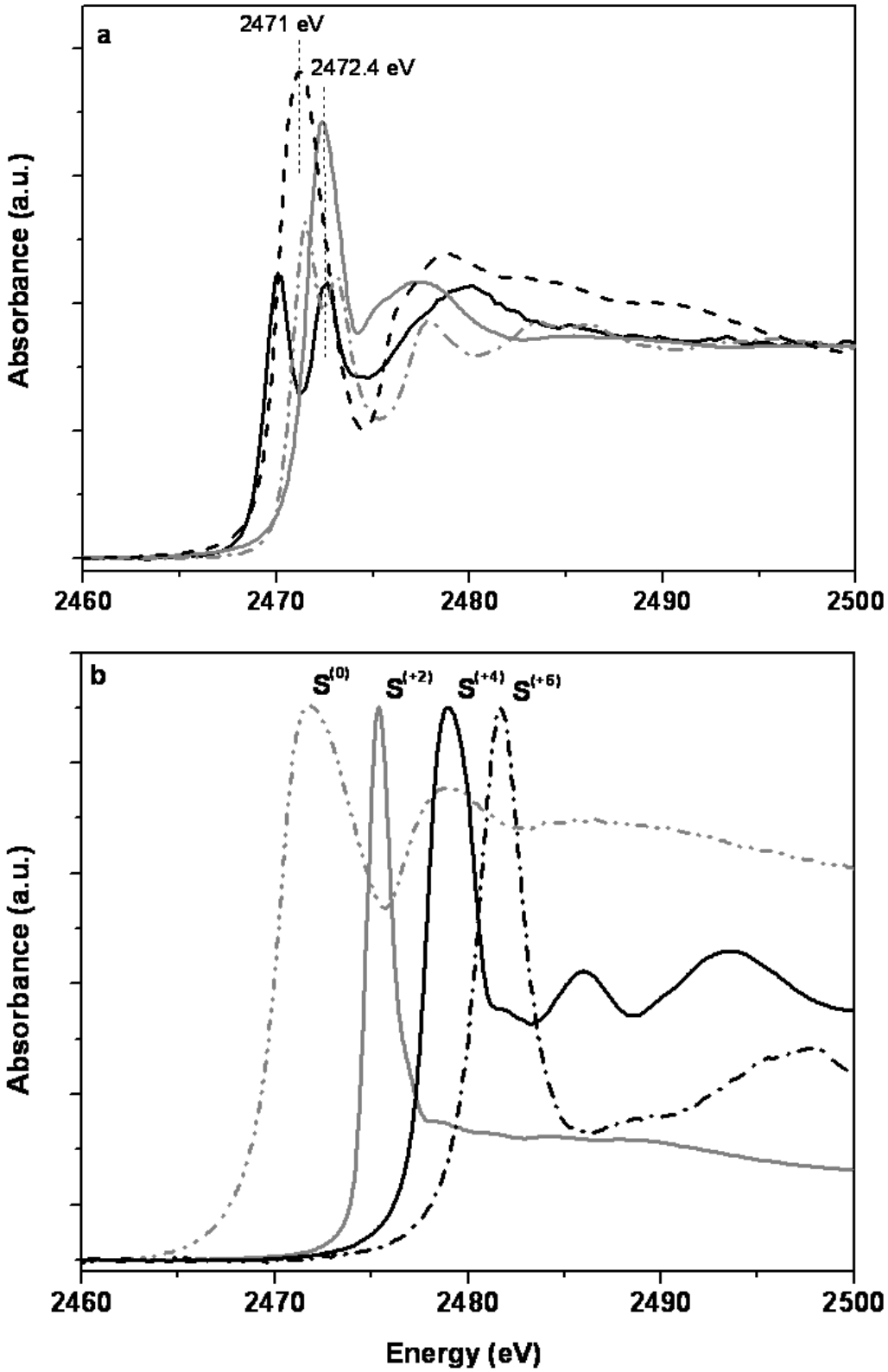

Figure B 2 (a) S K-edge XANES spectra of Co nanoparticles peptized with L-cysteine ethil ester (solid black) in comparison with CoS_2 (dash black), L-cysteine (solid gray) and L-cystine (dash dot gray) references, (b) reference spectra with systematic variation of valence, from left to right: sulfur, $(CH_3)SO$, $(CH_3)SO_2$, $ZnSO_4$.

Using the information obtained at the S K-edge that sulfur is coordinated to metal. Hence in the case of bilayer of Co atoms at the surface, one third of the coordinations should be S atoms. To demonstrate this contribution to the Co K-edge spectra it is possible to construct a structural model of the Co–S interface and check whether such a model (interface contribution) will be suited to explain the changes observed in the Co K-edge XANES spectrum of the peptized nanoparticles. The calculations were performed using real-space full multiple scattering FEFF8 code.

On account of fcc-like features of nanoparticles observed at the Co K-edge and typical hollow positions of sulfur in sulfur–metal compounds,[105,106] the model was built based on a CoS_2[105] structure in which the disulfide bond was omitted. First, Co K-edge fcc XANES spectrum of bilayer of Co atoms up to 10 Å in diameter were calculated as a reference for comparison of Co-S interface contribution and contribution of only Co atoms surface (Figure B 3 (a)). Furthermore, to imitate the Co–S interface effect, the first Co–S coordination shell was formed by translation of sulfur top atoms along the Y axis 1.6 Å above the Co surface so that the typical Co–S distance would be 2.32 Å[105] and inner S atoms remained discarded. All calculations were performed using the spherical self-consistent muffin-tin potential. A core- hole is included on the absorber atom in order to mimic the final state of the photon absorption process. The self-consistent field radius was chosen as 4.189 Å, so that approximately 30 atoms were included in the calculations of potential field. Results are present in Figure B 3 (a). As can be seen theoretical calculations confirm the shift of the absorption edge and the shape resonance to a slightly higher energy discussed above and illustrates its dependence on sulfur occupation of the cobalt surface. The significance of this result is underlined by the fact that the reproduction of this shift using O or C as surface coordination fails, as shown in Figure B 3 (b).

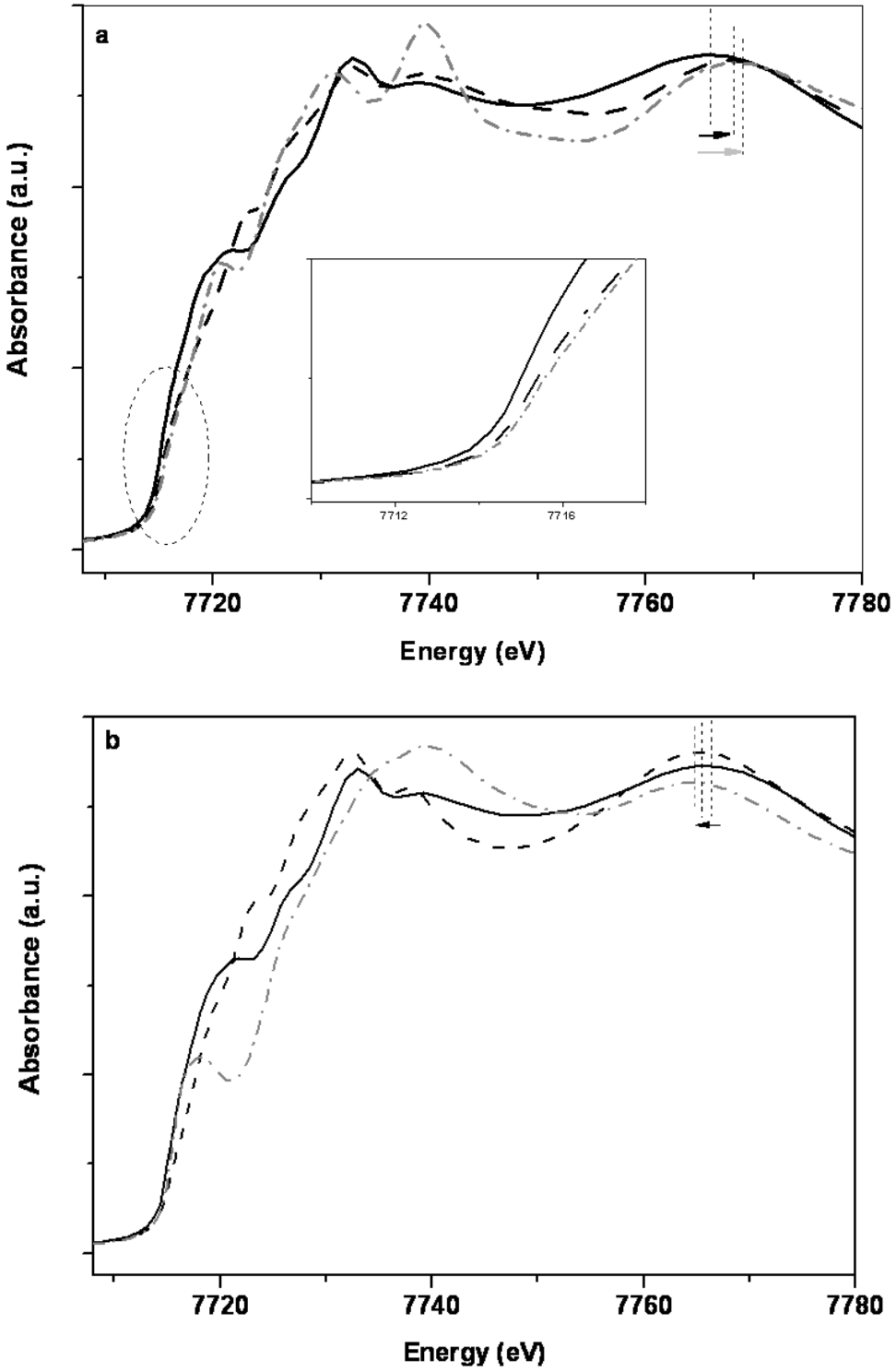

Figure B 3 Co K-edge FEFF8 calculated XANES spectra of bilaier of Co atoms *fcc* structure (solid black) in comparison with a) Co-S interface effect, partially filled (dash dot black), full occupied surface (solid gray), enlarged view of the pre-edge region is in the inset; b) Co-O interface effect (dash black) and Co-C (dash dot gray).

List of Figures

List of Tables

Acknowledgements

First of all, I would like to express my deepest gratitude to Prof. J. Hormes for giving me the opportunity to carry out my doctoral studies in his group. He has been a continuous inspiration and motivation, not only on a scientific, but also on a human level. His openness has created great atmosphere within the group, which helped enormously during the hard times and made the thesis supervision outstanding.

I am also very thankful to Dr. Challa Kumar C.S.S.R., who is leading the nanofabrication group in the Center of Advanced Microstructures and Devices (CAMD), Baton Rouge, Louisiana, USA. Working with him was a true pleasure and a constant inspiration.

My special thanks to Dr. W. Rohini M. de Silva for introducing me to a fascinating world of organometallic chemistry. Her world-wide expertise in the wet-chemical synthesis has made a tremendous impact on the outcome of my research. Also she becomes my dear friend with whom I could always share all my problems and hesitations, either scientific or personal.

The experiments presented in this thesis were carried out at CAMD synchrotron facilities involving the outstanding team of people working there and the infrastructure provided by the facility. I am grateful to all the colleagues with whom I shared my time (working and personal) in Baton Rouge. I have benefitted enormously from their scientific expertise and skills in synchrotron radiation, X-ray Absorption Spectroscopy, chemistry and microfluidic development. Special thanks to Dr. M. Fedurin, Dr. V. Palshin, Dr. A. Ignatov for their expertise, constant help and support during the beamtimes. I must truly express my gratitude to Russell Louis for all the contributions he has made to the "*in situ*" research project. He has been a constant source of knowledge about the electronics and programming. Furthermore, I would like to acknowledge all the microfabrication team at CAMD, especially Dr. J. Göttert and Dr. P. Datta for their contributions to the design and the fabrication of the microreactor system.

I would also like to thank all members of SyLi group for their friendship and support throughout my study. Special acknowledgements to Hubert Blank for help and support with mechanical and electronic equipment at all times.

My big thanks go to Prof. V. V. Kotlyar, his wife M. I. Kotlyar and my dearest friends Dr. M.V. Kotlyar and Dr. N. Palina for their spiritual and moral supporting of my studying, especially at the beginning.

I would like to thank all my friends for their kindness, support, understanding, and for nice moments spent together. Last but not the least; I would like to thank my family for their love and encouragement.

Curriculum Vitae

Personal Information

Name	Svetlana Zinoveva
Date of Birth	01.05.79
Place of Birth	Samara, Russia.

Education

1986-1996	High School Education, School № 2, Tereniga, Russia. Graduated with honour school-leaving certificate and silver medal.
1996-2001	Studying at the Physics department of Samara State University, Russia. Graduated with First honour Diploma and qualification: "Physicist. Lecturer in Physics". Qualification thesis: Modeling of kinetic solid gas. The model of soft spheres.
2001-2003	Post graduate studying at the "Physics of solids" faculty, Samara State University.
Since October 2003	PhD work in the group of Prof. Dr. J. Hormes.

Practical Experience

October 2003-2005	Operating an X-ray Absorption Spectroscopy (XAS) beamline at the Electron Stretcher and Accelerator (ELSA) at the Institute of Physics, Bonn; data acquisition.
October 2005-2007	Research experience in the nanofabrication group of Dr. Kumar C.S.S.R. at the Center for Advanced Microstructures and Devices (CAMD) in Baton Rouge, Louisiana, USA. Wet-chemical synthesis of Co nanoparticles via batch and microfluidic processes. Operating the X-ray Microprobe (XMP) beamline at CAMD. Setting-up "*in situ*" XAS experiments at XMP beamline.

References

[1] a) Vieu C., Carcenac F., Pepin A., Chen Y., Mejias M., Lebib A., Manin-Ferlazzo L., Couraud L., Launois H., *Appl. Surf. Sci.*, 164, 111, **2000**; b) Brehmer M., Conrad L., Funk I., *J. Dispers. Sci. Techol.*, 24, 291, **2003**; c) Lee S.J., Jeong J.R., Shin S.C., Kim J.C., Kim J.D., *J.Magn. Magn. Mater* 282, 147, **2004**.

[2] Morita S., Yib I., Sugimotoa Y., Oyabu N., Nishi R., Custance O., Abe M., *Applied Surface Science* 241, 2, **2005**.

[3] a) Masala O., Seshadri R., *Annu. Rev. Mater. Res*., 34, 41, **2004**; b) Green M., *Chem. Commun.*, 3002, **2005** and references therein; c) Boennemann H., Richards R.M., *European J. Inorg. Chem.* 10, 2455, **2001**; d) Schmid G., (Ed.); "*Clusters and colloids-from theory to applications*", VCH: Wienheim, **1994**; e) Cha S. I., Chan B. M., Kim K. T., Hong S. H., *J. Mater. Res*., 20, 2148, **2005**; f) Murray C. B., Sun S., Gaschler, W., Doyle, H., Betley, T. A., Kagan, C. R., *IBM J. Res. Dev*,45, 47, **2001**; g) Wagner J., Kirner T., Mayer G., Albert J. A. & Köhler J. M., *Chem. Eng. J.* 101, 251, **2004**; h) Yen B. K. H., Günther A., Schmidt M. A., Jensen K. F. & Bawendi M. G., *Angew. Chem. Int. Edn.* 44, 5447, **2005**.

[4] Borchert H., Shevchenko E.V., Robert A., Mekis I., Kornowski A., Gruebel G., WellerH., *Langmuir*, 21 (5), 1931, **2005**.

[5] Koningsberger D. C., *X-ray Absorption Principles, Applications, Techniques of EXAFS, SEXAFS and XANES*, Wiley, New York, **1988**.

[6] Puntes, V. F., Krishnan, K.M., Alivisatos, A.P., *Science* 291, 2115, **2001**.

[7] Bao Y.A., Pakhomov B. and Krishnan K.M., *J. Appl. Phys.* 97, 10J317, **2005**.

[8] Lagunas A., Jimeno C., Fond D., Sola l., Pericás M.A., *langmuir* 22, 3823, **2006**.

[9] De Silva R., Palshin V., Fronczek F.R., Hormes J., Kumar C. S. S. R., *J. Phys. Chem.* C, 111(28), 10320, **2007**.

[10] Rehr J. J. and Albers R. C., *Reviews of Modern Physics* 72, 621, **2000**.

[11] Teo B.K., EXAFS: *Basic Principles and Data Analysis.* Springer-Verlag Berlin Heidelberg New York Tokyo, **1986**.

[12] Rehr J. J., Albers R. C., Natoli C. R., and Stern E. A., *Phys. Rev*. B, 34, 4350, **1986**.

[13] Sayers D. E., Stern E. A., and Lytle F. W., *Phys. Rev. Lett.* 27, 1204, **1971**.

[14] Stern E.A., Theory of EXAFS. Konigsberger D.C. and Prinz R., editors, *X-Ray Absorption: Principles, Applications, Techniques of EXAFS, SEXAFS, and XANES*, volume 92 of *Chemical Analysis*, chapter1, 3-51, John Wiley and Sons, New York, **1988**.

[15] Ravel B.and Newville M., *Journal of Synchrotron Radiation* 12, 537, **2005**.

[16] Ankudinov A.L., Ravel B., Rehr J.J., and Conradson S.D., Phys. Rev. B 58, 7565, **1998**.

[17] Newville M., Livins P., Yacoby Y., Stern E. A., and Rehr J. J., *Phys. Rev*. B, 47,14126—14131, **1993**.

[18] Kelly S. "Basics of EXAFS Analysis", NSLS EXAFS workshop, available online, **2003**.

[19] Bevington P.R. and Robinson D.K. *Data Reduction and Error Analysis for the Physical Science*. Mcgraw-Hill, new York, 2nd edition, **1992**.

[20] Basinski Z.S., Hume-Rothery W., Sutton A.L., Proceedings of the Royal Society of London, Series A: *Mathematical and Physical Sciences* 229, 459, **1955**.

[21] Rehr J. J. and Albers R. C., *Reviews of Modern Physics*, 72, 621, **2000**.

[22] http://www.synchrotron soleil.fr.

[23] Krinsky S., Fundamentals of Hard X-Ray Synchrotron Radiation Sources, in *Third-Generation Hard X-ray Synchrotron Radiation Sources*, edited by Mills D. M., 1-40, John Wiley and Sons, Inc., New York, **2002**.
[24] http://camd.lsu.edu/ Annual Report **2005**.
[25] C. J. Sparks, "Synchrotron Radiation Research," in *Synchrotron Radiation Research,*459, edited by H. Winick, S. Doniach, Plenum Press, New York, **1980**.
[26] Lemonnier M., Collet O., Depautex C., Esteva J. M., Raoux R., *Nucl. Instr. Meth.* A, 152, 109, **1978**.
[27] Pinsker Z.G. *Dynamical Scattering of X-Rays in Crystals,* Springer-Verlag Berlin Heidelberg New York, **1978**.
[28] Materlik, G.; Kostroun, V. O., *Review of Scientific Instruments* 51, 86-94, **1980**.
[29] http://henke.lbl.gov/optical_constants/
[30] Mölders N., Moser H.O., Saile V., Schilling P.J., *Spatially-Resolved X-Ray Spectroscopy at CAMD,* Wissenschaftliche Berichte FZKA 6314, **1999**.
[31] Kirkpatrick P., Baez A.V., *J.Opt.Soc.Am*., 38, 766, **1948**.
[32] Lee P. A., Citrin P. H, Eisenberg P. and Kincaid B. M., *Rev. Mod.Phys*. 53, 769, **1981**.
[33] Stern E. A. and Kim K., *Phys. Rev. B* 23, 3781, **1981**.
[34] Rothe J., *"Zwischen Molekuel und Festcorper: Roengenabsorptionsspectroskopie an Uebergangsmetallkolloiden"* ISBN 0172-8741 Doctoral Thesis, Bonn University, **1997**.
[35] a) Bönnemann H., Brijoux W., Brinkmann R., Matoussevitch N., Waldöfner N., Palina N., and Modrow H., *Inorg. Chim. Acta* 350, 617, **2003**; b) Bönnemann H., Brijoux W., Brinkmann R., Matoussevitch N., Waldöfner N., DE 10 227 779.6 to Studiengesellschaft Kohle mbH, **2002**; c) Bönnemann H., Brand R. A., Brijoux W., Hofstadt H. W., Frerichs M., Kempter V., Maus-Friedrichs W., Matoussevitch N., Nagabhushana K. S., Voigts F., and Caps V., *Appl. Organomet. Chem*. 19, 790**, 2005**.
[36] Sternburg, H. W.; Greenfield, H.; Wotiz, J. H.; Friedel, R. A.; Markby, R.; Wender, I. *J. Am. Chem.Soc*., 76, 1457, **1954**.
[37] Son S.U., Lee S.I., Chung Y.K., Kim S.-W., Hyeon T., *Organic letters,*Vol.4, No.2, 278, **2002.**
[38] *http://www.kern-microtechnic.com/2-Machines-Micro.html*
[39] *http://www.jo-mikrotechnik.com/*
[40] a) Juang, Y.J., L.J. Lee, and K.W. Koelling, *Hot embossing in microfabrication. Part I: Experimental.* Polymer Engineering and Science, 42(3): p. 539-550, **2002;** b) Juang, Y.J., L.J. Lee, and K.W. Koelling, *Hot embossing in microfabrication. Part II: Rheological characterization and process analysis.* Polymer Engineering and
Science, 42(3): p. 551-566, **2002.**
[41] Datta P. *Modular, Polymeric Development Platform for Microfluidic ApplicationsDesign, Fabrication, Testing and Examples* **2007** Doictoral Thesis, Fakultät für Maschinenbau der Universität Karlsruhe.
[42]a) Turkevich J., Stevenson P.C., Hillier J., *Faraday Disscus.Chem. Soc.* 11, 55, **1951**; b) Privman V., Goia D.V., Park J., Matijevic E. *J. Colloid and Interface Sci.*, 213, 36, **1999**; c) Oxtoby D.W., *Acc. Chem. Res*. 31, 91, **1998**.
[43] a) La Mer V.K. and Dinegar R.H., *J. Am. Chem. Soc., 72*(11), 4847, **1950**; b) La Mer V., *Ind. Eng. Chem.*, 44, 1270, **1952**.
[44] Watzky M.A. and Finke R.G., *J. Am. Chem. Soc., 119,* 10382, **1997**.

[45] a) Becker R., Döring W., *Ann. Phys*. 24, 719, **1935**; b) Volmer M., *Kinetik der Phasenbildung*, Steinfopff, Leipzig, **1939**.
[46] Widegren J.A., Aiken J. D. III, Őzkar S., and Finke R.G., *Chem. Mater.*, 13, 2, 312, **2001**.
[47] Watzky M.A. and Finke R.G., *Chem. Mater*., 9, 3083, **1997**.
[48] Turkevich J., Stevenson P. C., Hillier J., *Faraday Disc. Chem. Soc*. 11, 55, **1951**.
[49] Finney E.E., Finke R.G. *J.Coll. Interface Sci.*, Accepted manuscript, **2007**.
[50] Rothe J., Hormes J., Boennemann H., Brijoux W., Siepen K. *J. Am. Chem. Soc.*, 120, 6019-6023, **1998**.
[51] a) Angermund K., Bühl M., Dinjus E., Endruschat U., Gassner F., Haubold H.G., Hormes J., Köhl G., Mauschick F.T., Modrow H., Mörtel R., Mynott R., Tesche B., Vad T., Waldöfner N., Bönnemann H., *Angew. Chem. Int. Ed.* 41, 4041, **2002**; b) Angermund K., Bühl M., Endruschat U., Mauschick F.T., Mörtel R., Mynott R., Tesche B., Waldöfner N., Bönnemann H., Köhl G., Modrow H., Hormes J., Dinjus E., Gassner F., Haubold H.G., Vad T., Kaupp M. *J. Phys. Chem*. B 107, 7507, **2003**.
[52] Ciacchi L. C., Mertig M., Pompe W., Meriani S., De Vita A., *Platinum Metals Rev*. 47, 98, **2003**.
[53] Henglein A., Giersig M., *J. Phys. Chem. B, 104,* 6767, **2000**.
[54] Henglein A., Giersig M., *J. Phys. Chem. B, 103,* 9533, **1999**.
[55] Pong B.K., Elim H.I., Chong J.X, Ji W., Trout B.L., and Lee J.Y. *J. Phys. Chem. C, 111,* 6281, **2007**.
[56] Wang J., Boelens H. F. M., Thathagar M. B., Rothenberg G., *Phys. Chem. Chem. Phys.* 5, 93, **2004**.
[57] a) Wang J., Boelens H. F. M., Thathagar M. B. and Rothenberg G., *Chem. Phys. Chem*, 5, 93, **2004**; b) Cruz S. C., Aarnoutse P. J., Rothenberg G., Westerhuis J. A., Smilde A. K. and Bliek A., *Phys. Chem. Chem. Phys.*, 5, 4455, **2003**.
[58] Gaikwad A. V. and Rothenberg G., *Phys. Chem. Chem. Phys*., 8, 3669, **2006**.
[59] King S., Hyunh K., Tannenbaum R., *J. Phys. Chem*. B 107, 12097, **2003**.
[60] a) Ungvary F., Marko L. *J. Organomet. Chem.*,71,283, **1974**; b) Papirer E., Horny P., Balard H., Anthore R., Petipas C., Martinet A. *J. Colloid Interface Sci. 94*, 207, **1983**; c) Papirer E., Horny P., Balard H., Anthore R., Petipas C., Martinet A. *J. Colloid Interface Sci*. *94*, 220, 1983; d) Tannenbaum, R., Bor G. *J. Organomet. Chem.*, 586,18, **1999**.
[61] de Silva R., Palshin V., Fronczek F.R., Hormes J., KumarC. S. S. R., *J. Phys. Chem.* C, 111(28), 10320, **2007**.
[62] Ericsson T., *Acta Metall*. 14, 853, **1966**.
[63] Kitakami O., Satao H., Shimada Y., Sato F., Tanaka M., *Phys. Rev*. B, 56, 13849, **1997**.
[64] Ostwald W., *Z Phys.Chem.* 22, 289, **1897**.
[65] Plummer E.W., Salaneck W.R.,Miller J.S., *Phys. Rev.* B, 18, 4, 1673, **1978**.
[66] Kazusaka A. and Howe R.F., *J. Mol. Catal*. 9, 183, **1980**.
[67] Palina N., *Novel magnetic nanoparticles: size and surfactant effects on geometric and electronic structure, probed using X-ray Absorption Spectroscopy*, ISBN 0172-8741 Doctoral Thesis, Bonn University, **2005**.
[68] Fecht J.H., *Acta Metall. Mater*., 38, 1927, **1990**.
[69] De Lima, J.C., dos Santos, V. H. F., Grandi T. A. and de Biasi R.S. *Cond. Mat.* 26, 10415D, **2000**.

[70] Christian J. W. *The Theory of Transformations in metals and Alloys,* vol I (Oxford: Pergamon), **1975**.
[71] a) Frahm R. *Rev. Sci. Instrum.,60,* 2515, **1989**; b) Frahm R., *Nucl .Instrum. Methods* A, 270, 578, **1988**; c) Cimini F. and Prins R., *J. Phys. Chem.* B, 101, 5277, **1997**.
[72] Edwards A.B., Garner C. D. and Roberts K. J., *J. Phys. Chem. B,* 101, 20, **1997**.
[73] Hagelstein M., Cunis S., Frahm R. , Niemann W. and Rabe P., *Physica* B, 158, 324, **1989**.
[74] De Mello A. J., *Nature*, 442, 394, **2006**.
[75] Zimmerman, W. B. J. (Ed.) Microfluidics: History, Theory and Applications, **2006.**
[76] Greenway G. M., Haswell S. J., Morgan D. O., Skelton V. and Styring P. *Sens. Actuators B* 63,153, **2000**.
[77] Beebe D.J., Mensing G.A. and Walker G.M. *Annu. Rev. Biomed. Eng*. 4, 261, **2002**.
[78] a) Wootton R. C. R., Fortt R. and De Mello A. J. *Lab Chip* 2, 5, **2002**; b) Chambers R. D., Fox, M. A. and Sandford G. *Lab Chip* 5, 1132, **2005.**
[79] Song Y., Doomes E.E., Prindle J., Tittsworth R., Hormes J. and Kumar C. S.S. R., *J. Phys. Chem. B* 109**,** 9330, **2005**.
[80] Song Y., Kumar C. S. S. R. and Hormes J., *J. Nanosci. Nanotech.* 4, 788, **2004**.
[81] Lin X. Z., Terepka A. D. and Yang H., *Nano Lett.* 4, 2227, **2004**.
[82] Wagner J., Kirner T., Mayer G., Albert J. A. and Köhler J. M., *Chem. Eng. J.* 101, 251, **2004**.
[83] http://www.upchurch.com/
[84] http://www.bostik-us.com
[85] http://www.bio-chemvalve.com/Self-Priming_Micro_Pumps.pdf
[86] Arp U., Lagutin B.M., Materlik G., Petrov I.D., Sonntag B. And Sukhorukov V.L., *J.Phys.* B: At. Mol. Opt. Phys. 26, 4381, **1993**.
[87] a) Wang J., Chong P.F., Ng S.C., Gan L.M., *Mater. Lett.*, 30, 217, **1997**; b) Glavee G.N., Klabunde K.J., Sorensen C.M., Hadjipanayis G.C., *Langmuir,* 10, 4726, **1994**; c) Glavee G.N., Klabunde K.J., Sorensen C.M., Hadjipanayis G.C., *Langmuir,* 9, 162, **1993**; d) Glavee G.N., Klabunde K.J., Sorensen C.M., Hadjipanayis G.C., *Inorg.Chem.*, 32, 474, **1993**.
[88] Zhurakovskii E.A., Shashkina T.B. and Kotlyar V.I. *Russian Phys. J.*, Vol.13,1, **1970**.
[89] Watzky M. A., Finke R. G., *J. Am. Chem. Soc*. 118, 10382, **1997**.
[90] a) Berkowitz A. E., Takano K. **1999** *J. Magn. Magn. Mater., 200,* 552-570 b) Kiwi M. **2001** *J. Magn. Magn. Mater., 234,* 584-595.
[91] a) Li Z., Gu B., *Phys. Re*V. *B* **1993**, *47*, 13611 b) Wu R., Freeman A., J. *Phys. Re*V. *B,* 47,, 3904, **1993**; c) Eriksson O., Boring A. M., Albers R. C., Fernando G. W., Cooper B. R., *Phys. Re*V. *B 45*, 2868, **1992**.
[92] Song Y., Modrow H., Henry L.L., Saw S.K., Doomes Ed. E., Palshin V., Hormes J. and Kumar C.S.S.R., *Chem. Mater.,* 18 (12), 2817, **2006**.
[93]Sun S., Murray C.B., *J. Appl. Phys.* 85, 4325, **1999**.
[94] a) Luna C., Morales M.P., Serna C.J. and Vázquez, *Mater. Sci. Engin.*, C 23, 1129, **2003**; b) Margeat O., Amiens C., Chaudret B., Lecante P., Benfield R.E. *Chem. Mater.*, 17 (1), 107, **2005**.
[95] Zeng H., Li J., Liu J. P., Wang Z. L., Sun, S. **2002** *Nature, 420,* 395-398.
[96] Zalich M.A., Baranauskas V.V., S. Riffle J.S., Saunders M., and Pierre T.G. St., *Chem. Mater., 18*, 2648, **2006**.
[97] a) Bao Y., Beerman M., Pakhomov A.B., Krishnan K.M., *J.Phys.Chem B.*, 109, 7220, **2005**; b) Komada R. H., Berkowitz A. E., Mcniff E., J., Foner Jr. and S., *J. Appl. Phys, 81*, 5552, **1997**; c)

Tung L. D., Kolesnichenko V., Caruntu D., Chou N. H., O'Connor C. J., Spinu L., *J. Appl. Phys. 93*, 7486, **2003**.

[98] Zhang L.and Manthiram A., *Phys. Rev.* B, 54 (5), 3462, **1996**.

[99] Zeng H., Li J., Liu J. P., Wang Z. L., Sun, S., *Nature*, *420*, 395,**2002**.

[100] a) Ramirez L. P. and Landfester K., *Macromol. Chem. Phys.* 204, 22, **2003**; b) Yang C, Liu H, Guan Y, Xing J, Liu J and Shan G *J. Magn. Magn. Mater.* 293, 187, **2005**; c) Behrens S. Boennemann H., Matoussevitch N., Gorschinski A., Dinjus E., Habicht W., Bolle J., Zinoveva S., Palina N., Hormes J., Modrow H., Bahr S., Kemter V., *J. Phys.: Condens. Matter*, 18, 1, **2006**.

[101] a) Margeat O., Amiens C., Chaudret B., Lecante P. and Benfield R. E., *Chem. Mater.* 17, 107, **2005**; b) Zhang P. and Sham T. K., *Phys. Rev. Lett.* 90, 245502, **2003**; c) Vestal C. R. and Zhang Z. J., *J. Am. Chem. Soc.* 125**,** 9828, **2003**; d) Modrow H., *Appl. Spectrosc. Rev.* 39, 183, **2004**; e) Skumryev V., Stoyanov S., Zhang Y., Hadjipanayis G., Givord D. and Nogues J., *Nature* 19, 850, **2003**.

[102] Prange A., Dahl C., Trueper H. G., Behnke M., Hahn J., Modrow H. and Hormes J. *Eur. Phys. J.* D 20, 589, **2002**.

[103] a) Chauvistre R., Hormes J., Hartmann E., Etzenbach N., Hosch R. and Hahn J. *J. Chem. Phys.* 223, 293, **1997**; b) Flemming B., Modrow H., Hallmeier K. H., Hormes J., Reinhold J. and Szargan R. *Chem. Phys.* 270, 405, **2001**; c) von Busch F., Hormes J., Modrow H. and Nestmann N. B. Interaction of atomic core electrons with the molecular valence shell *Interactions in Molecules—Electronic and Steric Effects* ed. S. D. Peyerimhoff (New York: Wiley–VCH) 193 (ISBN: 3-527-27732-3), **2003**.

[104] Behrens S., Bönnemann H., Matoussevitch N., Dinjus E., Modrow H. , Palina N., Frerichs M., Kempter V., Maus-Friedrichs W., Heinemann A., Kammel M., Wiedenmann A., Pop L., Odenbach S., Uhlmann E., Bayat N., Hesselbach J., Guldbakke J.M., *Z. Phys. Chem.*, 220, 3, **2006.**

[105] Nowack E., Schwarzenbach D. and Hahn T., *Acta Crystallogr.* B 47, 650,**1991**.

[106] Will G,. Lauterjung J., Schmitz H. and Hinze E., *Mater. Res. Soc. Symp. Proc.* 22**,** 49, **1984**.